7-26-2012

On Nature of the Gradient Echo MR Signal and Its Application to Monitoring Multiple Sclerosis

Jie Luo
Washington University in St. Louis

WASHINGTON UNIVERSITY IN ST. LOUIS

Department of Chemistry

Dissertation Examination Committee

Joseph Ackerman, Chair

Dmitriy Yablonskiy, Co-chair

Anne Cross

Dewey Holten

Richard Mabbs

Joshua Maurer

On Nature of the Gradient Echo MR Signal and Its Application to Monitoring Multiple Sclerosis

by

Jie Luo

A dissertation presented to the
Graduate School of Arts and Sciences
of Washington University in
partial fulfillment of the
requirements for the degree
of Doctor of Philosophy

August 2012

Saint Louis, Missouri

Abstract

Multiple Sclerosis is a common disease, affecting 2.5 million people world-wide. The clinical course is heterogeneous, ranging from benign disease in which patients live an almost normal life to severe and devastating disease that may shorten life. Despite much research, a fully effective treatment for MS is still unavailable and diagnostic techniques for monitoring MS disease evolution are much needed.

As a non-invasive tool, Magnetic resonance imaging (MRI) plays a key role in MS diagnosis. Numerous MRI techniques have been proposed over the years. Among most widely used are conventional T1-weighted (T1W), T2-weighted (T2W) and FLuid Attenuated Inversion Recovery (FLAIR) imaging techniques. However their results do not correlate well with neurological findings. Several advanced MRI techniques are also used as research tools to study MS. Among them are magnetization transfer contrast imaging (MT), MR spectroscopy (MRS), and Diffusion Tensor Imaging (DTI) but they have not penetrated to clinical arena yet.

Gradient Echo Plural Contrast Imaging (GEPCI) developed in our laboratory is a post processing technique based on multi-echo gradient echo sequence. It offers basic contrasts such as T1W images and T2* maps obtained from magnitude of GEPCI signal, and frequency maps obtained from GEPCI signal phase.

Phase information of Gradient Echo MR signal has recently attracted much attention of the MR community since it manifests superior gray matter/ white matter contrast and sub-cortical contrast, especially at high field (7 T) MRI. However the nature of this contrast is under intense debates. Our group proposed a theoretical framework - Generalized Lorentzian Approach - which emphasizes that, contrary to a common-sense intuition, phase contrast in brain tissue is not directly proportional to the tissue bulk magnetic susceptibility but is rather determined by the geometrical arrangement of brain tissue components (lipids, proteins, iron, etc.) at the cellular and sub-cellular levels - brain tissue “magnetic architecture”. In this thesis we have provide first direct prove of this hypothesis by measurement of phase contrast in isolated optic nerve. We have also provided first quantitative measurements of the contribution to phase contrast from the water-macromolecule exchange effect. Based on our measurement in protein solutions, we demonstrated that the magnitude of exchange effect is 1/2 of susceptibility effect and to the opposite sign.

GEPCI technique also offers a scoring method for monitoring Multiple Sclerosis based on the quantitative T2* maps generated from magnitude information of gradient echo signal. Herein we demonstrated a strong agreement between GEPCI quantitative scores and traditional lesion load assessment. We also established a

correlation between GEPCI scores and clinical tests for MS patients. We showed that this correlation is stronger than that found between traditional lesion load and clinical tests. Such studies will be carried out for longer period and on MS subjects with broader range of disease severity in the future.

We have also demonstrated that the magnitude and phase information available from GEPCI experiment can be combined in multiple ways to generate novel contrasts that can help with visualization of neurological brain abnormalities beyond Multiple Sclerosis.

In summary, in this study, we 1) propose novel contrasts for GEPCI from its basic images; 2) investigate the biophysical mechanisms behind phase contrast; 3) evaluate the benefits of quantitative T2* map offered by GEPCI in monitoring disease of Multiple Sclerosis by comparing GEPCI results to clinical standard techniques; 4) apply our theoretical framework - Generalized Lorentzian Approach – to better understand phase contrast in MS lesions.

Acknowledgements

First and foremost I give my sincere gratitude to my advisor Prof. Dmitriy Yablonskiy. This thesis is produced under his enormous encouragement and support. I really appreciate his help, time, ideas, and funding which make my PhD experience productive and stimulating. I'm also very much grateful to my advisor Prof. Joseph Ackerman for introducing me to BMRL and allowing me to work freely. They are both resourceful teachers, and have taught me in various aspects – MR physics, imaging techniques, writing, academic life, and more. I feel fortunate to have met him at my first step into the world of MRI.

Special thanks to Prof. Anne Cross, for leading me to the field of Multiple Sclerosis. It was a great pleasure to work with her, and she is a role model for me in many ways. Her expertise in MS was essential for the success of our study.

I also would like to thank members from my thesis committee, for their helpful and insightful suggestions/comments.

Thank you to Dr. Pascal Sati, I learned a lot from whom when I first stepped in this lab. And for the initial work he has done for one of the projects. Thank you to Dr. Xiang He, who has been a great collaborator and teacher during my first two years. Thank you to Dr. Andre D'Avignon, who have provided generous support with spectroscopy experiment. Thank you to Dr. Bharathi Jagandeesan, who brought new insights to improve our technique. Thank you to Dr. Robert Schmidt who has generously supported us with his tissue bank and taught us with

his expertise in pathology. Thank you to Dr. Charles Hildebolt, who offered his expertise in statistics. Thank you to Ms. Samantha Lancia and Ms.Susan Fox, who constantly supported us on the clinical side. Thank you to Dr. Alexander Sukstanskii, who supported with mathematical ideas. Thank you to Aditi Iyer, Britney Johnson, and Bryan Nyguen for helping me with experiments.

Dozens of people have helped and taught me immensely at BMRL. I give my heartfelt thanks to Dr. Bill Spees, Mr. John Engelbach, Dr. James Quirk, Dr. Adil Bashir, Dr. Jeffery Neil, Dr. Joel Garbow, Dr. Larry Bretthorst, Dr. Victor Song who provided generous help and advice, both experimentally and theoretically, during my years in BMRL. Also thanks to Ms Debra Brouk for help on purchasing and taking care of financial problems. I'm appreciative my fellow students and researchers in the lab: Dr. Junqian Xu, Dr. Qing Wang, Dr. William Tu, Dr. Jeff Anderson, Dr. Emir Osmagenic, Chiawen Chiang, Qingqing Ye, Xiaojie Wang, Xiaoyu Jiang, Donghan Yang, Xiaoqi Wang, Tsen Hsuan Lin, Chenchen Liu, Yue Zhao, Dr.Joonghe Kim, Dr. Yong Wang, Dr. Peng Sun, Dr. Xialing Ulrich.

Special thanks to my parents, for they have always allowed and supported me to pursue what I want, and to be who I am, which is not typical in Chinese families. Finally, I would like to extend my gratitude to my dear friend Zongxi Li and my husband Shiyi Zhang. They have always been my sources of encouragement both in science and in life. They are part of my motivation to go on. To them I dedicate this thesis.

Table of Contents

List of Figures

List of Tables

Chapter 1 Introduction

1.1 Nuclear Magnetic Resonance Imaging

Magnetic Resonance Imaging (MRI), or nuclear magnetic resonance imaging, is a medical imaging technique used extensively to visualize detailed internal structures of the body. MRI makes uses of the property of nuclear magnetic resonance (NMR) to image (most commonly ^{1}H in H_2O) nuclei inside the body. The content in this section (1.1) can be found in most classical textbooks on the subject (1,2).

1.1.1 Nuclear Spin

Spin is the intrinsic quantum property of nucleons. The overall spin of the nucleus is determined by the spin quantum number S. The spin of a proton, which is the most common signal source in MRI experiment, is 1/2. That means proton has two possible spin states m = 1/2 or m = -1/2 (also referred to as spin-up or spin-down). When placed in a magnetic field, there are only two energy eigenstates, one representing alignment parallel to the field, another anti-parallel. The population ratio of the two states is determined by several factors as shown below:

$$\frac{Population(anti-parallel)}{Population(parallel)} \propto \exp(\frac{-\mu B}{kT}) \qquad [1.1]$$

where μ is magnetic moment of the spin, *B* is external magnetic field strength, *k* is the Boltzmann constant and *T* is the absolute temperature. Majority of spin

population goes to the lower energy state. Note that with *in vivo* biological samples that we are interested in (physiologic temperature) and with commonly available magnets, there is only a slight population difference between two energy states – on the order of 1 in a million spins. Fortunately, in biological samples we have huge population of ^{1}H (55 Molar), which provides a sufficient signal.

In the field of magnetic resonance, for convenience in describing mechanism of signal generation (which is coming not from single spin but from object comprised of millions of spins), spins are usually analogued in the context of classical physics. Just as a spinning top precesses around the gravitational field, nuclear spin precesses around the magnetic field. The frequency of this precession is called Larmor frequency $\omega_0 = \gamma \cdot B_0$, which is proportional to the strength of magnetic field B_0, and γ - the gyromagnetic ratio.

1.1.2 Free Induction Decay

After nuclear spins are polarized under external magnetic field, they reach equilibrium, and result in a net magnetization along the B_0 field. Upon excitation with a 90° pulse (radiofrequency (RF) pulse), which is perpendicular to the magnetic field, the spins are forced to precess in the transverse x,y plane. A receiver coil is positioned in the transverse plane to pick up the current generated

by the precessing magnetization, which is subsequently amplified and becomes NMR signal.

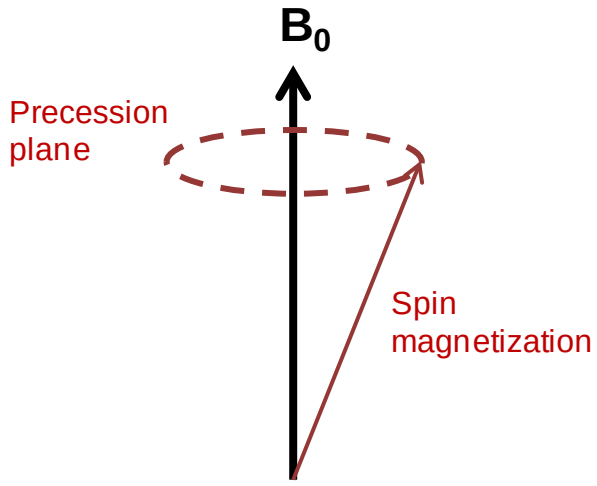

Figure 1.1 Illustration of spin precession.

The NMR signal, known as free induction decay or FID, decays over time (usually on the order of 10^{-1} - 10^{-2} s in human tissue). Because microscopic sources of magnetic fields including electron magnetic moment and electron orbital currents, and also the nucleus itself, create their own local surrounding field, and also because of atomic motions, any nucleus in a sample will experience a net magnetic field whose direction and strength is fluctuating with time. As a result, all individual nuclei precess at slightly different frequencies. They get out of phase with each other over time, causing decay of the macroscopic magnetization.

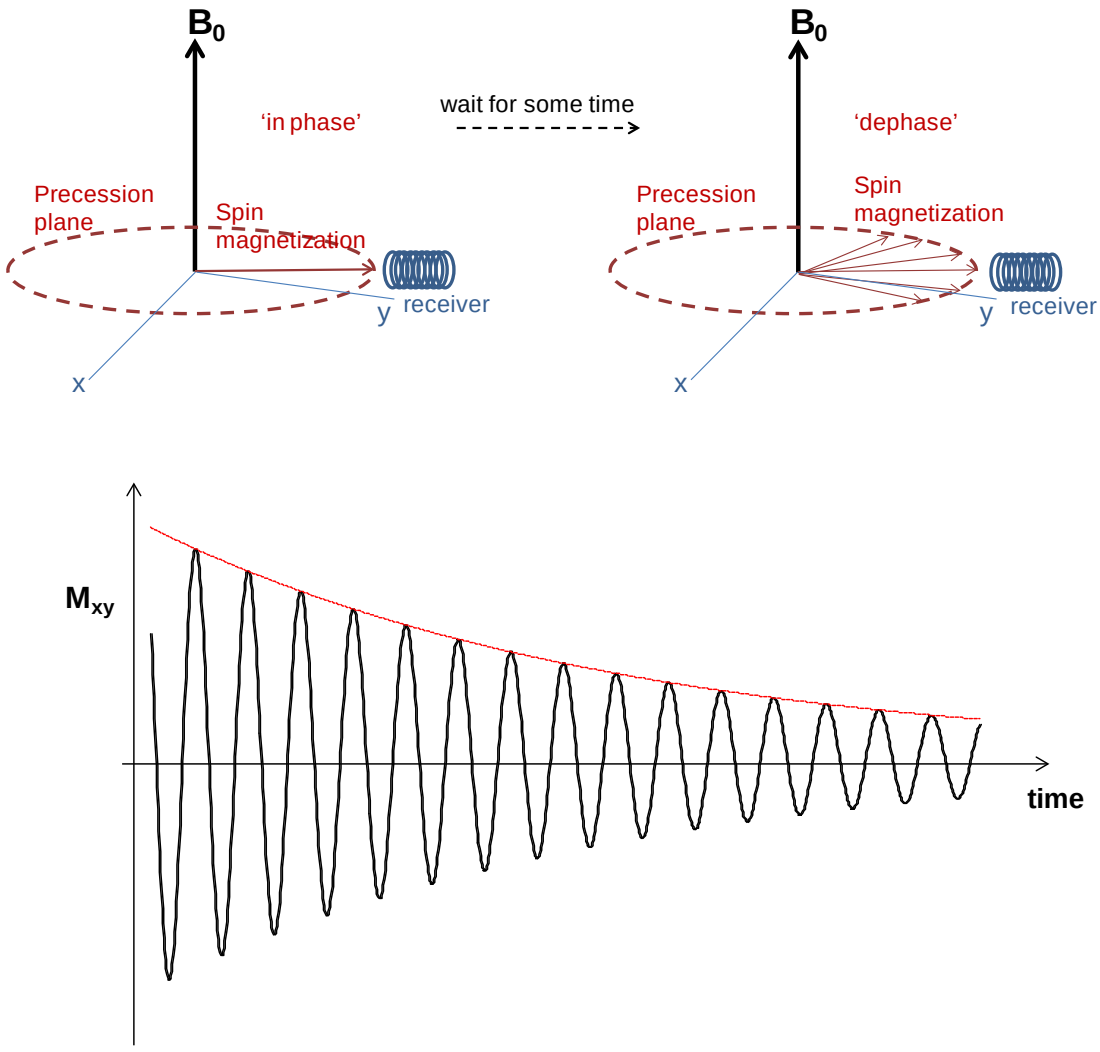

Figure 1.2 Illustration of Free Induction Decay.

1.1.3 Imaging Basics – Gradient and K-space

Applied magnetic field gradients are essential in Magnetic Resonance Imaging experiments. A constant field gradient results in magnetic field with a linear

dependence on position. For example, a gradient in the x-direction, G_x, when applied in addition to a uniform field B_0, gives a spatially dependent field $B = B_0 + x \cdot G_x$; and this field results in a spatially dependent Larmor frequency $\omega = \omega_0 + \gamma \cdot x \cdot G_x$. In this way, the location of a nucleus can be tracked by its precession frequency, by $x = \frac{(\omega - \omega_0)}{\gamma G_x}$. This technique of spatial encoding also known as frequency encoding results in a one-dimensional projection of spin density (as shown in Figure 1.1, 1.2 and 1.3). In practice, a gradient of equal magnitude, opposite direction, and half duration is applied before the frequency encoding gradient to form a gradient echo. The MR signal collected during the presence of frequency encoding (read-out) gradient around gradient echo time (See Figure 1.4 Illustration of gradient echo sequence diagram.Figure 1.4).

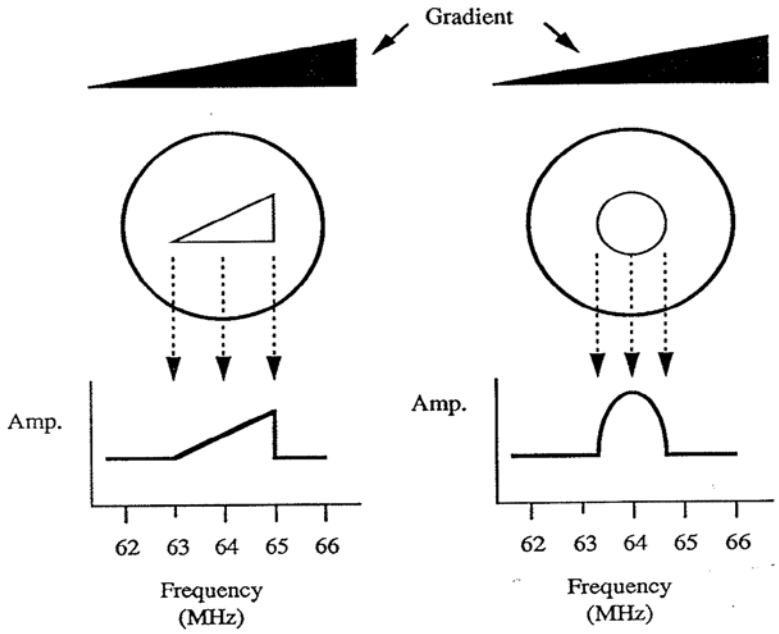

Figure 1.3 Illustration of frequency encoding.

A two-dimensional image is created with the so called 'phase encoding gradient' applied in orthogonal direction to the frequency encoding gradient. Phase encoding is accomplished by applying an orthogonal gradient after the RF pulse and before the frequency encoding gradient for a short period (typically on the order of millisecond). This phase encoding gradient will cause the spins to accumulate certain amount of position-dependent phase in its direction. In an imaging experiment, the data collected at the gradient echo formed by the frequency encoding gradient constitutes a single line of 'k-space'. A full k-space is composed of multiple lines of k-space (typically 64,128 or 256 for convenience of Fast-Fourier-Transform), each line collected with a different phase encoding gradient strength. In case of 2D imaging, raw data (k-space) is the 2D Fourier transform of the target MR object. Inverse Fourier transform is applied to the k-space data in order to obtain corresponding real space image.

1.1.4 Gradient Echo Sequence

An example of imaging pulse sequence - gradient echo sequence (the most important one for our project) is shown below for the 2D version.

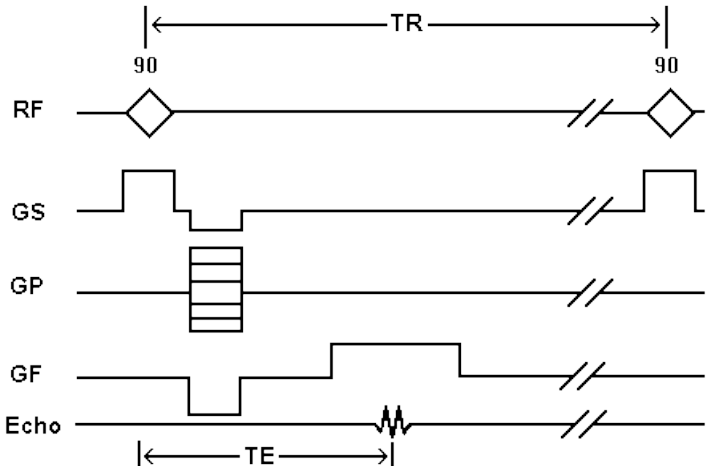

Figure 1.4 Illustration of gradient echo sequence diagram.

Frequency selective RF pulse (usually a small flip angle rather than 90^{o}) is applied in the presence of Gradient along the slice direction, that will excite the spins in a targeting slice.

Followed by a rewinding gradient in the slice direction, which drives back the dephasing of spins caused by the slice-select gradient.

In the phase encode direction, a gradient is applied over certain duration, so that spins along this direction will accumulate position-dependent phase.

In the frequency encode direction (or read out direction), a pre-rewind gradient which has power of exactly half of the read-out gradient is applied. It can be followed by a delay time before the readout gradient is turned on, which will refocus the spins in readout direction at gradient echo time TE (Time of Echo).

A gradient echo is formed when the spins in the readout direction are pulled back in phase. Receiver is turned on during readout gradient to collect signal.

The time between RF pulse and the echo is called Gradient Echo time. The

time delay between two excitation RF pulses is called TR: time of repetition.

Within one TR, one k space line is collected.

During repetitive TRs, everything is carried out the same way except that phase encode gradient varies from time to time, allowing collection of different k space lines.

1.2 Complex MR signal

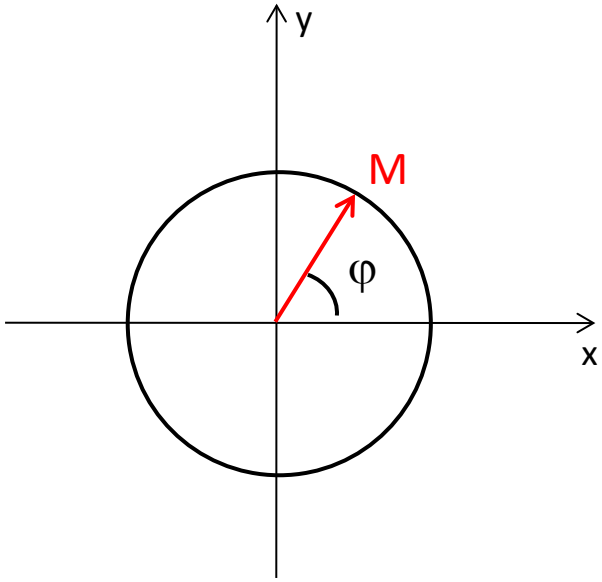

Figure 1.5 Illustration of MR signal components.

The signal that we measure in MRI is a complex number. It can always be written as $A \cdot e^{-i\varphi}$, where A is the magnitude of signal, that represent signal strength, and φ is the phase of signal, that characterizes rotational evolution of nuclear magnetization overtime.

Over years most MRI research and applications were directed to searching for information from the magnitude of signal. It can be weighted by different signal decay mechanisms by carefully designed pulse sequences. Pulse sequences based on contrast mechanisms such as T1, T2, spin density, FLAIR, diffusion, magnetization transfer, etc., are now commercially available from most MRI manufactures.

The phase information of Gradient Echo MRI signal has recently attracted much attention of the MR community. Part of the reason why people did not consider phase information useful is because field variations at all different scales will affect signal phase, and these variations are not only due to intrinsic properties of sample, but largely affected by environmental factors (anything that will affect field homogeneity). However, since It manifests superior gray matter/ white matter contrast and sub-cortical contrast at high field (7 T) (3), and it is extremely easy to obtain – by simple gradient echo sequence, it has become a hot topic in the field of MRI in recent years. However, the nature of phase contrast is under intense debates. By studying properties of protein solutions and rat optical nerve (as model systems) our group has contributed to deciphering the main mechanisms contributing to the phase contrast. This will be discussed in Chapters 2 and 3.

1.3 Multiple Sclerosis

Multiple sclerosis (MS) is a common disease, affecting 2.5 million people world-wide. The clinical course is heterogeneous, ranging from benign disease in which patients live an almost normal life to severe and devastating disease that may shorten life. Despite much research, a fully effective treatment for MS is still unavailable.

There are three subtypes of MS, classified according to their patterns of progression (4-6). 1) Relapsing-Remitting (RRMS), characterized by unpredictable relapses followed by months to years of relatively quiet periods with no signs of disease activity before another relapse. It is the majority of MS population (85-90%), and is the only clinical subtype that responds well to current immuno-modulatory drugs (IMDs). 2) Secondary-Progressive (SPMS) evolves from over 50% of RRMS cases. Patients entering this stage will begin to have progressive neurologic decline between acute attacks. 3) Primary Progressive (PPMS) occurs in about 10% of MS patients. In this case patients have a steady neurologic decline with superimposed attacks from onset.

Symptoms of MS patients are very diverse. It can be almost any neurological symptoms, including changes in sensation, muscle weakness, difficulty moving, difficulties with coordination and balance, problems in speech or swallowing, visual

problems, fatigue, acute or chronic pain, and bladder and bowel dysfunctions. Cognitive impairment of varying degrees and emotional symptoms of depression of unstable mood are also common. The main clinical measure of disability progression and symptom severity is the Expanded Disability Status Scale (EDSS)(7).

Cause of MS is not definite. It is likely to occur as a result of some combination of genetic, environmental and infectious factors (4), and possibly other factors like vascular problems (8).

The pathology of this disease is rather complex - many processes co-exist in the CNS (e.g. inflammation, demyelination, axonal damage and repair mechanisms). Inflammatory CNS demyelination with relative preservation of axons has been considered the pathologic hallmark of MS, but it has been known for many years that axonal loss also frequently occurs in MS (9,10). In principle, the functional deficits in MS caused by inflammation and demyelination can be reversible. In contrast, the damage to axons and neurons is likely to be irreversible.

Complexity of MS and lack of clinical diagnostic tools capable of identifying different specific aspects of MS stimulate numerous investigators to continue search for new

diagnostic methods. Especially important is a problem of early diagnostic as much accumulating data indicate that early treatment is beneficial to decrease ultimate disability in MS (11).

1.4 Magnetic Resonance Imaging in MS

As a non-invasive tool, Magnetic resonance imaging (MRI) plays a key role in MS diagnosis (12,13). Numerous MRI techniques have been proposed over the years. Among most widely used are conventional T1-weighted (T1W), T2-weighted (T2W) and FLuid Attenuated Inversion Recovery (FLAIR) imaging techniques.

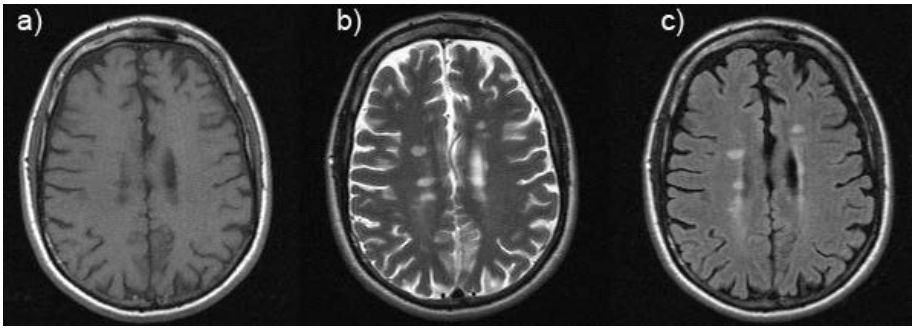

Figure 1.6 Example of clinical standard MRI used for monitoring MS (obtained in our laboratory). a) T1-weighted image, b) T2-weighted image, c) FLAIR.

As shown in Figure 1.6, in T2W image, WM appears dark, and CSF appears bright, with GM in between of them. MS lesions show heterogenous intensity between WM and CSF, but are always brighter than WM – so called hyperintense appearance. In FLAIR images CSF signal is suppressed, so that lesions are visually more

detectable. This is most frequently used in clinical scans in MS subjects. In T1W image on the other hand, WM demonstrates itself as bright, and GM as gray, CSF as dark gray. MS lesions that show up on T2w images do not always came out on T1w image. Those that show up on T1w as hypointense are often called black-holes or grey-holes, indicating severer tissue damage than those that are not seen on T1w. This is the only conventional sequence that provides information about the severity of the MS lesion

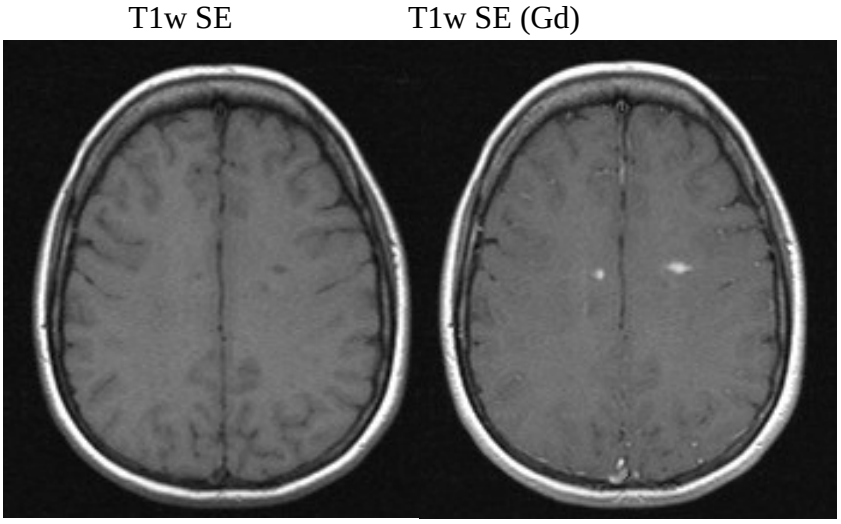

Figure 1.7 Example of clinical standard MRI used for monitoring MS. left: T1-weighted spin echo image; right: T1w-SE image with Gd-enhancement.

T1w image is also used for detecting ‘active lesions’, where administration of gadolinium (Gd) based contrast agent is needed. Because Gd shortens T1 relaxation time constant, the T1w image post-contrast will immediately have brighter blood vessels. Thus if there is a leak in blood-brain barrier (BBB), Gd will

find its way in brain tissue – lesion area – and the lesion will light up as ‘enhanced lesions’. Since BBB breakdown allows immune cells to infiltrate in the brain tissue, causing the known demyelination (14), the Gd-enhanced lesions are often referred to as ‘active lesions’.

The volume of T2W lesions is often used as a secondary endpoint in clinical trials, but it does not correlate well with MS disability (11). This is due to multiple factors, including not only inherent imaging limitations, but also that volumetric measures do not take into consideration lesion locations which determine the functional systems affected, do not include most gray matter lesions. This paradox has been attributed to the complexity and heterogeneity of the underlying tissue damage in MS, to the different effects on function caused by different lesion locations, as well as to variable degrees of neural plasticity among patients. Lack of strong correlation between clinical findings and standard imaging is especially noted in the progressive clinical subtypes (15,16), the subtype where effective treatments are most needed. Indeed, a “plateau effect” between T2W lesion volume and disability has been reported after MS disability reaches a certain level (15,16). Better quantitative imaging is particularly urgently needed for evaluation of new therapies for progressive MS subtypes in a timely fashion(17,18).

Several advanced MRI techniques are also used as research tools to study MS. Among them are magnetization transfer contrast imaging (MT), MR spectroscopy (MRS), and Diffusion Tensor Imaging (DTI).

MT measures the exchange of nuclear magnetization between bound (macromolecular associated) and free (mobile) water ^{1}H in tissue (19,20). Following selective saturation of the pool of bound ^{1}H using a radiofrequency pulse, the image intensity of mobile $^{1}H_2O$ is reduced due to the magnetization exchange process. The ratio of MR signal intensities of selectively saturated vs. non-saturated experiments, defined as magnetization transfer ratio (MTR) changes with loss of myelin and axons in MS and can be used as a measure of MS pathology (21,22), and correlates inversely with disability (23). Thus far, MT has not been widely used except in research studies. MTR would be difficult to use as a surrogate endpoint in multi-center trials due to site-to-site differences.

Another imaging method used primarily in research studies to assess underlying pathology in individual MS lesions is MR spectroscopy (MRS). In CNS, in vivo ^{1}H MRS measures the presence and relative amounts of various tissue metabolites such as N-acetylaspartate (24), choline, creatine, etc. (25). Because NAA derives almost exclusively from mature axons and neurons (9), its persistent reduction is considered a specific indicator of axon loss, damage, or dysfunction. Moreover, reduced NAA is found in the NAWM of some relapsing-remitting (RRMS),

secondary progressive (SPMS), and primary progressive (PPMS) MS patients (26), and the degree of reduction may differentiate SPMS from RRMS (27). Overall, NAA appears to be a meaningful neuroimaging marker for evaluating MS pathology, specifically axonal injury (28,29). However, MRS suffers from long acquisition time, coarse spatial resolution limiting its sensitivity and universal applicability.

Diffusion Tensor Imaging (DTI) provides quantitative data on the rate and direction of water diffusion (30). DTI has the potential to identify and differentiate axon loss/injury from demyelination, as shown in several animal model studies (31-35). The major limiting issue with DTI at present is that it is still labor-intensive to obtain high quality quantitative data routinely.

So far, amongst the best of the correlations between standard imaging methods and clinical function occurs with chronic T1W hypointensities. The volume of T1W hypointensities, or “black holes,” correlates, albeit modestly, with disability (11,16,18). The better correlation between “black holes” volumes and disability is likely because chronic MS lesions that are hypointense on T1W have more axon loss than those that are not (18,36). However, even the determination of what constitutes a “black hole” is subjective and non-quantitative. There are degrees of “blackness” of T1W hypointense lesion. Just because two “black holes” may

occupy the same volume doesn't mean they have the same severity of underlying pathology.

The image contrast in the standard "weighted" spin-echo sequences depends not only on the MR relaxation time constants of the brain tissue but also on the parameters of the pulse sequence. This non-biological dependence may lead to an incorrect estimation of the black hole load, as lesions may not be apparent when image contrast is poor. These shortcomings can be overcome by using recently-proposed approaches based on measuring tissue T2 and T1 relaxation times instead of using T2- and T1-weighted images(37,38). Based on published data, this would also allow improved differentiation among types of MS pathologies. Importantly, a recent study in autopsied MS brain tissue showed good correlation between T1 and T2 relaxation time constants and MS pathology (38). Correlations with another imaging measure, magnetization transfer ratio, MTR were not as strong. These new findings opened a door for using MRI relaxation time constants as quantitative markers of tissue damage in MS. However, the proposed quantitative methods (37,38) are not practical, even for clinical trials, because of the long time needed to produce accurate quantitative T1 and T2 maps.

GEPCI technique developed in our laboratory (39-41) can aid in solving this problem and differentiate the degree of "blackness" by quantitatively measuring

tissue T2* relaxation time constant in a clinical acceptable time (< 8 min). It offers a scoring method for monitoring Multiple Sclerosis based on the quantitative T2* maps generated from magnitude information of gradient echo signal. Herein we demonstrated a strong agreement between GEPCI quantitative scores and traditional lesion load assessment. We also established a correlation between GEPCI scores and clinical tests for MS patients. We showed that this correlation is stronger than that found between traditional lesion load and clinical tests. Such studies will be carried out for longer period and on MS subjects with broader range of disease severity in the future.

1.5 Dissertation Overview

Chapter 2 and Chapter 3 focus on studying the biophysical mechanism behind phase contrast in brain tissue. Experiments are carried out on carefully designed model systems.

Chapter 2 deals with magnetic susceptibility effects. The theory of correctly relating susceptibility to the frequency shift that we measure is proposed. Validation experiments *in silico* as well as *ex vivo* are described in this chapter.

Chapter 3 is about the relative magnitude of susceptibility effect mentioned in the previous chapter and the exchange effect which also shifts MR frequency. The

experimental setup that allows clean separation of these two effects is described; experimental results and validation experiment of this method are also presented in detail.

Chapter 4, Chapter 5 and Chapter 6 brings our investigation *in vivo*, which include both healthy volunteers and MS subjects.

Chapter 4 lays out all the experimental considerations in GEPCI technique involved in the following chapters. The first section describes the parameter optimization; model of the signal is discussed in the second section, multiple derived contrasts from GEPCI technique are also included in this chapter.

Chapter 5 presents the method for implementing GEPCI technique to assist with evaluation of the MS disease. Quantitative tissue damage score is introduced, applied to MS subjects. Comparison between GEPCI measurement and clinical standard evaluations is performed.

Chapter 6 presents the application of the theory described in chapter 2 to the MS disease. It made the effort of bridging understanding of MR signal frequency to the pathology of MS. MS abnormalities on phase images are identified. And theoretical explanation of data and its relationship to corresponding pathology is presented.

Chapter 7 closes out the dissertation by summarizing the specific accomplishments of this study, and also proposes several interesting future directions beyond this study.

Chapter 2 Biophysical Mechanism behind MR Signal Phase – Susceptibility effect[1]

2.1 Introduction

Phase MR images obtained by gradient-recalled echo protocols provide greatly enhanced contrast in the brain at high magnetic fields (3,42-45), which allows visualization of biological structures within gray matter (GM) (46) and white matter (WM) that are distinct from conventional T1-weighted and T2-weighted images. However, the biophysical origin(s) of the phase (frequency) contrast is not well understood, and has been ascribed to a variety of phenomena: (i) susceptibility effects induced by differing tissue chemical composition, specifically including differences in iron (47-49), deoxyhemoglobin (50,51), proteins (52,53), and myelin content (54); (ii) magnetization exchange effects between "free" water and macromolecules (42,55,56) and (iii) possible anisotropy of tissue magnetic susceptibility (57,58). A role for myelin was suggested by a report demonstrating that demyelination leads to a loss of phase contrast between WM and GM (54,59). It has also been shown that the phase contrast between WM and cortex can be principally attributed to variations in myelin content (60). However in contradistinction phase contrast is very small between WM, a myelin rich structure,

[1] Part of contents in this chapter have been published in Luo J, He X, Yablonskiy DA. Magnetic susceptibility induced MR Signal frequency shift in white matter. Proc. Int. Soc. Magn. Reson. Med. 2012; 415.

and cerebrospinal fluid (CSF) where myelin is essentially absent (3,61). To explain this curious phenomenon, He and Yablonskiy (61) introduced a new theoretical concept called the Generalized Lorentzian approach. An important insight from this conceptual framework is that the local contribution to the MRI signal phase does not depend solely on the bulk magnetic susceptibility of the tissue, but also on the "magnetic architecture" of the tissue – i.e., the distribution of magnetic susceptibility inclusions (lipids, proteins, iron, etc) at the cellular and sub-cellular levels. This theory explained why phase contrast is essentially absent between WM and CSF and provided a conceptual platform for quantitative interpretation of data from MR phase imaging of white matter diseases.

Herein the of "Generalized Lorentzian" concept is validated using *ex vivo* rat optic nerve as a model system. Representative of pure white matter, the simple geometry of isolated optic nerve provides a well-defined cylindrical shape that minimizes global magnetic field distortions and contamination from neighboring tissues.

2.2 Theory

2.2.1 Magnetic Susceptibility

Magnetic susceptibility describes how a substance reacts to the presence of external magnetic field B. $M = \chi \cdot B$. M is magnetization defined as a substance

magnetic moment per unit volume. There are three different kind of materials categorized according to their reaction to magnetic field: paramagnetic, diamagnetic, and magnetically ordered substances (ferromagnetic, anti-ferromagnetic and ferrites).

Paramagnetic substances usually have unpaired electrons and positive χ on the order of 10^{-3} at room temperature Their *M* has the same sign as *B*. Diamagnetic substances have no unpaired electrons their χ is 10^{-3} smaller than paramagnetic substance – it is on the order of ppm, and it is negative - *M* has an opposite sign compared to *B*. In magnetically ordered substances unpaired electrons are aligned with respect to each other and their magnetic susceptibility can be several orders of magnitude bigger than in paramagnets.

As it comes to human brain tissue that we are interested in, majority of the mass is diamagnetic, such as water, lipids, proteins. Iron (Fe^{2+} or Fe^{3+}) on the other hand is paramagnetic. Since there is only trace amount of iron (usually about 10^{-5} g/g wet), overall magnetic susceptibility of brain tissue is negative. It is not surprising to find that as complex structure as brain, its susceptibility is not homogenous. For example myelin with susceptibility of χ_m, has magnetization $M_m = \chi_m \cdot B$ which is different from magnetization of surrounding substances and will create additional

magnetic field upon itself and surrounding cytosol environment, resulting in an inhomogenous magnetic field at the cellular and subcellular levels.

Since signal phase is often thought of as directly related to magnetic field distribution, the variations of susceptibility of brain tissue, although small, plays a very important role in the phase contrast that we observe in the brain. To unveil the relationship between the tissue susceptibility and signal phase that we measure, we need to answer two questions: 1) what is field *b* in the tissue area, and 2) what is the relationship between *b* field and MR signal phase?

2.2.2 The signal phase that we measure

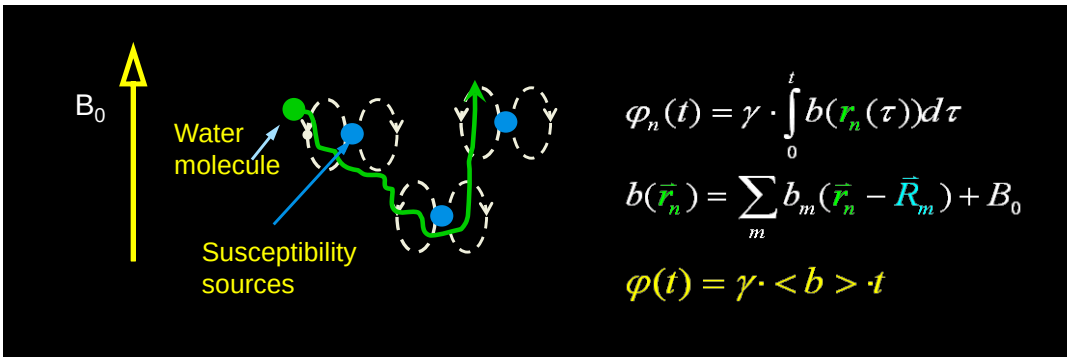

Figure 2.1 Schematic of water molecule moving around surrounding susceptibility sources.

In brain imaging, MRI signal coming from a given voxel is the sum of all signals generated by nuclei in the specific voxel.

$$S(t) = \sum_n \exp(-i\varphi_n(t)) \qquad [2.1]$$

As drawn in Figure 2.1 there are multiple susceptibility inclusions in the voxel – lipids, proteins, iron (all marked with blue dots). Water molecule (green dot) is moving around them all the time due to diffusion. So phase accumulated by single nucleus should be expressed by the integral of *b* field felt by this water molecule through the trajectory over time. $b(\vec{r})$ at each given point is affected by all of its surrounding susceptibility inclusions. Since water molecules that are within characteristic diffusion distance (about 1μm) sample experience more or less the same environment, their signal phase can be expressed as proportional to $< b >$.

One way to find $< b >$ is called 'Lorentzian Sphere Approach'. It borrows the idea proposed by Lorenz (1901), that $< b >$ can be considered as a sum of $< b >_{far}$ and $< b >_{near}$ - two parts separated by an imaginary sphere (demo in Figure 2.2).

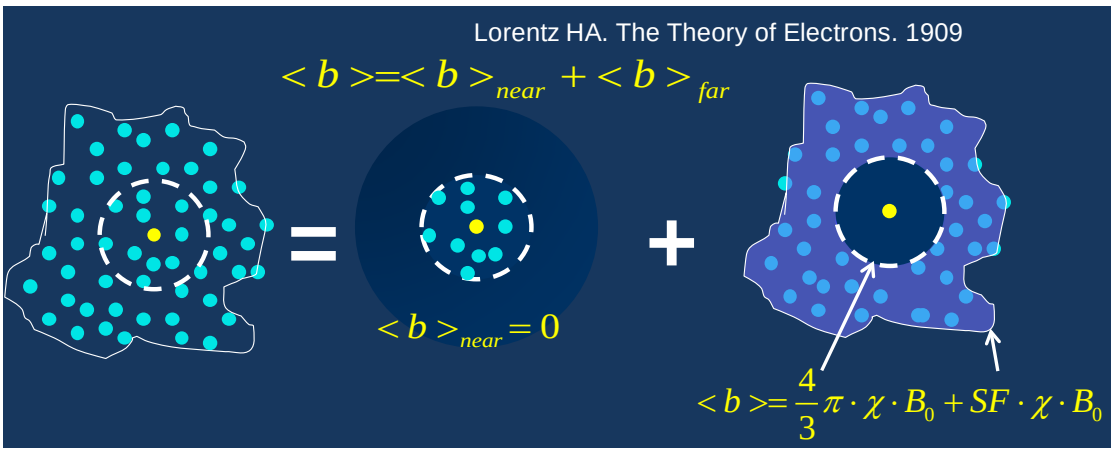

Figure 2.2 Schematic of Lorentzian Sphere Approach.

Due to diffusion and the fact that average field outside a dipole is zero, the $< b >_{near}$ field is zero. The $< b >_{far}$ on the other hand (since all the susceptibility inclusions are far away from the nuclei of interest) can be seen as a field generated by a homogenous media. Thus $< b >$ depends on two things: 1. Lorentzian factor, that is a spherical boundary with vacuum on the inside and susceptibility χ on the outside; 2. The Shape Factor, which varies from different global shapes of the whole object. For example, if global shape of object is also a sphere, then Shape factor will be $(-4/3)\pi$, if it is an infinitely long cylinder, SF will be $-2\pi \cdot \sin^2 \alpha$.

Frequency shift Δf due to the presence of external magnetic field can be expressed as a sum of two terms (62). First term describes effects of global shape of the sample:

$$\left.\frac{\Delta f}{f_0}\right|_{shape} = SF \cdot \chi \qquad [2.2]$$

and the second term describes the short-range, structure specific effects (i.e., dependent upon the specific spatial arrangement of magnetic particles/dipoles) and is generally referred to as the contribution from Lorentzian sphere:

$$\frac{\Delta f}{f_0} = \frac{4}{3}\pi \cdot \chi \qquad [2.3]$$

Here f_0 is the base Larmor frequency, χ is the volume magnetic susceptibility of the liquid sample, and SF is a shape factor dependent on a global shape of the object.

The Generalized Lorentzian Approach (He and Yablonskiy) adds a very important consideration to the Lorentzian Sphere Approach – symmetry of the tissue microscopic structure. It says that if tissue has very regular architecture that has a scale much larger than the characteristic distance of water diffusion, then the selection of lorentzian cavity needs to be modified based on the actual arrangement of macromolecule/susceptibility inclusions. Particularly in the brain white matter, the axons have very specific geometry. A large amount of magnetic inclusions are aligned along axonal direction such as neurofilaments, and myelin sheath. Some can run for cm's long. When doing separation of $< b >_{near}$ and $< b >_{far}$ as we did before, we need to choose our Lorentz cavity as a cylinder. Then Lorenz factor will be $-2\pi \cdot \sin^2 \alpha$, and shape factor depends on brain geometry on the macroscopic level.

2.2.3 Frequency shift of MRI signal in a solution surrounding optic nerve:

The magnetic susceptibility of the nerve is comprised of magnetic susceptibility of longitudinal components/structures χ_L and magnetic susceptibility of isotropic

components/structures χ_{iso} .The homogeneous medium surrounding the nerve has magnetic susceptibility χ_e . In the imaging plane which presents a cross-sectional view of the nerve in the NMR tube, the nerve-induced frequency shift $\Delta f_e / f_0$ experienced by the homogeneous medium outside the nerve is described by the well-known equation as follows:

$$\left.\frac{\Delta f_e}{f_0}\right|_{r>r_0} = 2\pi \cdot (\chi_{iso} + \chi_L - \chi_e) \cdot (\frac{r_0}{r})^2 \cdot \cos(2\theta) \cdot \sin^2 \alpha \qquad [2.4]$$

The frequency shift is proportional to the bulk (total) magnetic susceptibility difference between the nerve ($\chi_{iso} + \chi_L$) and the surrounding solution (χ_e). Moving radially away from the nerve, the frequency shift decays as $1/r^2$, r_0 is the radius of the nerve. The angular dependence of the pattern of the frequency shift in the MR imaging slice plane is described by the angle θ between coordinate of interest in the plane and the projection of magnetic field B_0 onto plane (Figure 2.3); α is the angle between B_0 and long axis of the nerve. When $\alpha = 0°$, the nerve is parallel to B_0, there should be no frequency shift in the homogeneous medium outside the nerve; whereas when $\alpha = 90°$, the frequency shift effect is maximal. Integrating over all angles θ , the average frequency shift induced by the nerve on the external medium is zero.

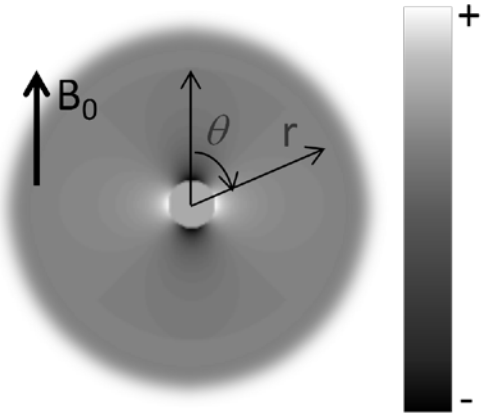

Figure 2.3 Illustration of the secondary field, generated by the optic nerve when B_0 is perpendicular to the axis of the nerve Eq. [2.4].

2.2.4 Frequency shift of MRI signal between inside the nerve and the outside solution surrounding optic nerve

When B_0 field is parallel to the long axis of the nerve, the global shape factor SF = 0 (long cylinder approximation), and the optic nerve frequency shift induced by the longitudinal structures within the nerve is equal to zero (Eq. [2.2] : Lorentzian cylinder). In this case, the only frequency shift observed between inside the nerve and the external homogeneous medium $\Delta f_{i-e} / f_0$ is that induced by the isotropic components, $\frac{4}{3}\pi \cdot (\chi_{iso} - \chi_e)$ per Lorentzian sphere, Eq. [2.3]. In the case when B_0 forms an angle with the long axis of the sample, the global shape factor $SF = -2\pi \cdot (\chi_{iso} + \chi_L - \chi_e) \cdot \sin^2 \alpha$, the Lorentzian cylinder contribution of the intra-nerve longitudinal structures is $= 2\pi \cdot \chi_L \cdot \sin^2 \alpha$, and the Lorentzian sphere contribution of isotropic structures is still $\frac{4}{3}\pi \cdot (\chi_{iso} - \chi_e)$. Including a possible macromolecule exchange effect (which would not depend on the angle between the

long axis of the nerve and B_0) (42,55), the average frequency shift $\Delta f_{i-e} / f_0$ between inside the nerve and the homogeneous external medium (per Eq. [2.4] the average field induced by the nerve itself in the surrounding media is zero) is:

$$\frac{\Delta f_{i-e}}{f_0} = -2\pi \cdot (\chi_{iso} - \chi_e) \cdot \sin^2 \alpha + \frac{4}{3}\pi \cdot (\chi_{iso} - \chi_e) + MWE \qquad [2.5]$$

A very important feature of Eqs [2.4] and [2.5] is the difference in their dependence on magnetic susceptibility: while Eq. [2.4] depends on the total magnetic susceptibility of the optical nerve ($\chi_{iso} + \chi_L$), Eq. [2.5] depends only on the isotropic component χ_{iso} (longitudinal structures do not contribute to the frequency shift in circular structures)! This would not be the case in a traditional use of the Lorentzian sphere approach where both Eqs. [2.4] and [2.5] would depend on the total magnetic susceptibility ($\chi_{iso} + \chi_L$).

2.3 Materials and Methods

2.3.1 Materials

Pairs of rat optic nerves are harvested from three euthanized rats (Sprague-Dawley). For each subject, one nerve was soaked in 1% PBS buffer, and examined 2~3 hours after death. The other nerve was subsequently fixed with 10% formalin, and examined 1~2 days later.

Two pieces of thin coated copper wires (30 micron diameter) were used to tie the optic nerve at both ends. The [wire-nerve-wire] structure was then threaded through an NMR tube with two open ends. The free ends of the copper wires are then wrapped around both ends of the NMR tube (2.97 mm ID), with the nerve suspending in the middle of the tube (as shown in Figure 2.4). The NMR tube was filled with either 1% PBS or 10% formalin fixative, and sealed tight with parafilm.

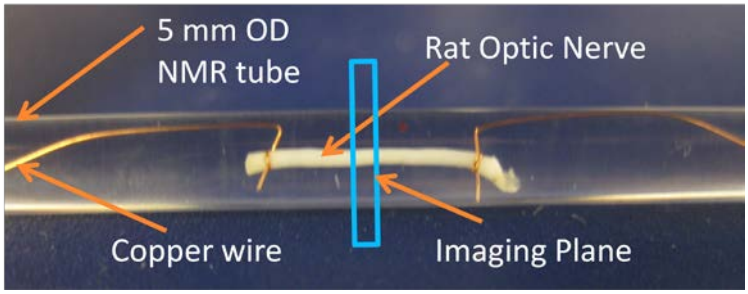

Figure 2.4 Picture of the experimental setup.

2.3.2 MRI Procedures:

Experiments were performed on an Angilent/Varian DirectDriveTM MR scanner based on a 4.7-T horizontal-bore superconducting magnet with a 21 cm diameter inner bore gradient and shim assembly, using a 1.5 cm diameter, laboratory constructed, surface transmit/receive RF coil. Localized shimming employed a STEAM sequence on a 5 x 5 x 5 mm^3 voxel, selected at the mid-point of the optic nerve's longitudinal length. Typical linewidth ~ 8 Hz (range 5 to 12 Hz) was achieved. Data were acquired using a multi-echo gradient echo sequence, on a 1-mm thick slice with 75 x 75 μm^2 in plane resolution. TR 170 ms, first TE 7.4 ms, echo spacing 13.176 ms, flip angle 30 deg, imaging matrix 128 x 128, total

acquisition time 17 min (with 50 averages). The tube was first oriented parallel to B_0 and then rotated 6 times by ~15 degree each time until a perpendicular orientation was reached. Following each rotation, (i) the exact orientation of each rotation was determined from scout images; (ii) the imaging plane of the multi-echo gradient echo sequence was oriented perpendicular to the optic nerve; (iii) localized shimming was performed to minimize field distortions. (Note that if the optic nerve and NMR tube were not perfectly parallel, then imaging plane was made sure to be perpendicular to the nerve.) Experiments were repeated three times on each pair of optical nerves.

2.3.3 Data processing

Data were processed with Matlab® software (The MathWorks, Inc.). Eight fold zero-filling was applied to k-space data in order to increase digital resolution for more accurate estimation of optic nerve radius r_0. Then the data were Fourier transformed into imaging domain (63) and a Hanning filter was applied to reduce Gibbs-ringing and signal leakage.

Frequency maps f were determined from phase maps φ corresponding to different gradient echo times TE according to equation $\varphi = \varphi_0 + 2\pi \cdot f \cdot TE$. Phase unwrapping was preliminary performed in the time-domain for each voxel as described in (39).

Evaluation of the optical nerve position and radius:

Knowledge of the radius r_0 of the optic nerve is required to determine the magnetic susceptibility of the optic nerve as per Eq. [2.4]. To find the center of the optic nerve and subsequently measure its radius, a map of the image intensity gradient was generated based on the magnitude image *I*(*x,y*), Eq. [2.6]:

$$G(x,y) = \sqrt{[I(x+1,y) - I(x-1,y)]^2 + [I(x,y+1) - I(x,y-1)]^2} \qquad [2.6]$$

where *x* and *y* are voxel coordinates in the imaging plane. Starting from an initial estimate of the nerve's center coordinate (origin), radial rays were traced across and covering the nerve's full circumference at 2° intervals (i.e., 180 rays in total). Coordinates of maximal ray intensity (maximal image gradient) at each 2° increment outline the first estimate of the edge of the optic nerve. An updated estimate of the nerve's center was found by averaging coordinates of the edge points and the entire process was repeated until convergence was achieved. Finally, r_0 was determined by calculating average distance from the center point to all the edge points.

2.3.4 Field inhomogeneity correction

Before determining the susceptibility of the optic nerve based on the frequency maps, account must be taken of the background field inhomogeneities. This was done by expanding the angular dependence of the frequency map in terms of a Fourier series:

$$f(r,\theta) = f_0(r) + \sum \cos(n\cdot\theta)\cdot f_{nc}(r) + \sum \sin(n\cdot\theta)\cdot f_{ns}(r) \qquad [2.7]$$

where θ is the azimuthal angle, n=1,2,… and r is the distance from the nerve center (Figure 1). The coefficients in this series can be expressed in a standard manner:

$$f_{ns}(r) = \frac{1}{\pi}\oint f(r,\theta)\cdot\sin(n\theta)d\theta; \quad f_{nc}(r) = \frac{1}{\pi}\oint f(r,\theta)\cdot\cos(n\theta)d\theta; \quad f_0(r) = \frac{1}{2\pi}\oint f(r,\theta)d\theta; \qquad [2.8]$$

All coefficients in front of the harmonics can be further expressed as Taylor series:

$$f_n(r) = \sum a_{nm}\cdot r^m \qquad [2.9]$$

where m=0,1,2,… The only exception to this expression is the $f_{2c}(r)$ term is associated with $\cos(2\theta)$ because the field generated by the optical nerve also contains the term $\cos(2\theta)$, Eq. [2.4], hence this term should be written as

$$f_{2c}(r) = \sum a_{2m}\cdot r^m + 2\pi(\chi_{iso} + \chi_L - \chi_e)\cdot\sin^2\alpha\cdot r_0^2\cdot r^{-2} \qquad [2.10]$$

As the dipolar term is proportional to $1/r^2$, when one is close to the inner cylinder (the minimum point) the local field is mainly affected by this term, while at larger r, distant from the inner cylinder, the field inhomogeneity plays bigger role. The $f(r)$ curves are first calculated by numerical integration of frequency maps for the distant regions ($r > 2r_0$) according to Eqs. [2.8]. Then coefficients a_{nm} are calculated by fitting Eqs. [2.9] and [2.10] to these curves. Finally, fitting results are used to calculate all terms in Eq. [2.7] (usually up to second order) for all r and θ;

the frequency maps are subsequently corrected by subtracting these terms except for the term $\cos(2\theta)\cdot f_{2c}(r)$.

2.3.5 Evaluation of imaging errors

In-silico experiments - computer simulations of the MRI experiment were conducted to evaluate errors in parameter estimates that might have been introduced by the imaging protocol itself. All programs for data generation and analysis were written in Matlab®. Imaging protocol parameters in the simulations were set to reproduce experimentally employed parameters. 2D *in-silico* imaging data mimicked cross-sectional slices of two infinitely long co-axial cylinders filled with different homogenous media.

The inner cylinder had radius r_0 = 0.32 mm, corresponding to the optic nerve, and the outer cylinder had radius R = 1.87 mm, corresponding to the NMR tube. The field of view was 9.6x9.6 mm^2 and the matrix size was 128 x128. The k-space sampling of the object was calculated according to the following equation:

$$S(k_x,k_y)=\int\int \rho(x,y)\cdot\exp(-i\cdot 2\pi\cdot(k_x\cdot x+k_y\cdot y)+i\cdot\gamma\cdot b(x,y)\cdot(TE+t))\cdot dxdy \quad [2.11]$$

where *TE* is the gradient echo time, *t* is time during readout ($2\pi k_x=-\gamma G_x t$), γ is the gyromagnetic ratio and *b*(*x*,*y*) is the secondary field generated by the susceptibility difference ($\Delta\chi_{i-e}$) between the different homogeneous medium assumed to fill the inner and outer cylinders. This susceptibility difference was set according to a preliminary evaluation measurement: $\Delta\chi_{i-e}$ = - 9.287 ppb. In simulations, *b*(*x*,*y*) inside the inner cylinder was described by the Lorentzian sphere

approach, in this case requiring shape factor of cylinder and Lorentzian factor of sphere, hence $b(x,y) = -(2/3)\pi \cdot \Delta\chi_{i-e} \cdot B_0$. The field surrounding the inner cylinder (present in the annulus between the two concentric tubes) is $b(x,y) = 2\pi \cdot \Delta\chi_{i-e} \cdot (\frac{r_0}{r})^2 \cdot \cos(2\theta) \cdot B_0$. To focus on magnetic susceptibility effects the global field inhomogeneity was neglected and the T2 relaxation time constant was assumed to be infinite for both compartments. The integral in Eq. [2.11] was calculated as a discrete sum over 2048 x 2048 points which is 16x16 times greater than the simulated imaging resolution (128 x128).

Effects of different data processing procedures, such as zero filling and Hanning filtering were evaluated with cylinders perpendicular to B_0. Different combinations of spin densities of inner and outer cylinders (in:out) were selected as 1:2, 2:1, 3:2 and 2:3, bracketing that observed in actual experiments. Finally, the specific TE, image intensity, and *b* field corresponding to experimental data presented in Results were used to estimate r_0 from simulated data with B_0 parallel to the axis of the concentric cylinders. These results were subsequently used for correction of the r_0 estimated from experimental data.

2.3.6 Determination of Magnetic Susceptibility

The bulk magnetic susceptibility of the nerve was determined following field inhomogeneity correction using Eq. [2.10]. Fitting $f_{2c}(r)$ against r^{-2} yields the coefficient $2\pi(\chi_{iso} + \chi_L - \chi_e) \cdot r_0^2 \cdot \sin^2\alpha$, which is then fit to a linear function of

$\sin^2\alpha$ to yield $2\pi(\chi_{iso}+\chi_L-\chi_e)\cdot r_0^2$. Since r_0 is known from measurements described above, the bulk (total) susceptibility $(\chi_{iso}+\chi_L-\chi_e)$ is obtained.

The frequency shift experienced in the interior of the inner cylinder or optic nerve *vs.* surrounding homogeneous-medium was also determined after field inhomogeneity correction. The average frequency shift experienced by the surrounding medium is zero. The frequency shift experienced in the interior of the inner cylinder or optic nerve is calculated by averaging over the area inside the cylinder/nerve (an area around the center point covering less than half of the cylinder/nerve diameter to avoid partial volume effects).

2.4 Results

2.4.1 In Silico Experiments

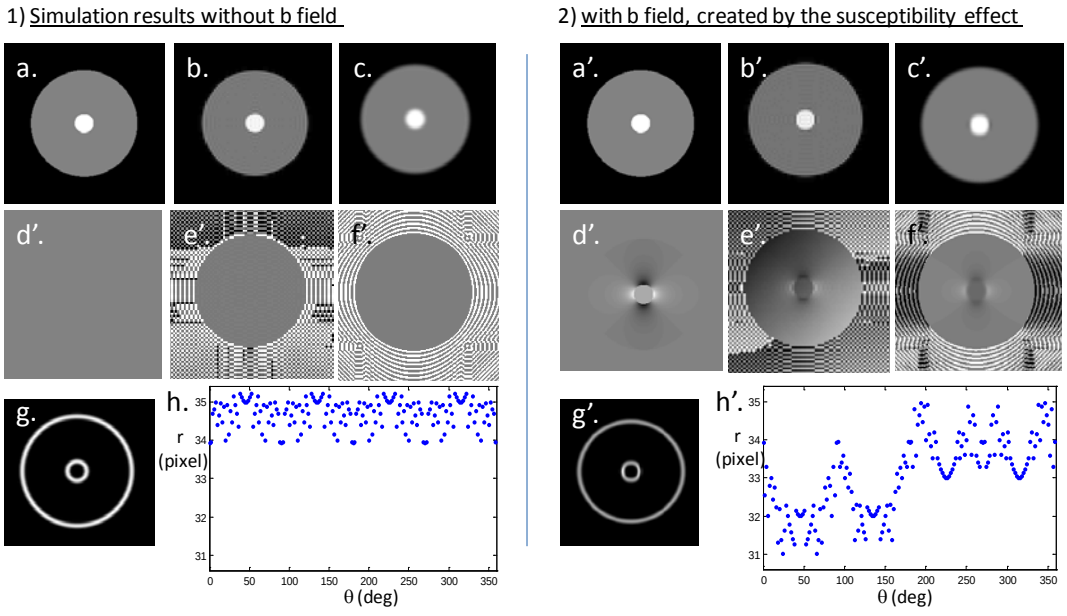

Figure 2.5 An illustration of *in silico* results and procedure for determining radius of

the inner cylinder (input value: 35 pixels). Left panel - results without including susceptibility effect in the simulation; Right panel - results with susceptibility effect. a,a' - objects created for simulation; b,b' - original magnitude images obtained from simulated data; c,c' - magnitude images obtained after zero filling and Hanning filter; d,d' - field maps used in simulations; e,e' - original phase images obtained from simulated data; f,f' - phase images obtained after zero filling and Hanning filter; g,g' - gradient maps of the magnitude of the processed image (c,c' respectively); h,h' - plots of radius vs. sample points around the cross-section of the inner cylinder.

Two examples of the results of *in-silico* experiment are shown in Figure 2.5. Limited imaging resolution, partial volume effects, and Gibbs ringing artifacts create uncertainties in determining the inner cylinder radius. Even with no susceptibility difference between the two compartments, the simulated data do not provide for an exact determination of the radius of the inner cylinder. The different combinations of spin densities showed the same effect (Table 2.1). In the presence of magnetic-susceptibility-induced field inhomogeneities, the measured radius deviates more from the true (input) r_0, shown in Fig 2.5h'. Moreover, distortion of the cylinder is demonstrated clearly in the plot of radius as measured at different angles about the inner cylinder. This effect results from the static inhomogeneous *b* field, which adds an additional gradient (although small) to the imaging gradient. Herein, since the simulation employed a susceptibility difference between actual nerve tissue and

surrounding solution that was close to the experimental value, it is possible to use the *in-silico* results as correction factors in the processing of the experimental data.

Spin Density Ratio (Inner : Outer)	Estimated r_0 at χ = 0	Estimated r_0 at χ = - 9.287 ppb	Deviation from Input (%)
2 : 1	34.7070	33.0829	-5.4%
3 : 2	34.7070	32.1771	-8.0%
1 : 2	34.7070	36.0424	2.98%
2 : 3	34.7070	36.7514	5.01%

Table 2.1 *In-silico* measured radius of inner cylinder obtained for different 'spin densities' (input radius is 35); simulation was performed with assuming the echo time TE of 20 ms; both Hanning filter and zero filling were applied during data processing.

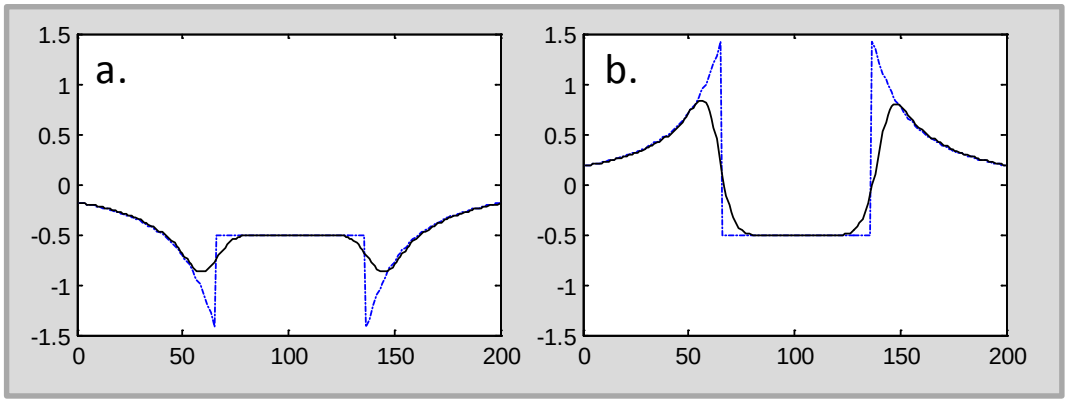

Figure 2.6 Example of the profiles of phase images obtained from *in-silico* data for B_0 oriented perpendicular to the cylinder axis along the read out direction. The frequency distribution arising in the simulation (Lorentzian sphere approach) resulted from an assumed susceptibility for homogeneous medium in the inner cylinder of χ = -9.287 ppb. Vertical scale is phase value in radians; Horizontal scale is pixel number with origin at the center of inner cylinder. a) Profiles through the

center of the inner cylinder along B_0 direction; b) Profiles through the center of the inner cylinder perpendicular to B_0 direction. Solid black lines represent resulting phase after simulation (processed with zero-filling and Hanning filter), blue dotted lines represent the "ideal" phase result which is proportional to the input of susceptibility induced *b* field.

Figure 2.6 shows phase distortions revealed by the in *in-silico* procedure, which arise from magnetic susceptibility effects. Major deviations from the input model parameter are seen at the edges of the inner cylinder. However the central portion and the "tails" of frequency maps around the inner cylinder more closely follow the ideal phase. In fitting *in silico* data to Eqs. [2.9] and [2.10], the data points to be modeled are chosen be sufficiently far from the edge of the nerve so as to avoid the distortions shown in Figure 2.6. For the case of B_0 perpendicular to the cylinder, the frequency shift between the inner cylinder and the average frequency shift outside of the inner cylinder is: $\frac{\Delta f_{i-e}}{f_0} = -\frac{2}{3}\pi \cdot \Delta\chi_{i-e}$. Considering only the central area of the inner cylinder (avoiding partial volume effects) yields $\Delta\chi_{i-e}$ = 9.2875 ppb which is practically identical to the input parameter $\Delta\chi_{i-e}$ = - 9.2867 ppb. Considering the frequency shift outside of the inner cylinder yields, Eq. [2.4], $\Delta\chi_{i-e}$ = 9.3023 ppb, which differs from the input model parameter by only 0.016 ppb or 0.17%.

Spin Density Ratio (Inner : Outer)	Fresh Optic Nerve Mimic	Deviation from Input	Fixed Optic Nerve Mimic	Deviation from Input

	(pixels)	(%)	(pixels)	(%)
3 : 2	34.5537	-1.28%	34.0043	-2.84%
1 : 2	35.4734	1.35%	36.7754	5.07%

Table 2.2 Examples of error in r_0 measured when coaxial cylinders (inner and outer) are parallel to B_0. Input r_0 was 35 pixels; $b(x,y)$ inside inner cylinder was modeled as having essentially the same frequency shifts as encountered in the actual optic nerve experiments. Top row shows the cases when cylinder spin density ratio inner : outer = 3 : 2, sampled at TE = 7 ms; Bottom row shows the cases when spin density ratio inner : outer = 1 : 2, at TE = 25 ms.

2.4.2 Ex vivo experiments

Figure 2.7 demonstrates dependence of the signal phase inside the optical nerve on gradient echo time TE. The data shows that the linearity of phase as function of TE is very good (R^2 >0.99), which means that a set of echo times used in our experiments is not sensitive to the non-linear phase behavior observed in (64-66). Figure 2.8 and Figure 2.9 show examples of magnitude and phase images obtained from the optical nerve.

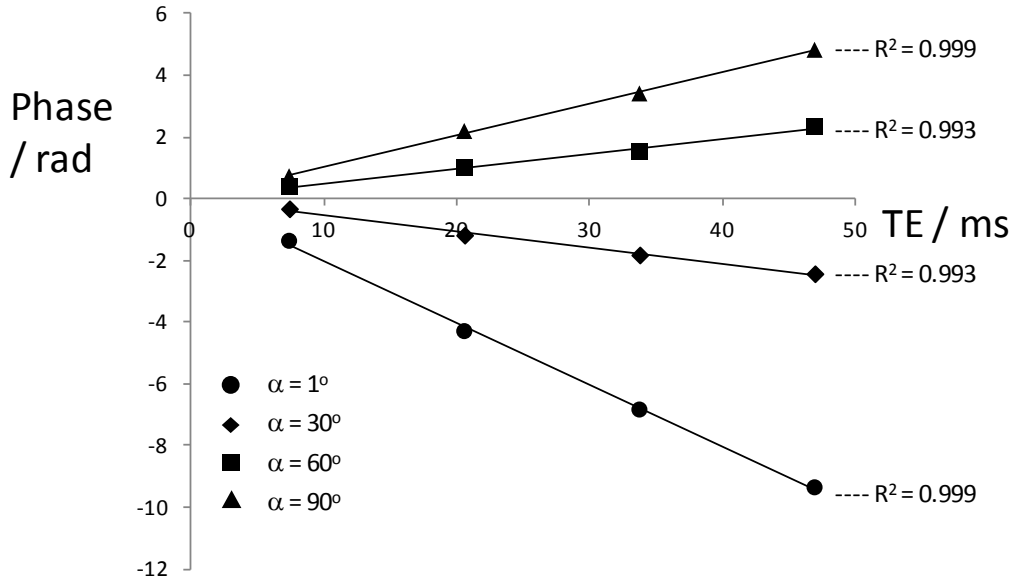

Figure 2.7 Representative examples of signal phase evolution along echo time at different angles (α) to B_0. Experimental data.were taken from inside the optic nerve. The phase at TE=0 was set to zero. The solid lines are linear fits. All four data sets show good linearity.

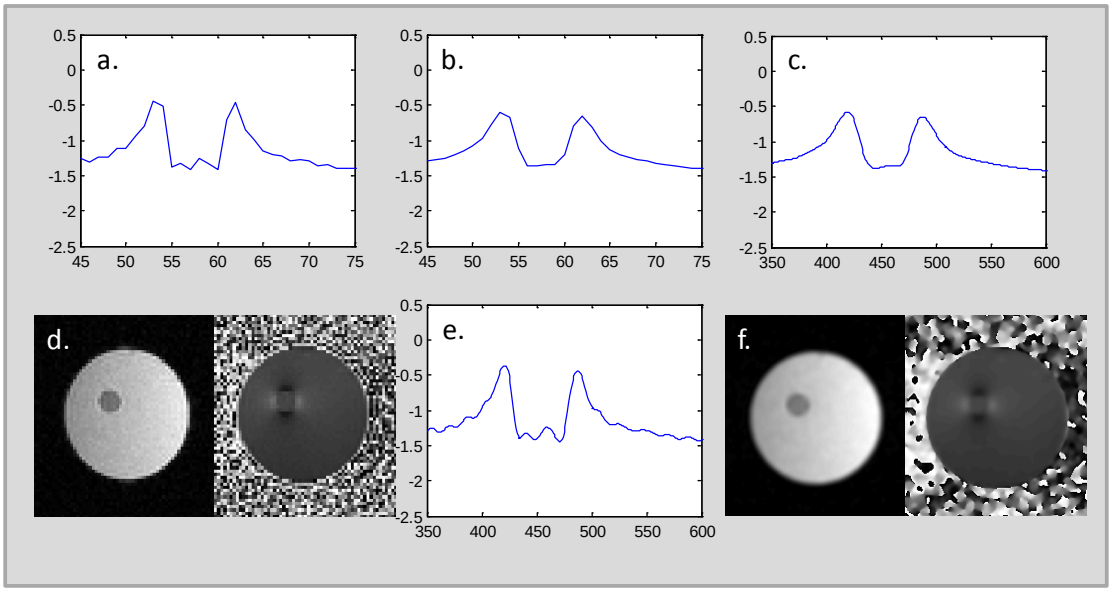

Figure 2.8 Illustration of the results of zero-filling and Hanning filtering of data. Images shown are obtained while optic nerve is perpendicular to the B_0 direction. Profiles through the center of the optic nerve are displayed. a) Profile directly resulting from IFFT of k-space data. b) Profile after Hanning filter was applied to a) to eliminate Gibbs ringing artifact. c) Profile after eight fold zero filling was applied to b) to increase digital resolution. e) Profile after only eight fold zero filling was applied to a), i.e., no Hanning filter. Magnitude and phase images corresponding to cases a) and c) are displayed in d) and f), respectively.

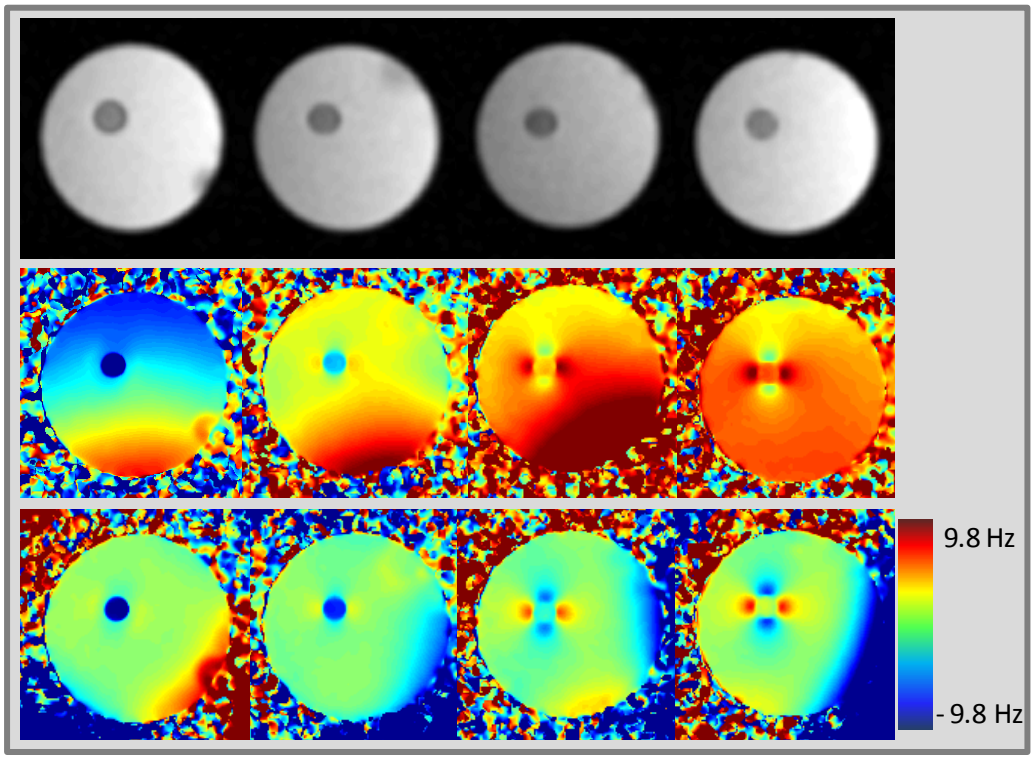

Figure 2.9 An example of experimental data obtained from a fixed optic nerve. Upper row - magnitude images, middle row - corresponding frequency maps, and bottom row - frequency maps after field correction. Maps from left to right show

cross-sections of the optic nerve as the nerve was rotated from parallel to B_0 to perpendicular to B_0 in steps of 30 degrees.

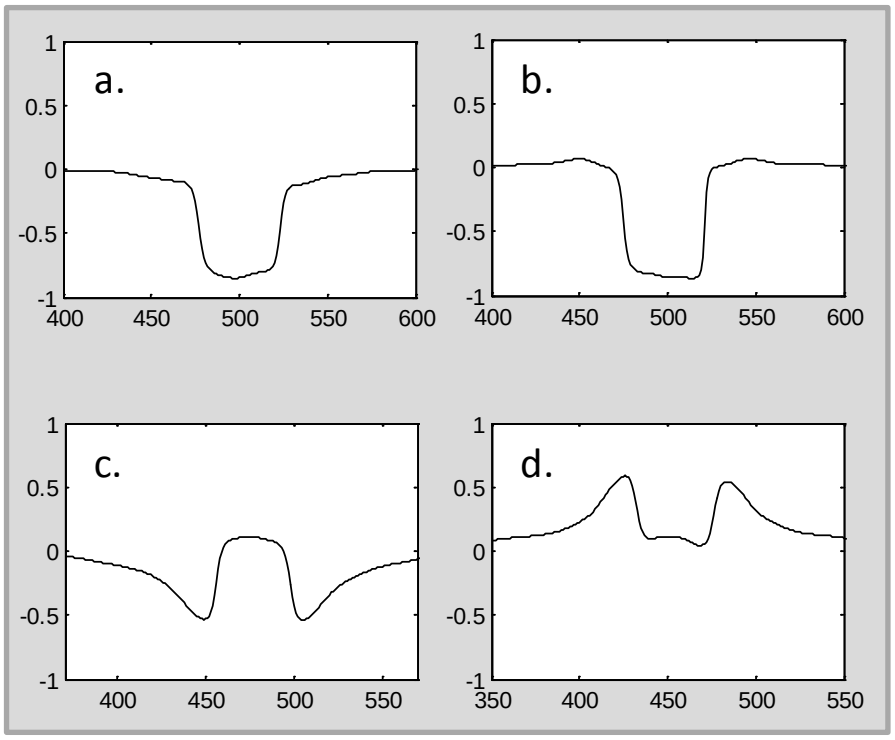

Figure 2.10 Example of the profiles of phase images after field correction. Profiles are drawn through the center of the nerve. Vertical scale is value of phase in radians, horizontal scale is pixel number in the image matrix. a) Profile along readout direction when nerve is parallel to B_0; b) profile along phase encode direction when nerve is parallel to B_0; c) profile along readout direction when nerve is perpendicular to B_0; d) profile along phase encode direction when nerve is perpendicular to B_0.

Field corrected profiles of the phase images for parallel and perpendicular cases are displayed in Figure 2.10. Profiles are taken through the center of the nerve in both horizontal and vertical directions. The frequency shifts described in Eq. [2.4] are clearly demonstrated here. When the nerve is parallel to B_0, it does not induce frequency shift in the surrounding media, whereas when nerve is perpendicular to B_0, it induces maximal frequency shift to the surrounding that decays as $1/r^2$. In agreement with theoretical prediction, the readout and phase encode directions show frequency shift with opposite signs [as cos(2θ) changes from 1 to -1].

Magnetic Susceptibility Measurements

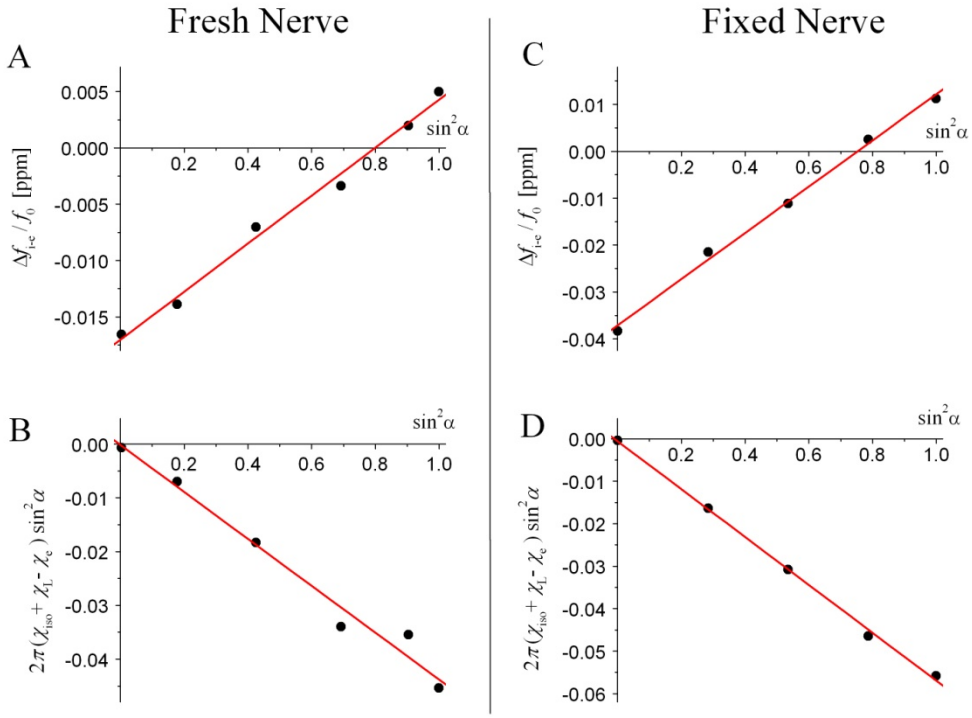

Figure 2.11 Angular dependencies of the frequency shifts for one fresh nerve and one fixed nerve. Filled circles - experimental data; lines - linear fits against $\sin^2\alpha$. Panels A) and C) are frequency shifts of inside nerve *vs.* surrounding media; B) and D) are coefficients in front of $(r_0/r)^2$ in Eq. [2.10] describing frequency shifts induced outside the nerve by magnetic susceptibility difference between nerve and surrounding media.

Fitting Results [ppm]		$2\pi(\chi_{iso}+\chi_L-\chi_e)$	R^2	$2\pi(\chi_{iso}-\chi_e)$	MWE	R^2
Fresh nerve	Rat 1	-0.043	0.978	-0.021	-0.003	0.99
	Rat 2	-0.050	0.999	-0.025	0.002	0.98
	Rat 3	-0.040	0.989	-0.0232	-0.003	0.91
	Average +/- std	-0.044 ± 0.005		-0.023 ± 0.002	-0.001 ± 0.003	
Fixed nerve	Rat 1	-0.062	0.997	-0.052	-0.017	0.99
	Rat 2	-0.056	0.998	-0.049	-0.004	0.99
	Rat 3	-0.049	0.995	-0.035	-0.013	0.97
	Average +/- std	-0.056 ± 0.006		-0.045 ± 0.009	-0.011 ± 0.007	

Table 2.3 Summary of fitting results from three fresh and three fixed optical nerves without correction to radii of optic nerves.

[ppb] r_0 **Uncorrected**	$\chi_{iso}+\chi_L-\chi_e$	$\chi_{iso}-\chi_e$	χ_L	$\chi_e-\chi_w$	$\chi_{iso}+\chi_L-\chi_w$
Fresh Optic Nerve	-7.0 ± 0.8	-3.5 ± 0.3	-3.4 ± 0.7	-2.2	-9.2 ± 0.8
Fixed Optic Nerve	-8.9 ± 1.0	-7.2 ± 1.4	-1.6 ± 0.6	0	-8.9 ± 1.0
[ppb] r_0 **Corrected**					
Fresh Optic Nerve	-7.0 ± 0.9	-3.5 ± 0.3	-3.3 ± 0.8	-2.2	-9.2 ± 0.9
Fixed Optic Nerve	-9.6 ± 1.7	-7.2 ± 1.4	-1.9 ± 0.5	0	-9.6 ± 1.7

Table 2.4 Summary of magnetic susceptibilities calculated from Table 2.3. Numbers represent mean ± standard deviation.

After background field is removed, dependency of the frequency shifts on $\sin^2\alpha$ is plotted in Figure 6. Fitting results from three data sets of both fresh nerves and

fixed nerves are recorded in Table 2.3. If the Lorenzian sphere approximation would be valid, the magnitude of the slopes in $\Delta f_{i-e} / f_0$ vs. $\sin^2\alpha$ plot and $\Delta f_e / f_0 |_{r>r_0}$ vs. $\sin^2\alpha$ plot would have been the same. As we can see, none of the fresh nerve data agree with the prediction from the Lorentzian sphere approximation. Hence Generalized Lorentzian approach should be applied to explain our observations. For fresh nerve, the average result of $2\pi(\chi_{iso} + \chi_L - \chi_e)$ is (-0.044 ± 0.005) ppm, and $2\pi(\chi_{iso} - \chi_e)$ is (-0.023 ± 0.002) ppm. The subsequently estimated $\chi_{iso} - \chi_e$ and χ_L are - (3.5±0.3) ppb and - (3.5±1.1) ppb, respectively. Further, the linearity of fittings is good, which means that the $\sin^4\alpha$ term, as proposed in (57) to describe the susceptibility anisotropy, is negligible in our data. On the other hand, the magnetic susceptibility of longitudinal structures, χ_L, observed in fixed nerves is much smaller. Also note that the bulk susceptibility difference between nerve and surrounding media is consistently different for fresh nerve and fixed nerve by ~ 20%. This difference can be attributed to the difference in experimental conditions – fixed nerves were studied in 10% formalin solution while fresh nerves were studied in 1% PBS solution. To take into account these differences we measured magnetic properties of formalin and PBS and results are presented in section 2.6. While no measurable susceptibility difference between formalin solution and water was found, the susceptibility difference between PBS and water is - 2.2 ppb.

Finally, the intercept of plot $\Delta f_{i-e} / f_0$ vs. $\sin^2\alpha$ is equal to $\frac{4}{3}\pi \cdot (\chi_{iso} - \chi_e) + MWE$, Eq. [2.5], allows estimation of the water-macromolecule exchange effect in the

optic nerve. Result shows that MWE in fresh nerve is negligible, while MWE in fixed nerve is around 0.038 ± 0.007 ppm. These results however cannot be directly attributed to water-macromolecule exchange inside the optical nerve. Indeed, data in Appendix show that both formalin and PBS shift water frequency by non-susceptibility mechanism.

Possible error introduced by the data processing procedure is investigated in the *in silico* experiments. And a major source of error comes from image distortions as demonstrated in Figure 2.5 and Figure 2.6, which has significant effect on the measurement of radius of the optical nerve. If correct number for radius is used, the error of resulting bulk susceptibility measurement is within 0.2%. Since the data we use to fit curves described in Eqs. [2.9] and [2.10] are far away from the edge of nerve, this step should not be affected by the imaging distortion at the edge of nerve. And also according to Eq. [2.4], when nerve is parallel to B_0, there will be no additional field outside nerve, which indicate least asymmetric distortion. We decided to correct the radius of nerve measured in parallel cases, and then use that as 'real r_0' when calculating susceptibility. Corrections on r_0 are applied to experimental data and reported for reference in Table 2.4.

On the other hand, measurement of susceptibility from inside of the nerve is independent on the radius, and thus very accurate. Errors here might come from the fact that the nerve tissue actually has more than one frequency compartments(64-66). Though this effect is not apparent in our data, see Figure 2.7.

2.5 Discussions

It is generally understood that the MRI signal frequency shift induced in biological objects due to magnetic susceptibility effects is dependent on the objects bulk magnetic susceptibility and shape. However, this is not adequate to explain frequency shifts observed in brain white matter. For example, the Lorentzian sphere approach predicts equal slope magnitudes comparing a plot of $\Delta f_{i-e} / f_0$ *vs.* $\sin^2\alpha$ and a plot of $\Delta f_e / f_0 |_{r=r_0,\theta=0}$ *vs.* $\sin^2\alpha$. The fresh nerve results presented herein are clearly not in agreement with this prediction. The Generalized Lorentzian Approach (61) proposed that the underlying microstructure of the object at the cellular and sub-cellular levels should also be included in the model describing the MR signal frequency shift. This is especially important for brain structures such as white matter composed mainly from longitudinally arranged cells (i.e., neurons). Demonstrating this phenomenon in the brain is highly challenging because of complicated underlying structure and generally sufficient resolution of MRI experiments. Herein, the MR signal frequency shift induced by a tract of white matter was determined and compared to the predictions of two theoretical concepts – Lorentzian sphere approach and the generalized Lorentzian approach (cylinder model). The cylindrical geometry of isolated optic nerve, a tract of axonal bundles running parallel to each other, provides a well-defined shape that minimizes distortions in B_0 and eliminated contamination from neighboring tissues. These attributes make it possible to accurately measure the bulk magnetic susceptibility of

freshly harvested optic nerve ($\chi_{iso} + \chi_L - \chi_w = -9.2 \pm 0.8$ ppb) as well as the longitudinal component ($\chi_L = -3.4 \pm 0.7$ ppb).

Quantitative measurement of frequency shifts is crucial for this study. Simulations generating *in silico* image data were performed to test the bias of post-processing procedures. As demonstrated in Figure 2.6, the transition point from inner cylinder to outer cylinder is greatly affected by imaging resolution and also field distortions. Similar profiles are also observed in *ex vivo* data (Figure 2.10). Moreover image definition of the circular edge of inner cylinder can be distorted when the cylinder is not parallel to B_0 (Figure 2.5h'). Fitting data outside the nerve substantially distant from the transition point ($r > 2r_0$) and then extrapolating the back to smaller r avoids this artifact and provides an accurate determination of $2\pi(\chi_{iso} + \chi_L - \chi_e) \cdot r_0^2 \cdot \sin^2\alpha$. Employing the exact r_0 and α, the deviation between the derived susceptibility and the 'true value' (model parameter value(s) input to the simulation) is only 0.17%.

With this insight gained from the simulations, the radius r_0 of the nerve measured with cylinder parallel to B_0, was used in combination with simulation results in Table 2.2 to get "true r_0" when calculating susceptibility since Eq. [2.4] shows that when the nerve is parallel to B_0 there will be no additional field outside the nerve and thus the least asymmetric distortion. Experimental results on susceptibilities are reported with and/or without corrections on r_0 in Table 2.4. Finally, although $\sin^2\alpha$

determined each time the tube was rotated is, of course, not be perfectly accurate, fitting to multiple measurements at 5 to 7 different values of α ensures the accuracy of the final result. While the frequency shift inside of the nerve is, in principle, independent of the nerve radius r_0, partial volume effects on the measurement were avoided by evaluating only the area for which $r < 2r_0$.

Effects of magnetization exchange might also be a significant factor in determining the frequency shifts in the biological tissue (42, 55-56). In the experiments herein, magnetization exchange will contribute to the frequency shifts separately from the susceptibility effect. As magnetization exchange will not be dependent on the angle formed between nerve tissue and B_0, it enters Eq. [2.5] as a constant term. In principle, these experiments should allow determination of the exchange effect, as described in "Results". These findings, however, cannot be directly attributed to water-macromolecule exchange inside the optical nerve since data in the "Appendix" show that both formalin and PBS shift the water MR frequency by non-susceptibility mechanisms and the volume fraction of either formalin or PBS that penetrates inside of the nerve is unknown.

A multiple compartment model has been proposed to explain the MR frequency shifts between grey matter and white matter (64-66). The measurements obtained from voxels inside the optic nerve would need to be reexamined if multiple

frequency compartments were found to originate within one voxel. This phenomenon does not appear to be significant (Figure 2.7) within the TE range that used here.

Anisotropic susceptibility of white matter has also been proposed to explain MR frequency shifts observed in white matter. Experimental data herein demonstrate that the MR frequency shifts observed in optic nerve tracts can be fully described by the generalized Lorentzian concept (Lorentzian cylinder model) in the absence of postulating an anisotropic susceptibility for white matter.

2.6 Magnetic Susceptibility and Exchange Effects in External Media

Separate measurement of susceptibility and exchange effects were performed to exclude the contribution from external media in our experimental setup. Since the fresh nerve was measured while suspended in 1% PBS solution, and fixed nerve was done in formalin.

NMR Experiments: This experiment applied the method for simultaneously determining the susceptibility effect and exchange effect employed in a previous publication (Luo *et al*.) details of experiments can be found there (or in Chapter 3). A scheme employing coaxial tubes was employed. The inner tube (2mm outer diameter) was filled with water and 0.5% Dioxane; the outer tube (5mm outer

diameter) was filled with aqueous solutions containing either 1% PBS or 10% formalin (exact same solutions that were used in optic nerve experiments), including 0.5% Dioxane. MR experiments were conducted on a Varian INOVA 500-MHz (11.74-T) vertical bore analytical spectrometer. Samples did not contain D_2O, which is commonly used for field/frequency locking and shimming. A separate coaxial tube containing a D_2O/H_2O mixture was used for shimming (maximizing B_0 homogeneity). After shimming, the sample was loaded, and FIDs were collected. Radiation damping was minimized by detuning the receiver coil and employing a reduced filling factor (5 mm outer tube diameter in a RF coil greater than 10 mm in diameter).

Results:

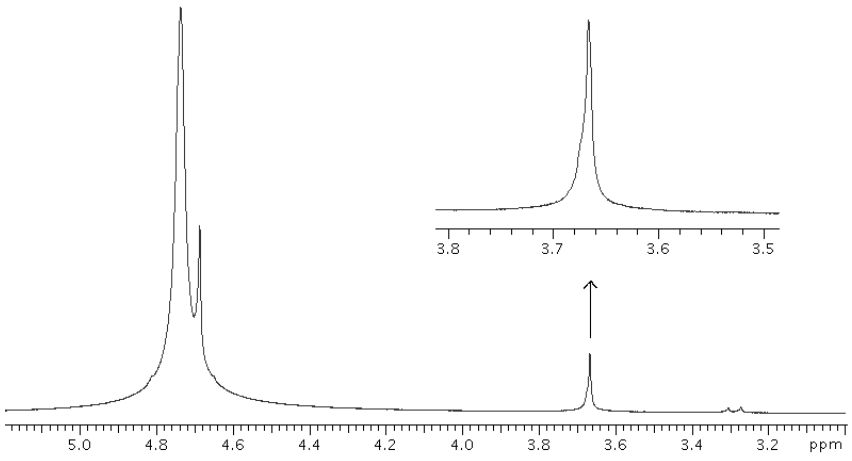

Figure 2.12 Results for formalin measurement.

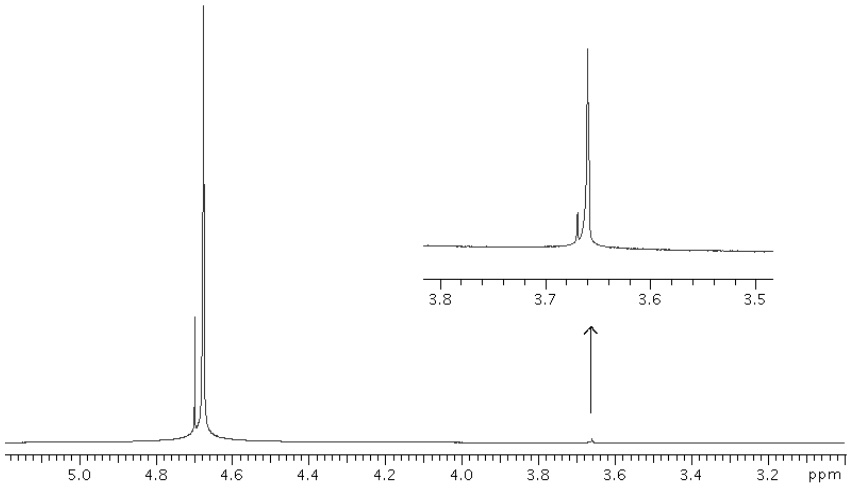

Figure 2.13 Results for PBS measurement.

As spectra in Figure 2.12 and Figure 2.13 show, the MR frequency near 3.6 ppm is identified as dioxane and the peak near 4.7 ppm is identified as water. Regarding neighbor resonances originating from the same ^{1}H species, the resonance with greater intensity is from species in the outer tube of the co-axial set, and the lower intensity resonance is from species in the inner tube. Since the dioxane MR frequency is considered reflective only of a susceptibility effect, the frequency shifts between dioxane in the inner and outer tubes reflects the susceptibility deviation of PBS or formalin solutions (here compared to pure water). Formalin did not induce discernible frequency shift on dioxane resonances, whereas PBS induced a -0.0093 ppm shift compared to pure water. However, the ^{1}H water MR resonance frequency is affected not only by the susceptibility effect, but also by other effects - pH, exchange with other labile protons, etc. Figure 2.12 shows that the principal

formalin ^{1}H resonance has a frequency shift induced by non-susceptibility effects of +0.050 ppm. Figure 2.13 shows that the PBS solution has frequency shifts induced by non-susceptibility effects of -0.013 ppm. These results are important factors to consider when understanding the results of the current manuscript and other such experiments in fixed tissue.

2.7 Conclusion

The Generalized Lorentzian Approach well-describes the MR frequency shifts in white matter. Freshly harvested nerve and fixed nerve show quite different results for the longitudinal component of susceptibility, which suggest that care should be taken when analyzing phase data in fixed tissue and projecting findings to *in vivo* or freshly excised tissues.

Chapter 3 Biophysical Mechanism behind MR Signal Phase – Exchange effect[2]

3.1 Introduction

Gradient recalled echo (GRE) MR phase images acquired at high magnetic field strength show remarkably enhanced contrast between gray matter (46) and white matter (WM) in human (3) and animal (43) brain. The contrast-to-noise ratio in MR phase images shows an almost 10-fold improvement over conventional MR magnitude images. Anatomic/functional structures that are not apparent on magnitude images can be visualized in phase images. Indeed, phase contrast has been explored for applications such as the study of multiple sclerosis (67) and Alzheimer's disease (68). While the remarkable contrast observed at high field with phase imaging is provocative, the biophysical origins of this contrast are poorly understood. For example, phase variations have been observed across different brain regions (3), in both healthy and diseased brains. To fully quantify the anatomic, functional, and physiological information contained within phase images, it is crucial to understand the biophysical underpinnings of the MR "phase image" signal formation.

---

[2] All contents in this chapter have been published in Luo J, He X, d'Avignon DA, Ackerman JJH, Yablonskiy DA. Protein-induced water 1H MR frequency shifts: Contributions from Magnetic Susceptibility and Exchange. J. Magn. Reson. 2010; 202:102-108.

The MRI signal phase is determined by frequency shifts caused by multiple effectors. One group of effects relates to magnetic susceptibility variations within the tissue. Such tissue components as lipids (3), non-heme iron (3,69-71), deoxyhemoglobin in the blood (3,49,72), and proteins (53,73) were suggested as possible sources of susceptibility variation. Importantly, He and Yablonskiy (74) showed that the MR signal frequency shift depends not only on tissue chemical composition but also on tissue architecture at the cellular and subcellular levels (i.e., geometrical distribution of cells and structures within the cells). They proposed a new theoretical concept for evaluation of the frequency shifts that lead to tissue phase contrast between GM/WM/CSF. Their theory provides a means to predict tissue frequency shifts from the known tissue architecture and magnetic susceptibilities of proteins, lipids, tissue iron and deoxyhemoglobin in the blood. The derived shifts agree very well with the experimental results of Duyn *et al.* (3). Importantly, the work by He and Yablonskiy successfully explained the lack of phase contrast (3) between WM and CSF in the motor cortex area of the human brain.

However, another mechanism - the water-macromolecule exchange effect - has been suggested as an alternate or contributing cause of GM/WM phase image contrast (42). The association of water and hydrophilic groups on the surface of

macromolecules, including labile ^{1}H sites, and resultant exchange between “bound” and “free” water, is known to substantially contribute to the water ^{1}H T_1 and T_2 relaxation times due to the abundant macromolecular content *in vivo*, especially proteins (75-79). Although a water-macromolecule association/exchange mechanism cannot solely explain both the lack of contrast between CSF and WM (3) (protein contents are different - 10.9% in WM (24) and 0.015%~0.045% in CSF (80)) and the orientation dependence of phase contrast in white matter (43), it remains important to assess the roles of exchange vs. susceptibility in the formation of phase contrast.

Proteins constitute one of the major components of brain tissue (~50% of dry tissue weight). Thus, it is reasonable to hypothesize that proteins could play a dual role – modulating both magnetic susceptibility and water-macromolecule exchange - in shifting the water MR frequency. Understanding the extent to which these roles are in play is important to quantitative interpretation of the contrast in GRE phase MR images. Hence, the major goal of this manuscript is to separate and scale the contributions of protein-induced magnetic susceptibility and exchange effects to the observed shifts in MR signal frequency.

3.2 Materials and Methods

An aqueous solution of BSA (bovine serum albumin) was chosen as a model system to study the effects of protein content on the water ^{1}H MR signal frequency. 1,4-Dioxane ("Dioxane"), which has been reported to be an appropriate internal reference in protein solutions (81), was employed as an internal ^{1}H MR frequency reference.

3.2.1 Sample preparation

To prepare a stock protein solution, 10g BSA (99% purity, Sigma, [CAS No. 9048-46-8]) was dissolved in de-ionized water (with 0.5% v/v Dioxane) to a final volume 100ml. The solution was clear to the eye, indicating the lack of residual insoluble components. Additional BSA samples were prepared from this stock solution by dilution with de-ionized water (which also contained 0.5% v/v Dioxane) to concentrations of 25, 50, 75, 100 mg (BSA)/ml (solution). The BSA volume fraction of the stock solution was calculated by weighing the volumetric flask before and after making the solution; from the mass of the BSA powder and the mass of the total solution, the mass of de-ionized water was determined. Knowing the density of water at the relevant temperature, the water and BSA volume fractions were derived.

3.2.2 Mechanisms Affecting the ^{1}H Water MR Signal Frequency

The magnetic resonance frequency f of a spin immersed in a homogeneous media containing macromolecules can be described by several additive

components: (i) a component $f_0 = \gamma \cdot B_0$, the base Larmor resonance frequency, where γ is the gyromagnetic ratio and B_0 is the main static field, (cgs units are used throughout this paper), (82) a component Δf_χ due to the magnetic susceptibility of the media, (iii) a component Δf_e due to chemical exchange between free (bulk) water and bound water, typically that associated with hydrophilic groups on the surface (and perhaps interior) of macromolecules, and (83) a component $-\sigma f_0$ due to the local, electronic shielding provided by the "host" water molecule (shielding factor σ):

$$f = f_0 + \Delta f_\chi + \Delta f_e - \sigma \cdot f_0 \ . \qquad [3.1]$$

The frequency component Δf_χ due to magnetic susceptibility for a homogeneous, isotropic liquid (media) can be described as a sum of two terms. The first term arises from the presence of the media's external boundary:

$$\Delta f \ / \ f_0 = A \cdot \chi \ , \qquad [3.2]$$

where χ is the volume magnetic susceptibility of the media. Here for simplicity we only consider media whose boundary can be described by an arbitrary ellipsoidal shape. Hence, the magnetic field inside the boundary containing the media is homogeneous with the factor A depending on the specific shape of the media boundary (see the discussion in (62)). For example, if the media boundary forms an infinitely long cylinder, oriented with angle θ between the cylinder's main axis and B_0, $A = -2\pi \cdot \sin^2 \theta$, while for a spherical boundary $A = -\frac{4}{3}\pi$. The second term

describes the frequency shift caused by neighboring molecules, which in the Lorentzian sphere approximation can be represented as:

$$\Delta f \; / \; f_0 = \frac{4\pi}{3} \cdot \chi \; . \qquad [3.3]$$

The concept embodied in the Lorentzian sphere approximation has played an important role in the evaluation of magnetic susceptibility effects on the MR frequency shift Δf . It is based on the assumption that for a homogeneous, isotropic solution the microscopic local field acting on a spin can be evaluated as if this spin were moving inside a hollow sphere embedded in the magnetized media, while the media outside the Lorentz sphere can be modeled as a homogeneous and isotropic continuum. With these assumptions, the frequency shift Δf in the presence of external static field B_0 is described by Eq. [3.3]. It should be noted, however, that in biological tissues exhibiting anisotropic structure (i.e., white matter in the brain), the Lorentzian sphere approximation is no longer valid and a more general approach should be used (74).

3.2.3 Measurement of the Magnetic Susceptibility of BSA

A scheme employing orthogonal tubes was applied to measure the volume magnetic susceptibility of the BSA solutions (62). Standard, 5mm diameter, 7'' long, glass "NMR tubes" were filled with degassed BSA solutions and sealed with parafilm. A given tube was first oriented parallel to the magnetic field and then perpendicular to the field. Under these conditions, the MR signal frequency difference between the two orthogonal orientations will be determined only by the

susceptibility effects created by the boundary of the tube (coefficient *A* in Eq. [3.2]). Any other factors remain constant and, thus, are cancelled out.

During the experiment, since the tube is positioned in air instead of a vacuum, the frequency difference between the two orientations will be (the same for both water and Dioxane):

$$\Delta f = 2\pi \cdot (\chi_{solution} - \chi_{air}) \cdot \gamma \cdot \mathrm{B}_0 , \qquad [3.4]$$

where

$$\chi_{solution} = \chi_{water} + \zeta_{protein} \cdot (\chi_{protein} - \chi_{water}) + \zeta_{Dioxane} \cdot (\chi_{Dioxane} - \chi_{water}) \qquad [3.5]$$

and ζ indicates the relevant solution-component volume fraction. Thus, by measuring Δf at different volume fractions of BSA ($\zeta_{protein}$), the volume magnetic susceptibility difference between BSA and water ($\chi_{protein} - \chi_{water}$) can be determined. Further, since χ_{water} is a known parameter, the volume magnetic susceptibility of BSA can be determined.

Susceptibility measurement experiments were performed on a Varian DirectDrive™ MR scanner based on a 4.7T horizontal-bore superconducting magnet with a 21cm-bore inner-diameter gradient and shim assembly using a 1.5cm diameter, laboratory constructed, surface transmit/receive RF coil. A PRESS sequence was employed for localized shimming and data acquisition from a 4×4×4mm^3 voxel

selected at the mid point of the cylinder's axial length. Forty minutes prior to initiating experiments, a thermometer and all the tubes to be scanned were positioned at one end of the magnet for temperature stabilization. As noted above, each sample tube was first oriented parallel to the magnetic field B_0 and shimming was performed on the selected voxel. The ^{1}H resonance frequencies of water and Dioxane were measured. Then, immediately following data acquisition, the tube was carefully rotated about the voxel position so as to align it perpendicular to the magnetic field and the signal frequencies were determined again. For both orientations, the shim settings (currents in the shim coils) and the voxel positioning were kept the same. At each orientation, thirty individual (not summed) free induction decays were acquired with 4,000Hz bandwidth, 3s data sampling period, and 10s TR.

Frequencies for both water and Dioxane ^{1}H resonances were determined separately for each of the 30 individual spectra using Bayesian probability analysis (84). During the 5min total acquisition time, the water frequency drifted about 0.022ppm while the Dioxane frequency fluctuated around a mean ± SD of 7.1187 ± 0.0002ppm, indicating that field drift was minimal. The water frequency drift was presumably reflective of a ~ 2°K temperature decrease (~ -0.011ppm/°K) (85)). }) associated with relocating the sample to the observation coil. If any untoward field/frequency shift was detected during the experiment, e.g., if a light rail train passed by the scanner site (the scanner is ~ 150' feet distant from the train track),

the experiment was repeated. The ^{1}H resonance frequency of Dioxane (the mean of all 30 individually analyzed data sets) was used to determine the frequency differences between orthogonal orientations of the same sample contained in a given tube.

3.2.4 Separation of magnetic susceptibility and exchange effects

To separate susceptibility and exchange effects, a scheme employing coaxial tubes was employed. The inner tube (2mm outer diameter) was filled with aqueous solutions containing different concentrations of BSA, including 0.5% Dioxane; the outer tube (5mm outer diameter) was filled with water (no BSA) and 0.5% Dioxane. Accordingly, the magnetic susceptibility of the BSA solution in the inner tube was defined by Eq. [3.5], and the magnetic susceptibility of the reference solution (no BSA) in the outer tube is:

$$\chi_{ref} = (1-\zeta_{Dioxane}) \cdot \chi_{water} + \zeta_{Dioxane} \cdot \chi_{Dioxane} . \qquad [3.6]$$

Since the orientation factor *A* in Eq. [3.2] nulls when both coaxial compartments are parallel to the B_0 field, the ^{1}H MR signal frequency shift induced by the susceptibility difference between inner and outer tubes is:

$$\Delta f \ / \ f_0 = \frac{4\pi}{3} \cdot (\chi_{inner} - \chi_{outer}) = \frac{4\pi}{3} \cdot \zeta_{protein} \cdot (\chi_{protein} - \chi_{water}) \qquad [3.7]$$

Dioxane is not expected to undergo exchange or physically/chemically associate with BSA molecules. Thus, the frequency difference of Dioxane resonances

between inner and outer tubes is taken to reflect a pure susceptibility effect per Eq. [3.7]. However the water frequency difference between inner and outer tubes reflects both the protein induced susceptibility and exchange effects:

$$\Delta f_{water} / f_0 = \Delta f_e + \frac{4\pi}{3} \cdot (\chi_{inner} - \chi_{outer}) . \qquad [3.8]$$

Note that Δf_e is also proportional to the volume fraction of BSA. Therefore, by subtracting the frequency shift of Dioxane from the frequency shift of water, the net frequency shift due to water-BSA exchange can be quantified.

The coaxial tubes MR experiment was conducted on a Varian Inova 500MHz (11.74T) vertical bore high resolution spectrometer. The probe was equipped with a variable temperature controller and all samples were stabilized at a fixed temperature before and during the measurement. Data was acquired at two temperatures: 286.5°K (same as with the 4.7T imaging scanner) and 310°K (similar to body temperature). Samples did not contain D_2O, commonly used for field/frequency locking and shimming. A separate coaxial tube containing a D_2O/H_2O mixture was used for shimming. After shimming, thirty individual free induction decays were collected on each of the relevant coaxial samples, with 10,000Hz bandwidth, 2s acquisition time, and 10s TR. Radiation damping was eliminated by detuning the receiver coil and employing a reduced filling factor (5mm outer tube diameter in a RF coil greater than 10 mm in diameter).

Because data were acquired without a field/frequency lock, and there was not enough SNR for accurate evaluation of the Dioxane frequency in the inner tube from a single acquisition, the following procedure was used to correct for field drift. In each data set composed of 30 individual FIDs, the first FID acquired was used as a reference; the frequency shift caused by field drift was calculated by comparing the phase of the water signal in each of the 29 subsequent FIDs to the reference FID. The time domain data from each individual acquisition were then frequency shifted correspondingly and averaged (sum of 30 FIDs) after this correction. The frequencies of each resonance (water and Dioxane) in the coaxial tubes were determined from the summed FIDs for different protein concentrations using Bayesian probability analysis (84).

3.3 Results

Examples of water and Dioxane spectra obtained in an orthogonal tubes experiment and a coaxial tubes experiment are shown in Figure 3.1a and b. Double peaks for water and Dioxane can be observed for the coaxial tubes experiment. These peaks correspond to water and Dioxane in the outer (large amplitude signals) and inner tube (small amplitude signals) compartments.

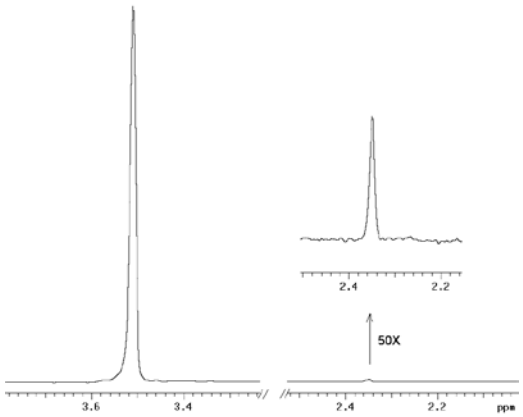

a)

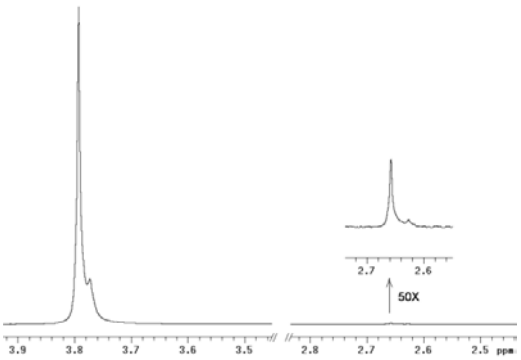

b)

Figure 3.1 Examples of spectra (line broadening apodization filter of 1Hz) obtained from the orthogonal tubes experiment. (a), and the coaxial tubes experiment after averaging (b). The Dioxane resonances are shown vertically expanded (50x) in the insets. Both experiments were carried out at the same temperature (286.5°K) and the protein solutions in both experiments contained 7.5% (v/v) BSA and 0.5% Dioxane. Resonance frequencies were determined by Bayesian probability analysis (84). Estimated uncertainties of resonance frequencies in (a) are: 1.3E-5 ppm for water and 2.5E-4ppm for Dioxane. Estimated uncertainties of resonance frequencies in (b) are: outer-tube water 1E-5ppm, inner-tube water 3.9E-5ppm, outer-tube Dioxane 9.7E-5ppm, inner-tube Dioxane 1E-3ppm.

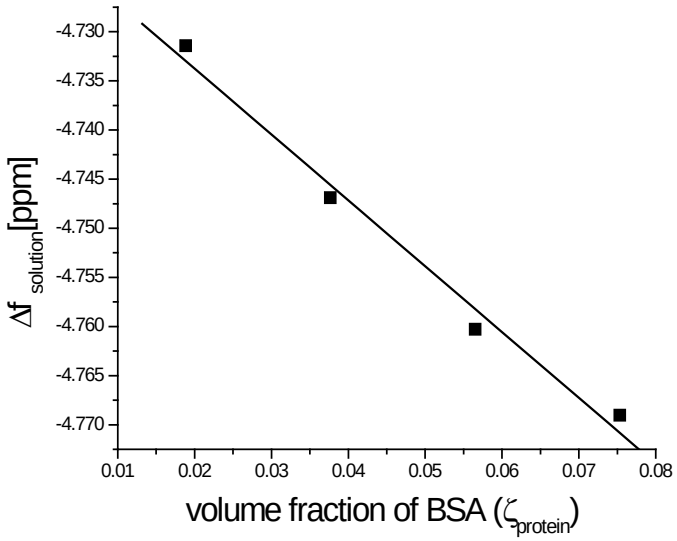

Figure 3.2 The dependence of magnetic susceptibility induced MR signal frequency shifts on protein volume fractions. $\Delta f_{solution}$ is the Dioxane MR signal frequency difference between cylindrical NMR tube orientations parallel and perpendicular to B_0 in the rotating tube experiment.

Figure 3.2 illustrates the observed frequency difference in the orthogonal tubes experiment at different protein concentrations. Fitting Eq. [3.4] to the $\Delta f_{solution}$ *vs.* volume fraction of BSA data yields (mean ± SD): $\chi_{protein} - \chi_{water}$ = (-0.107 ± 0.009) ppm and $\chi_{water} - \chi_{air} + \zeta_{Dioxane} \cdot (\chi_{Dioxane} - \chi_{water})$ = -(0.7513 ± 5E-4) ppm. Given the susceptibility of water (-0.719ppm (86)), the estimated volume magnetic susceptibility of BSA can be derived:

$$\chi_{BSA} = (-0.826 \pm 0.009)\text{ppm} . \qquad [3.9]$$

Further, given $\chi_{Dioxane}$ = -0.596 ppm (86), the magnetic susceptibility of air can be derived, χ_{air} = (0.0317 ± 5E-4) ppm. The positive magnetic susceptibility of air is caused by the presence of O_2, which is paramagnetic. This result is in excellent agreement with the susceptibility of oxygen in air as estimated from first principles using the Curie law, χ_{oxigen} = 0.0316 ppm, given the known molar magnetic susceptibility of pure O_2 ($\chi_m(O_2) = 3372\, ppm \cdot cm^3 \cdot mol^{-1}$ at 13°C (86)) and its volume fraction in air (21%). While this effect is small, it should be taken into account for accurate measurements of magnetic susceptibility.

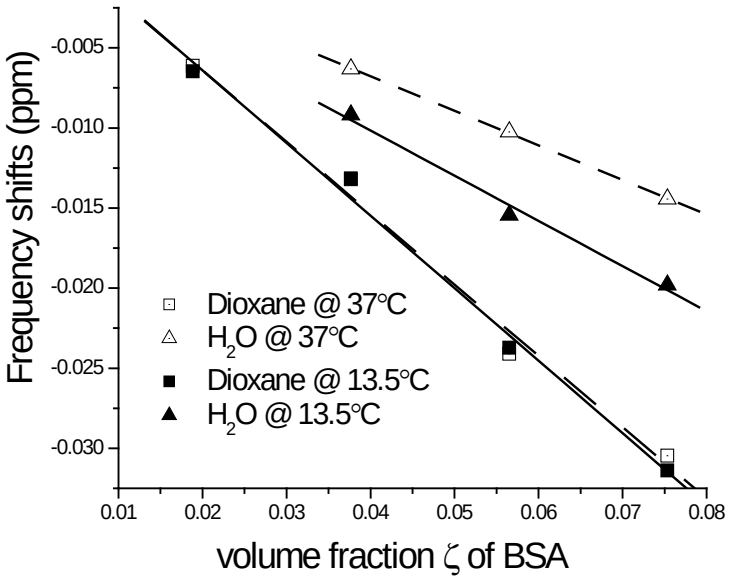

Figure 3.3 ^{1}H MR signal frequency difference of water (triangles) and Dioxane (squares) between inner and outer coaxial tubes $(f_{inner} - f_{outer})/f_0$ measured at 13.5°C (solid symbols) and 37°C (open symbols). Lines represent linear regressions. The slopes of the fitted lines are: (-0.45 ± 0.03) [ppm] for Dioxane, and (-0.28 ± 0.03) [ppm] for water at 13.5°C; (-0.445 ± 0.03) [ppm] for Dioxane and (-0.216 ± 0.004) [ppm] for water at 37°C.

Figure 3.3 shows the ^{1}H MR signal frequency difference between inner and outer tubes for water and Dioxane in the coaxial tubes experiment at two temperatures. Note that the ^{1}H frequency shift of water is the sum of the magnetic susceptibility effect and the water- exchange effect. Since Dioxane does not associate with BSA

(*vide infra*), the frequency shift of Dioxane can be attributed solely to a susceptibility effect:

$$\Delta f / f_0 |_{susceptibility} = \Delta f / f_0 |_{Dioxane} = -(0.45 \pm 0.03) \cdot \zeta \text{ ppm}. \quad [3.10]$$

As calibrated by Dioxane's pure susceptibility induced frequency shift, a BSA induced susceptibility effect will decrease the water ^{1}H resonance frequency. This is in agreement with our previous orthogonal tubes measurement.

Having quantified the magnetic susceptibility effect, the contribution of water-BSA exchange to the water MR signal frequency shift can be estimated by subtracting susceptibility frequency shifts from the observed water frequency shifts:

at 13.5°C: $\Delta f / f_0 |_{exchange} = \Delta f / f_0 |_{water} - \Delta f / f_0 |_{Susceptibility} = (0.17 \pm 0.03) \cdot \zeta \text{ ppm}$, [3.11]

at 37.0°C: $\Delta f / f_0 |_{exchange} = \Delta f / f_0 |_{water} - \Delta f / f_0 |_{Susceptibility} = (0.23 \pm 0.03) \cdot \zeta \text{ ppm}$. [3.12]

Hence, water exchange/association with BSA increases linearly with protein concentration as would be expected. It results in a frequency shift in opposite direction to that caused by protein susceptibility.

3.4 Discussion

The present work examines the homogenous model system of a native protein in solution. Two mechanisms through which proteins affect the water ^{1}H MR signal frequency are considered: magnetic susceptibility and water-protein exchange/association. The magnetic susceptibility of a substance is related to the electronic structure of its atoms. Protein density (g/ml) is greater than that of water. The presence of proteins in aqueous solution increases the density of circulating electrons (within molecular orbitals), thus making the solution more diamagnetic. (Recall, diamagnetism is related to changes in the molecular electron currents induced by the magnetic field.) According to Eq. [3.10] this decreases the water ^{1}H MR signal frequency. Water-protein exchange can be envisaged as a rapidly time modulated interaction/association between water and multiple exchangeable sites on protein residues (primarily –NH-, -NH_2, -OH, -SH and –COOH). The overall effect is a shift of the water ^{1}H MR signal to higher frequencies. On a protein volume fraction basis, the susceptibility effect is twice that of, and in opposition to, the exchange effect. As shown in Figure 3.3, the susceptibility induced frequency shift is not affected by temperature (as expected because small temperature variations have little effect on molecular electronic structure), while the exchange induced frequency shift is affected by temperature. This is also expected because temperature influences the rates of kinetic processes including protein conformational dynamics, which consequently alters exchange/association phenomena between water and protein (87).

As noted above, in native BSA solution at 37°C the amplitude of the exchange effect is one half and opposite in sign to that of the susceptibility effect. It is likely the water-protein exchange effect is even smaller in biological tissues where proteins are often cross-linked, associated with membranes or other proteins and sites for water association are reduced in number. Indeed, as a globular protein, BSA has a hydrophobic core and a hydrophilic surface, which makes it soluble in water. Its structure is representative for a large group of proteins: hemoglobulins, immunoglobulins, albumins, enzymes, etc. Considering brain *in vivo*, apart from the soluble proteins, the other major protein class is insoluble in water (88-90), namely, fibrous proteins (scleroproteins), which form neurofilaments and microtubules, etc. These proteins are found as aggregates due to hydrophobic groups that stick out of the molecules, providing mechanical strength and rigidity for the tissue as well as for physiological functions. Due to their aggregated structural features, protons on the surface of fibrous proteins are more likely to have very short ^{1}H T_2 relaxation time constants, further resulting in a reduction of water frequency shifts due to exchange effects. Hence, comparing with the model native protein solution employed herein, it is likely exchange effects *in vivo* will contribute even less to the water MR signal frequency shift. At the same time, protein contribution *in vivo* to tissue magnetic susceptibility will remain the same as measured herein. (The reader is reminded that the contribution of highly anisotropically organized protein structures to the water ^{1}H MR signal frequency shift cannot be described in terms of

the Lorentzian sphere approximation, Eq. [3.3], a more general approach must be applied (74).)

This method employed herein for separating magnetic susceptibility and exchange effects relies on having a reliable internal reference, Dioxane, that does not interact/associate with BSA. Several lines of evidence support the choice of Dioxane for this purpose. First, the Dioxane ^{1}H MR signal in the compartment with BSA showed no line broadening, consistent with a lack of significant interaction/association between Dioxane and BSA. Second, measurements of Dioxane frequency shift *vs.* protein concentration at 13.5°C and 37°C (see Figure 3.3) showed no temperature dependence, again consistent with a lack of significant interaction/association between Dioxane and BSA (as was not the case for water, Figure 3.3). Third, comparison of results obtained in the orthogonal tubes experiment with those from the coaxial tubes experiment further confirms that Dioxane exhibits no (or negligible) interaction/association with BSA. Indeed, we have determined from the orthogonal tubes experiment that the magnetic susceptibility of BSA is $\chi_{BSA} = (-0.826 \pm 0.009)\text{ppm}$, see Eq. [3.9]. Substituting this value into Eq. [3.7] we can predict that the frequency shift of the Dioxane MR signal between inner and outer compartments in the coaxial tubes experiment should be $(\Delta f / f_0)_{Dioxane} = -(0.45 \pm 0.04) \cdot \zeta \text{ ppm}$. This follows only if the frequency shift of the Dioxane signal is solely due to the magnetic susceptibility effect. Direct measurement as described in Eq. [3.10] is in an excellent agreement with this

prediction. That is, the frequency shift of Dioxane between inner and outer tubes is not affected by exchange/association with BSA, and reflects a pure susceptibility effect.

Although some studies suggest that Dioxane and water could affect each other's frequencies by 'bifunctional hydrogen bonds' (91), the absolute frequencies of Dioxane and water are not important in these measurement. Further, the same Dioxane concentration is maintained in both inner and outer coaxial tubes, thus the frequency difference between the two coaxial tubes is due solely to protein content.

These quantitative results regarding volume susceptibility are reported with respect to the volume fraction of BSA, which was calculated based on directly weighing protein powder and the measurement of solution volume. The estimated protein density in our solution was 1.332 g/cc, which is lower than the density of fully "dry" serum albumin reported as 1.381 g/cc (92). It is known, however, that crystalline protein is likely to contain approximately 10% (w/w) of water (83). Hence, from the density difference we can estimate that the water content in our purchased BSA is 10.6% (w/w) – similar to previously reported. Accordingly, we can recalculated the volume susceptibility of "pure" BSA as $\chi(pure\ BSA) = -0.841 ppm$ and the gram susceptibility as

$$\chi_g(pure\ BSA) = -0.609\, ppm[ml/g], \qquad [3.13]$$

which is in good agreement with previously reported "common χ_g value" of proteins: -(0.587 ± 0.005)*10^{-6}ml/g (93). Using the corrected value, we can re-examine the contribution of "pure" proteins to the water MR signal frequency shift at 37°C:

$$\begin{aligned} \Delta f / f_0\big|_{susceptibility} &= -0.51 \cdot \zeta_{pure}\ \text{ppm} \\ \Delta f / f_0\big|_{exchange} &= 0.26 \cdot \zeta_{pure}\ \text{ppm} \end{aligned} \qquad [3.14]$$

The possible role of water-protein exchange effects in the formation of ^{1}H water MR signal frequency shifts was first addressed by Zhong *et al.* (42). Data presented herein are different from their results, which utilized TSP as an internal reference. While TSP is broadly used in high resolution ^{1}H NMR experiments, our experimental data (see Appendix) suggests that TSP exhibits significant interaction with BSA. The line width of TSP in the coaxial tube with BSA is largely broadened compared to the line width of TSP in the coaxial tube without BSA. The frequency shift of TSP between the two coaxial tubes per unit volume BSA (-1.03 ± 0.07ppm) does not match the susceptibility effect determined by our orthogonal tube experiment (-0.45 ± 0.04 ppm), indicating the TSP frequency shift results from more than just the susceptibility effect of BSA. It is well known that an important function of serum albumin is to bind long-chain fatty acids and other like molecules, serving as a major transporter for free fatty acids *via* the plasma (94,95). Although the TSP is only equivalent to a 5-carbon chain, it is possible that BSA weakly binds with

TSP, resulting in a certain degree of exchange driven frequency shift. Earlier studies have reported that the chemical shift of TSP was dependent on the protein concentration ((81)).

3.5 Conclusion

In this study, the effects of protein content on water ^{1}H frequency shifts were examined. These shifts will contribute to the phase shift *in vivo* at high field. Two previously suggested mechanisms were determined separately and quantitatively by an experiment employing coaxial tubes and native protein (BSA) solutions. Results indicate that the protein susceptibility effect is twice that of, and in opposite direction to, the exchange effect. Excellent agreement between protein susceptibility measurement employing coaxial tubes and measurement employing an orthogonal tube protocol confirmed that Dioxane is a reliable marker for separation of magnetic susceptibility and exchange effects. This is further supported by a frequency shift, temperature dependence study. These experimental findings with native protein solution provide insights into the influence of protein content on water ^{1}H MR signal frequency. For structurally cross-linked proteins *in vivo*, the susceptibility effect is expected to play an even more substantial role in affecting the water ^{1}H MR frequency.

3.6 Line-broadening interaction between TSP and BSA

TSP (2,2,3,3-tetradeuterio-3-trimethylsilyl-propionate, 0.5% (w/w), 29mM) powder was added to the BSA stock solution and a control solution without BSA. The same experiment employing coaxial tubes as described in the main text was conducted to compare the TSP ^{1}H MR signal frequency change with that of Dioxane. However, the BSA solution was placed in the outer tube for improved detection (TSP has a broad line width in the presence of BSA).

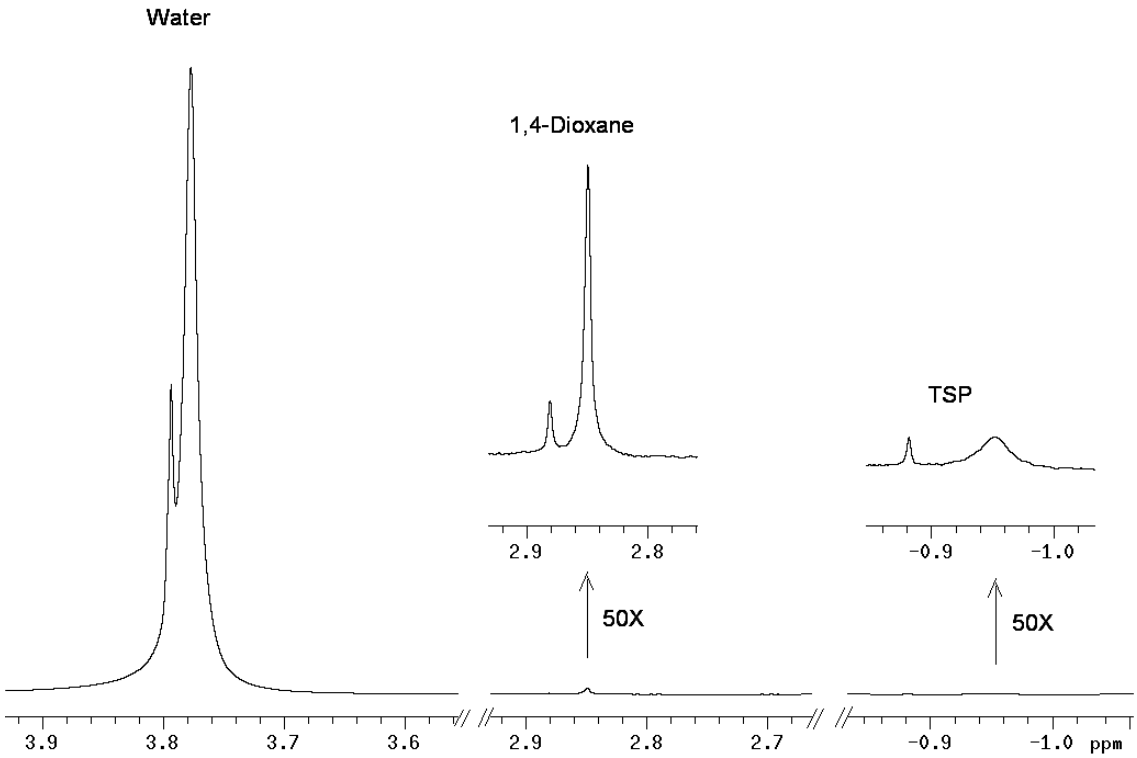

Figure 3.4 Spectrum (line-broadening apodization filter = 1Hz) from experiment

employing coaxial tubes. Concentric tubes were positioned parallel to the B_0 field, with temperature stabilized at 37°C. The solution in the outer tube contained 7.5% (v/v) BSA, 0.5% Dioxane, and 0.5% (w/w) TSP; the solution in the inner tube contained 0.5% Dioxane and 0.5% (w/w) TSP. Dioxane and TSP resonances are vertically expanded (50x) in the insets.

Figure 3.4 demonstrates a significantly broadened TSP resonance in the presence of BSA. Line broadening is not observed for the Dioxane resonance. With regard to the frequency shifts at this particular protein concentration: TSP is shifted by -0.072ppm whereas Dioxane is shifted by -0.031ppm. If TSP is taken as an internal reference and the BSA exchange effect on signal frequency is calculated, it would be +0.055ppm instead of +0.015ppm (using Dioxane as reference), a substantial systematic error.

Chapter 4 Gradient Echo Plural Contrast Imaging (GEPCI) – Basic and Derived Contrasts[3]

4.1 Signal Model and Data Processing of GEPCI

4.1.1 Multi-channel data processing

Multi-channel data were combined using a generalization of previously developed algorithm (82) that allows for the optimal estimation of quantitative parameters, such as MR signal decay rate constants. In original implementation it was assumed that the data from different channels are already phased coherently. Applying this algorithm for multi-gradient echo signal obtained from an M-channel RF coil, we get the following result:

$$S_{comb}(TE_n) = \frac{1}{M}\sum_{m=1}^{M}\lambda_m S_m(TE_1) S_m(TE_n) \qquad [4.1]$$

where index n enumerates gradient echoes, index m enumerates RF channels, $S_{comb}(TE_n)$ is a combined signal corresponding to the gradient echo time TE_n, $S_m(TE_n)$ are signals from individual channels, and parameter λ_m is

$$\lambda_m = \frac{\frac{1}{M}\sum_{m'=1}^{M}\sigma_{m'}^2}{\sigma_m^2} \qquad [4.2]$$

[3] Most contents in this chapter have been published in Luo J, Jagadeesan BD, Cross AH, Yablonskiy DA. Gradient Echo Plural Contrast Imaging – Signal model and derived contrasts. NeuroImage 2012; 60:1073-1082

Here σ_m are noise amplitudes (r.m.s.) in corresponding channels (*m*). They are calculated by averaging data from 10x10 pixel area in the corner of magnitude images $\left|S_m(TE_n)\right|$. Since noise levels of each acquisition (echo times) are similar, they are subsequently averaged to obtain σ_m for a single channel. The Rician nature of noise in magnitude images does not affect estimate of parameters λ_m since they are ratios of σ_m^2. The parameters λ_m provide additional signal weighting and reduce contribution of RF channels with high noise level.

Generalizing this consideration for complex data leads to the following algorithm for data combination:

$$S_{comb}(TE_n) = \frac{1}{M}\sum_{m=1}^{M} \lambda_m \overline{S}_m(TE_1) S_m(TE_n) \qquad [4.3]$$

where $\overline{S}_m(TE_1)$ is a complex conjugate of the signal from channel *m* at the first gradient echo time TE_1. Since signal phases of different channels differ by their initial values φ_{0m} but have the same frequency *f*, as described in

$$\varphi_m(TE_n) = \varphi_{0m} + 2\pi f \cdot TE_n \qquad [4.4]$$

this procedure removes destructive interference of data due to the term φ_{0m} from multiple channels. The procedure described by Eq. [4.3] is applied to each voxel in the image.

4.1.2 Phase Unwrapping and Multi-channel data

In order to generate GEPCI images, data from multi-channel RF coil should first be combined in a single data set. Figure 4.1 demonstrates the phase unwrapping and channel combination procedure proposed in this manuscript (see detail description in the Methods section). From phase maps shown in the top two rows of Figure 4.1, we can see that combining phase images from different channels requires solving two problems. First, individual receivers have different phase offsets, as described in Eq.[4.4]. To address this issue,for each voxel we multiplied signal from each channel by the complex conjugate of data from the first echo of the corresponding channel, thus eliminating the phase offsets of each receiver coil. Data from all channels were then averaged with their sensitivity weighting per Eq.[4.3] to achieve optimal SNR with minimum error in parameters estimate (82). Second problem is that phase images are affected by 'wraps', where jumps of 2π happen between adjacent voxels due to phase values of $2\pi m + \theta$ (m is integer) are encoded as identical. This problem becomes more pronounced at longer echo times. Usually phase unwrapping is accomplished in the image domain, where different algorithms have been used (see for example (96,97)). Here we take advantage of having gradient echoes corresponding to multiple TE and unwrap signal phase in the time domain for each imaging voxel. Frequency maps were then generated by fitting phase data for each voxel as function of the gradient echo times per Eq. [4.4]. Note that difference in wrapping pattern in the phase image corresponding to different TE does not affect this fitting procedure and resultant frequency maps. Though for

areas of the brain with strong field inhomogeneities additional unwrapping of the frequency map in the image domain might be required, this was not the case in any of our data.

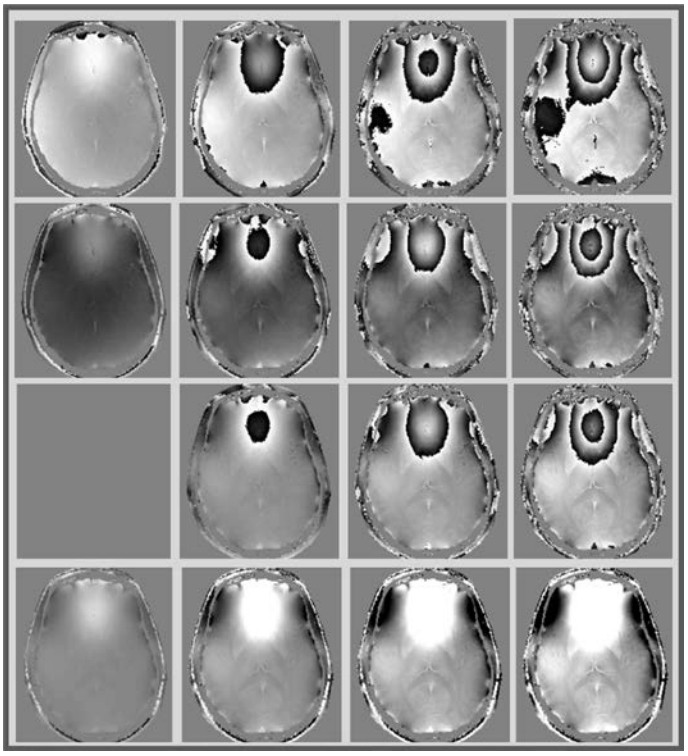

Figure 4.1 Example of the phase images before and after channel combination procedure. Top two rows show phase images at TE equals 4 ms, 12 ms, 20 ms, 28 ms from 2 different channels; Third row shows combined phase images obtained after channel combination according to Eq. [4.3]. First image in this row is zero because the phase of the first echo is compensated during channel combination. Bottom row shows phase images after unwrapping in the time domain as discussed in the methods section.

4.2 Experiment Protocol of Gradient Echo Plural Contrast Imaging

Brain images were collected from 5 healthy volunteers and one subject with Relapsing-Remitting MS who underwent brain MRI studies on a Siemens 3T Trio MRI scanner (Siemens, Erlangen, Germany). A 12-Channel phased-array head coil was used to obtain a 3D version of the multi gradient echo sequence with a resolution of 1x1x2 mm^3 or 1x1x3 mm^3, FOV of 256 mm x 192 mm and 11 gradient echoes (TR = 50 ms; minTE = 4 ms; delta-TE = 4 ms; bandwidth = 510Hz/Pixel; FA = 30°). Further effective resolution enhancement was achieved with zero-filling in k-space. Standard SWI images were also acquired with the same resolution and TR=27 ms, TE=20 ms, bandwidth 120Hz/Pixel, FA=15° for healthy volunteers; and standard FLAIR images were acquired for the MS patient with resolution 1.3x0.9x3 mm^3 by turbo spin echo sequence: TR=10 s, TI=2600 ms, TE=82 ms, turbo factor = 13, Echo trans per slice = 15. All studies were conducted with the approval of institution IRB.

4.2.1 Protocol Optimization

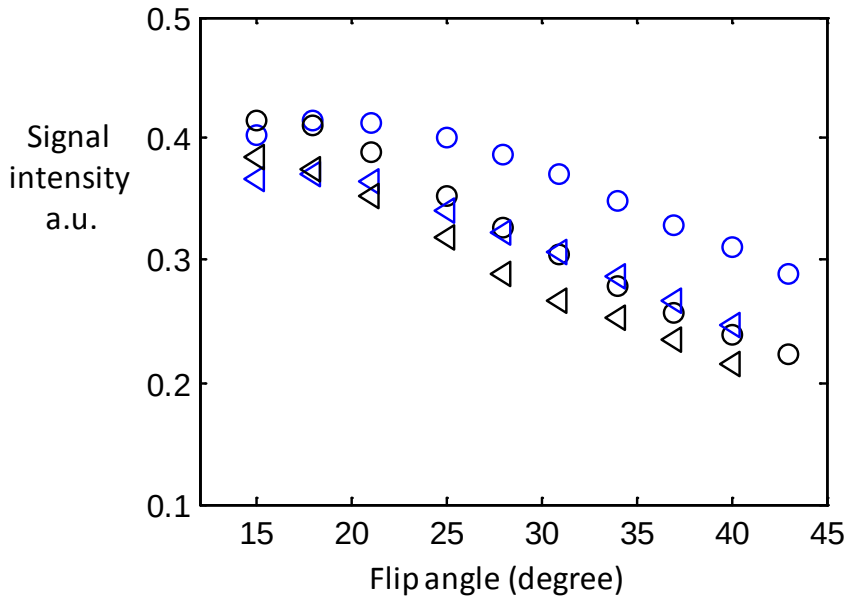

Figure 4.2 Comparison between signals result from TR = 40 ms (black) and TR = 50 ms (blue). Circles represent gray matter; triangles represent white matter.

Since in GRE it takes very long TR to get proton density weighting, in GEPCI, S_0 is targeted to be T1 weighted. We are trying to find an optimal combination of TR and flip angle for contrast between gray matter and white matter within reasonable time, and with sufficient SNR. From Figure 4.2, it is obvious that TR 50 ms gives both better signal and contrast than TR 40 ms. From Figure 4.3, we can get some phenomenological information on the GM/WM contrast. Black lines represent signal intensity of GM (from a single channel, before combining) and blue lines represent signal intensity of WM. A series of signals from 6 echoes are displayed. As we can see, the contrast between gray matter and white matter switches at around $\alpha = 18^o$, which is also when signal reaches maximum. As α increases, contrast between GM

and WM increases yet signal intensity decreases. Flip angle of 30^{o} was finally selected for the best contrast-to-noise ratio (CNR), with TR of 50 milliseconds.

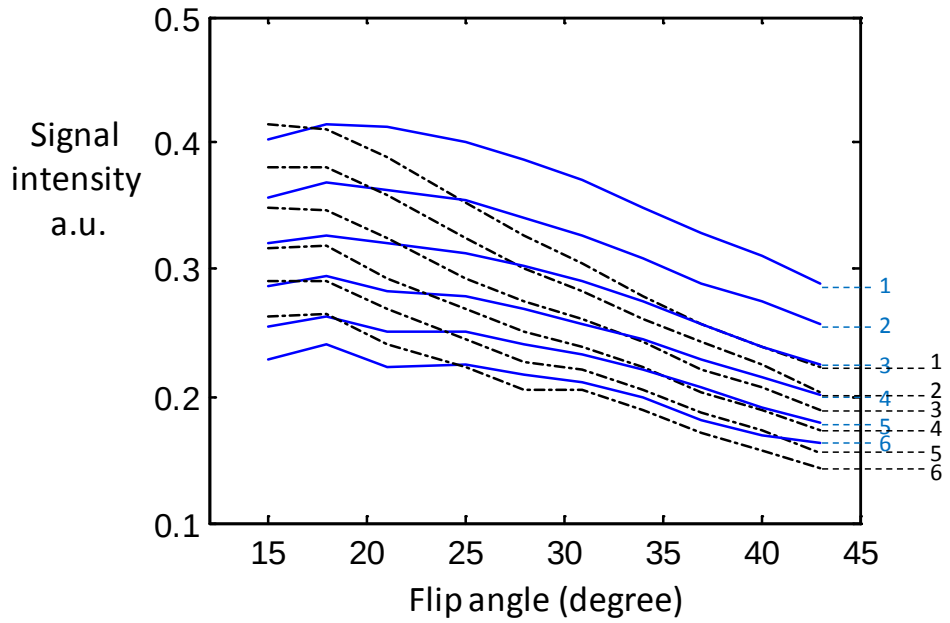

Figure 4.3 Signals in different echoes TR = 50 ms. Blue lines represent white matter; black dotted lines represent gray matter.

4.3 Basic Contrasts of GEPCI

4.3.1 Generating basic GEPCI images

Combined data are analyzed assuming mono-exponential signal decay and taking into account Eqs. [4.3] and [4.4]:

$$S_{comb}(TE_n) = S_0^2 \cdot e^{-R_2^*(TE_n+TE_1)} \cdot e^{i2\pi f(TE_n-TE_1)} \qquad [4.5]$$

Before fitting Eq. [4.5] to complex data (magnitude and phase images), the phase data were unwrapped for each voxel in a time domain using 11 data points (TE_n). If the frequency for some areas is high enough to cause multiple phase wraps within delta TE (that is 250Hz for our delta TE of 4 ms), then after time domain unwrapping there will be isolated areas in the frequency map that should be further unwrapped in spatial domain. Though most parts of the brain frequency map gets unwrapped already after the time domain procedure. The fitting procedure produces three naturally co-registered basic GEPCI images: a quantitative R2*=1/T2* map, a T1-weigted (S_0) image and a frequency (f) map. The frequency maps are then subsequently high-pass filtered to remove effects of macroscopic field inhomogeneities. Herein we use a 7x7 (out of 256x256) averaging matrix. Note that this filter is a rough approximation. Application of recently proposed advanced phase processing methods, e.g. SHARP method (98) or the projection onto dipole fields (99), could result in a more accurate removing of the artifacts related to macroscopic field inhomogeneities.

4.3.2 Basic GEPCI images

Example of basic GEPCI images is shown in Figure 4.4. The frequency map presents significantly different contrast from the corresponding magnitude image (T1w) or the R2* map. White matter (WM) showed up darker than the cortex and caudate, putamen in the deep grey matter area on frequency map; this contrast is reversed on T1w image; on the R2* map however, WM showed up darker than the

caudate and putamen, although still brighter than the cortex region. The nature of WM “darkness” on phase images was explained in (61) based on the introduced there Generalized Lorentzian approach. According to this theory, the longitudinal structures (myelin sheaths, axons, neurofilaments, etc.) that comprise WM do not contribute to the total frequency shift for the cylindrical axonal tracts even though WM has higher magnetic susceptibility than the GM. The frequency map allows superior delineation of the caudate, internal capsule, pallidum and putamen, whereas the differentiation is not as clear on T1 weighted image or R2* map. Grey matter/White matter boundaries are also clearly depicted on frequency maps. These results are similar to previously reported with high field MRI (3).

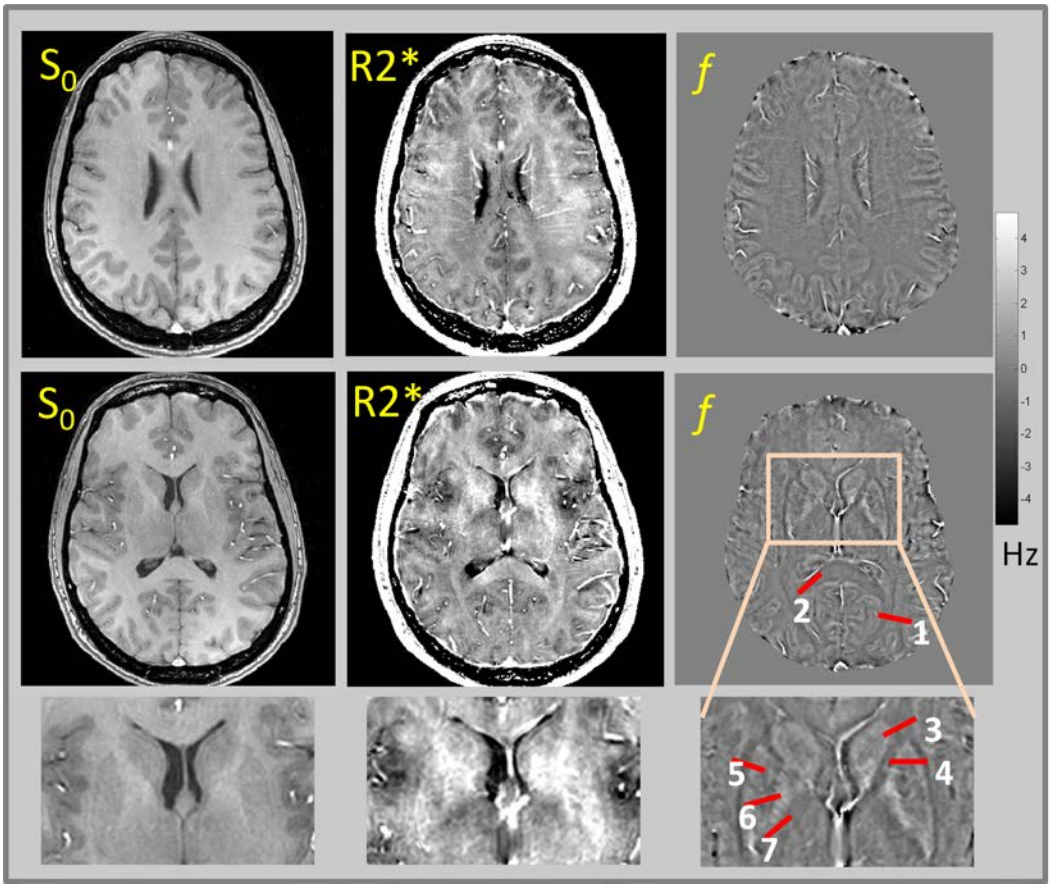

Figure 4.4 Example the basic contrast images generated by GEPCI technique from two axial brain slices (first and second rows). Lower row shows detail picture of the part of the images identified by a square. As described in Eq.[4.5], S0 is the T1w image, R2* map is derived from the magnitude of the signal decay, and the third image is a frequency map (*f*). The scale bar shows distribution of frequencies. Structures pointed out on the frequency map are: 1) Optic Radiations, 2) Splenium of Corpus Callosum, 3) Caudate, 4) Internal Capsule, 5) Putamen, 6) Pallidum, 7) Internal Capsule.

4.4 Derived Contrasts of GEPCI

4.4.1 Generating secondary derived GEPCI images

Several *derived* images can also be generated based on these basic GEPCI images. First, a positive Frequency contrast Mask (FM) is created by setting negative frequency values to unity, and normalizing positive frequency values to be ranged from 0 to 1, such that 1 corresponds to zero frequency and 0 corresponds to highest frequency. This procedure is similar to creating phase masks in standard SWI procedure (100).

4.4.1.1 SWI-like images are generated using the following equation

$$S_{SWI-like}(TE) = S_0 \cdot e^{-R2^* \cdot TE} \cdot FM^4 \qquad [4.6]$$

Here the T1 weighted image S_0 is T2* weighted with a certain TE (we used TE=20ms, which is typical echo time used for the SWI sequence on 3T systems) and is multiplied 4 times by the frequency mask (FM), which generates an image that mimics the standard SWI contrast (100).

4.4.1.2 GEPCI-SWI images are generated as follows

$$S_{GEPCI-SWI}(TE) = e^{-R2^* \cdot TE} \cdot FM^4 \qquad [4.7]$$

GEPCI-SWI images are free from T1 contrast contamination characteristic to the standard SWI because they are generated using pure T2* weighting and phase

contrast without S_0 term. Here we also use TE=20ms and multiply the magnitude image 4 times with a frequency mask just as in original SWI (100).

Minimum intensity projection (minIP) images using seven slices were also calculated for both the SWI-like and the GEPCI-SWI images.

4.4.1.3 GEPCI-T1f images

GEPCI-T1f images are derived by using only T1-weighted image (S0) and frequency contrast mask:

$$S_{GEPCI-T1F} = S_0 \cdot FM^4 \qquad [4.8]$$

In these images GM/WM contrast is enhanced.

4.4.1.4 Fluid Suppressed T2* images (FST2*)

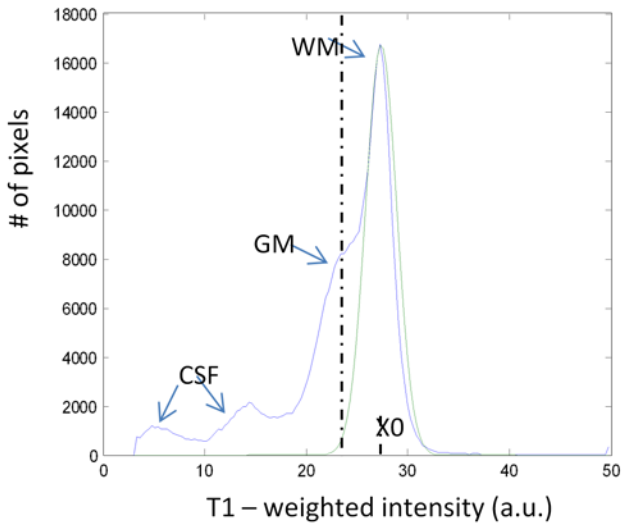

Figure 4.5 An example of the histogram of GEPCI T1w image. Different brain tissue components are indicated on the histogram： white matter (WM), grey matter (46), cerebrospinal fluid (CSF). X0 is the position of the WM peak. The vertical line indicates selected threshold that is used for CSF suppression in the FST2* images.

The goal here is to produce FST2* images that are T2* images with suppressed CSF signal that would “look similar” to FLAIR (fluid attenuated inversion recovery) T2 weighted images. Standard FLAIR-T2 images are obtained by using a long inversion pulse that suppresses the signal from CSF (long T1 component), and a long TE that produces heavy T2 weighting (101). To produce FST2* images we create a CSF mask (M_{CSF}) using the T1-weighted image (S0). The S0 image is first processed by FMRIB’s Automated Segmentation Tool (FAST) (102-104) to remove the bias in image intensity caused by RF field inhomogeneities. Example of the distribution of the corrected S0 values (T1w image) is plotted in a histogram, Figure 4.5; the signal intensities are ranked as S(WM)>S(46)>S(CSF), thus highest peak on the right corresponds to WM. Gaussian fitting was done on the right half of the main peak in this histogram determining peak position, X0, and standard deviation, STD. This allows thresholding of CSF signal. In this paper voxels that have S_0 values that are bigger than (X0 – 1.96 * STD) were considered as non-CSF area and their values were set as unity in M_{CSF} mask. Voxels with intensity below (X0 – 1.96 * STD) were normalized from 0 to 1, so that the darkest-appearing voxels on T1w image is 0, and brightest-apprearing voxels (those that are close to gray

matter) is 1. The FST2* images are produced by multiplying the T2* map with the CSF mask *n* times.

$$S_{FST2*} = T2* \cdot M_{CSF}^{n} \quad [4.9]$$

Since the voxels that are set to 1 in the mask will not get much attenuation in the resulting image, the threshold should be selected within the grey matter area to achieve a better suppression of CSF signal. In this manuscript we have compared several choices of parameter n (1~4). The optimal choice of threshold and 'n' is subject to further discussion. These images look like FLAIR images in the way that they have essentially T2* contrast (similar to T2 weighting) with strongly attenuated CSF signal.

4.4.1.5 T2*-SWI Images

In some applications like multiple sclerosis (MS) it might be advantageous to generate images that simultaneously show venous structure and T2 hyperintense lesions (105). Using GEPCI, this can be achieved by combining GEPCI-SWI and GEPCI FST2* images. Indeed, GEPCI-SWI data shows veins as dark contrast but are insensitive to hyperintense lesions. On the other hand, T2 hyperintense lesions are also hyperintense on FST2* images. We found that good visualization of the combined distribution of T2 hyperintense lesions and veins (and possible iron deposition) is achieved by multiplication of FST2* and GEPCI-SWI images so that T2 hyperintense lesions are contrasted by hypointense veins running through:

$$S_{FST2^*-SWI} = S_{FST2^*} \cdot S_{GEPCI-SWI} \quad [4.10]$$

It can also be applied to assess vascularity of tumors where tumors are bright on FST2*, and vascular structures inside tumors are dark.

4.4.2 Results of Derived Images

4.4.2.1 GEPCI-SWI and SWI-like Images

In this study, by combining basic GEPCI data sets in a manner analogous to standard SWI approach, we generated SWI like images and compared them to the Siemens scanner generated SWI data (Figure 4.6A and 4.6B). The images resulting from the standard SWI sequence were as usually contaminated by T1-weighting. This remains the case when GRE with several gradient echoes is used, although multi gradient echo approach allows increasing the signal to noise ratio (SNR) and contrast to noise ratio (CNR) of brain SWI images (106). The most obvious consequence of this T1 contamination is the 'dark CSF' area, particularly in the mIP images, which reduces contrast between the veins and CSF (Figure 4.6A and 4.6B). One way to resolve this issue was suggested by Haacke et al (107), that is to use small flip angles to minimize darkening of CSF area. Imaging parameter on 3.0T MRI scanner was proposed: FA 12-17 degrees, TR 25-35 ms, TE 20 ms, BW 80-100 Hz/pixel. As our images showed, although imaging parameters we used for the standard SWI imaging is within the recommended range, additional adjustments shall be made to get desirable SWI contrast. Further, using small flip

angle to minimize darkening of CSF area will inevitably result in loss of grey white contrast on the SWI images.

Using GEPCI approach allows overcoming this problem without losing signal. Indeed, GEPCI data were acquired with imaging parameters that maximize the T1-weighted contrast for S(108) as well as preserving SNR characteristic for optimal flip angle. In contrast to the SWI–like images and the standard scanner generated SWI images, GEPCI-SWI images had preserved bright CSF signal as well as preserved GM/WM contrast. This phenomenon maybe particularly useful in characterizing the deep veins in the area of the lateral ventricles. Such information about the deep veins is likely to be useful in surgical planning for patients who are set to undergo procedures such as placement of deep brain stimulators (109). Note that, the GEPCI-SWI image is as sharp as or even sharper than conventional SWI images with regard to vessel delineation. Also note that the GEPCI-SWI significantly enhances the gray and white matter interfaces, as seen in Figure 4.6A and 4.6B.

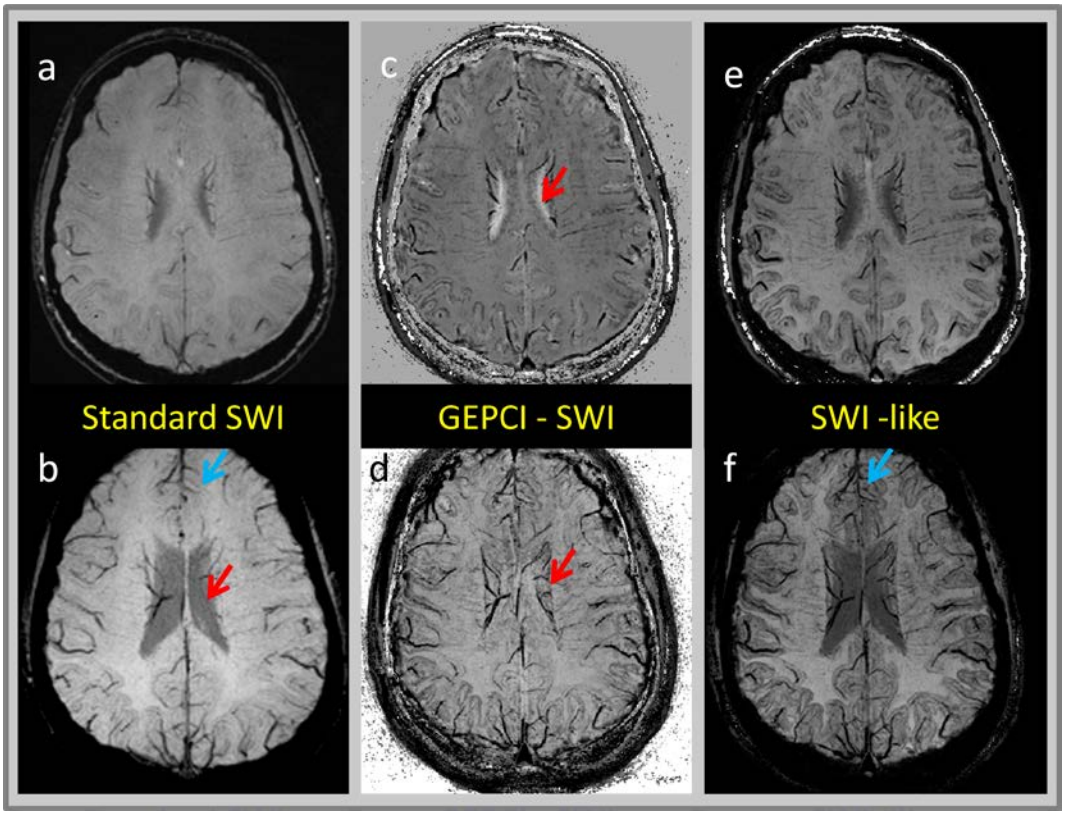

Figure 4.6A.

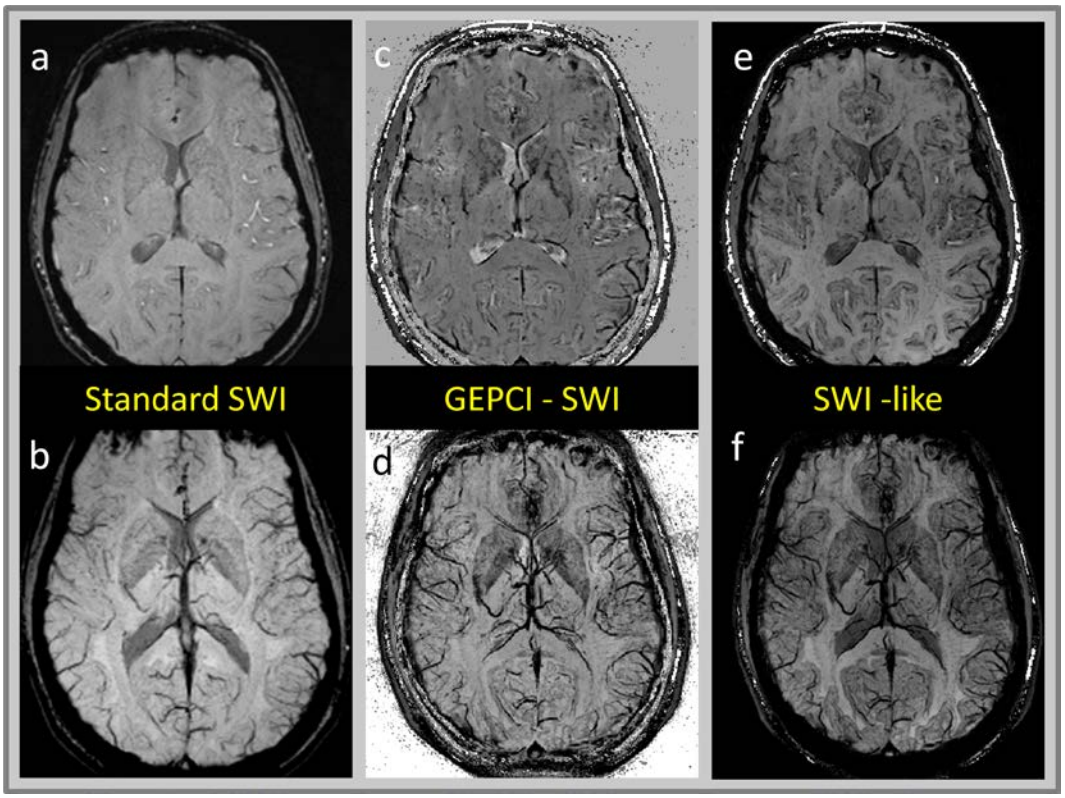

Figure 4.6B.

Figure 4.6A and 4.6B. Two examples of standard SWI images (left column - a,b), GEPCI-SWI images (middle column - c,d) and GEPCI-derived SWI like images (right column – e,f). The bottom row is the minIP corresponding to the images in the upper row. Standard SWI images (a & b) are obtained from Siemens automatic reconstruction. The rest of the images (c-f) are all derived from the same GEPCI 3D data set.

4.4.2.2 GEPCI-T1f Images

Another novel combination of the GEPCI basic images incorporates the frequency map and the T1-weighting (S0). The grey matter area on T1-weighted images is

darker than white matter. Considering the fact that grey matter tends to present more positive frequencies in frequency maps than white matter, plus the transition between gray and white matter on frequency map is more sharply delineated, we explored enhancement of GM/WM contrast by multiplication of the GEPCI T1w image with the frequency mask. The Resulting images (Figure 4.7) did indeed demonstrate more crisp GM/WM borders as well as enhanced GM/WM contrast compared to the T1w images. Deep grey matter structures such as caudate and putamen nuclei are also clearly outlined on the GEPCI-T1f images. These images are likely to be very useful in detecting malformations of cortical development in patients with intractable epilepsy, since they are more likely to be sensitive to blurring of the GM/WM interface from subtle cortical migrational abnormalities (110). Multiple sclerosis lesions in cortex, typically not clearly resolved by standard MRI (111), might be more clearly seen. Additionally, these images also offer a promising new method to achieve GM/WM segmentation which will result in more accurate volumetric data as well as improve data from cerebral perfusion studies.

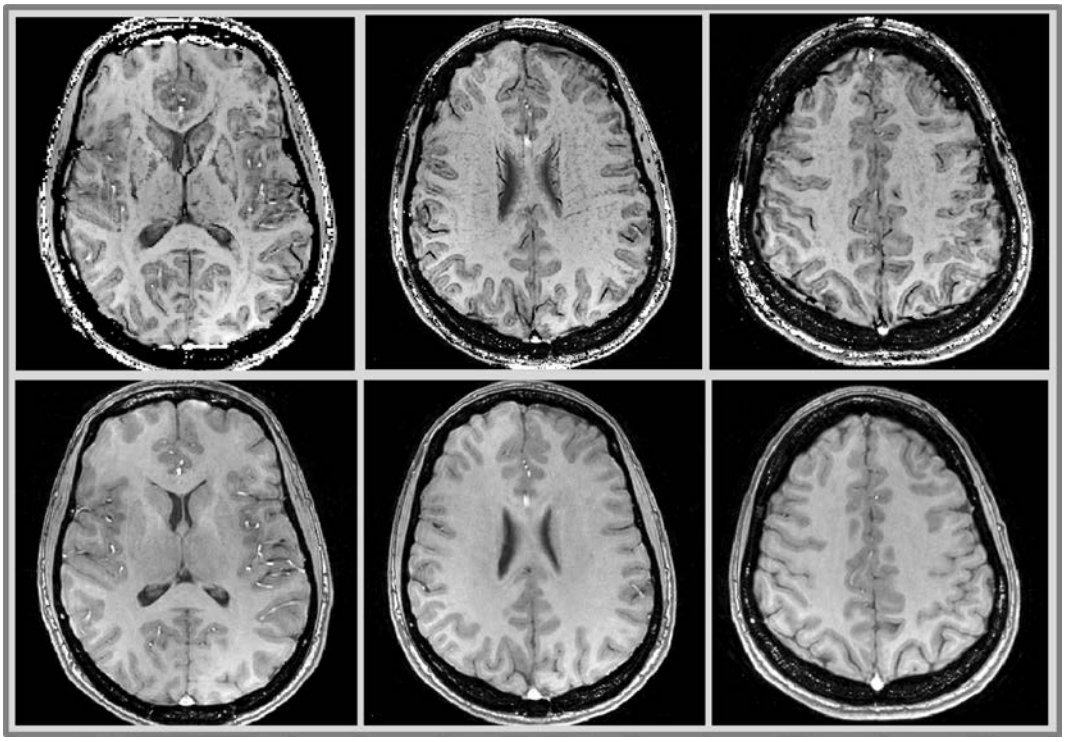

Figure 4.7 Examples of the GEPCI-T1f images obtained according to Eq. [4.8] (top row), comparing with basic GEPCI-T1 weighted images (bottom row). GEPCI-T1f images show excellent GM/WM matter contrast. Deep grey matter structure such as caudate and putamen nuclei are also clearly outlined on the GEPCI-T1f images.

4.4.2.3 FST2* Images

Example of GEPCI FST2* image is shown in Figure 4.8. These images are similar to FLAIR images in the way that CSF is suppressed based on tissue T1 properties. However, unlike T2 weighted FLAIR images which are based on T2 weighting, FST2* image is based on T2* map. Since difference between T2 and T2* values is usually small, especially in well shimmed white matter areas (112) FST2* images could be used to detect T2 sensitive changes in the brain, such as visualizing

edema, hyperintense lesions (in multiple sclerosis (40)), cerebral infarctions, which are usually well detected on the FLAIR sequences. Various degree of fluid suppression has been shown in Figure 4.8, as we go from n=1 to n=4. Choice may be made for different applications. For example, in MS brain part of the MS lesions can be suppressed together with CSF signal when bigger 'n' is applied. We could choose n=1 in order to maintain hyper-intensity of the lesions. Or since MS lesions are likely to appear in white matter areas, we could avoid suppression of lesions by designing WM masks based on GEPCI-T1w images. Additionally, based on its quantitative T2* nature, it could also be used to detect T2* sensitive changes, such as microbleeds or microcalcifications in the brain. Indeed, the fluid suppression based on the GEPCI-T1w image will not suppress artery signals on the T2* map, yet it should not affect most brain area.

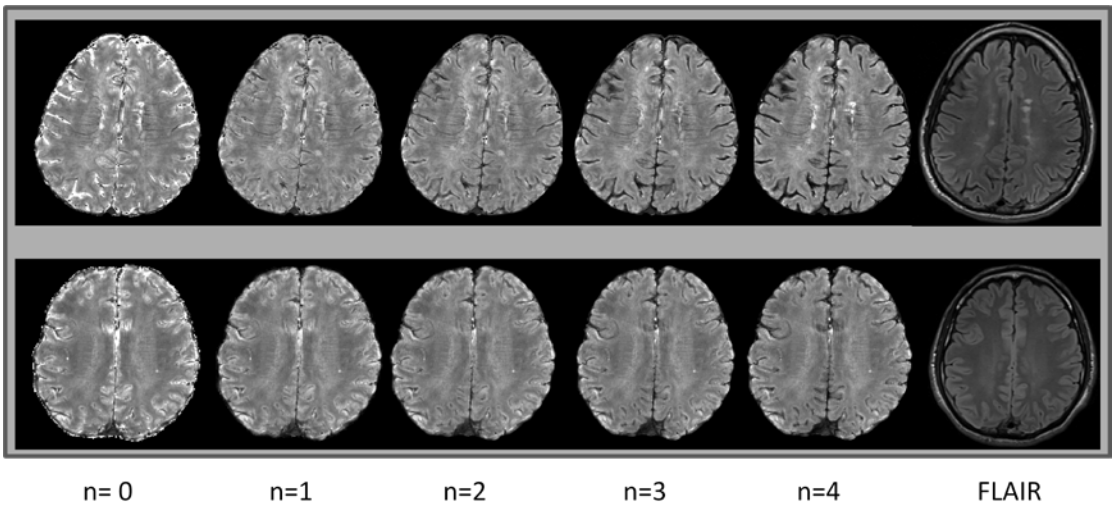

Figure 4.8 Example of the FST2* images (obtained using Eq. [4.9] with different parameter *n*), and corresponding FLAIR T2 images. Top row – images from a subject with relapsing remitting MS, bottom row - images from a healthy subject.

Different degree of suppression is shown from first column through fifth column, as parameter n grows from 0 to 4 in Eq. [4.9]. The case with n=4 for the MS patient shows image resulted from applying suppression of n=4 with exclusion of white matter area.

4.4.3 Possible applications of GEPCI in Clinical Arena

4.4.3.1 GEPCI in MS

GEPCI technique could also be applied to monitoring patients with multiple sclerosis. Typical MRI protocol for detecting MS includes FLAIR (fluid-attenuated inversion recovery), T2-weighted spin-echo, and T1-weighted spin-echo (including with and without Gd-enhancement) (113,114). Phase imaging and susceptibility weighted imaging has also been proposed for identification of MS lesions (47,115). While typical MRI protocol aims at imaging the contrast due to variations in the tissue characteristic relaxation rates, which are likely to represent lesions that are the result of myelin and/or axonal loss, or inflammation, the SWI and phase imaging are able to visualize small veins within white matter, which might help resolve the timing of interactions between venous structures and MS lesions. With the whole set of GEPCI images, as shown in Figure 4.9, we can obtain information on both the MS lesions and white matter veins within a single acquisition.

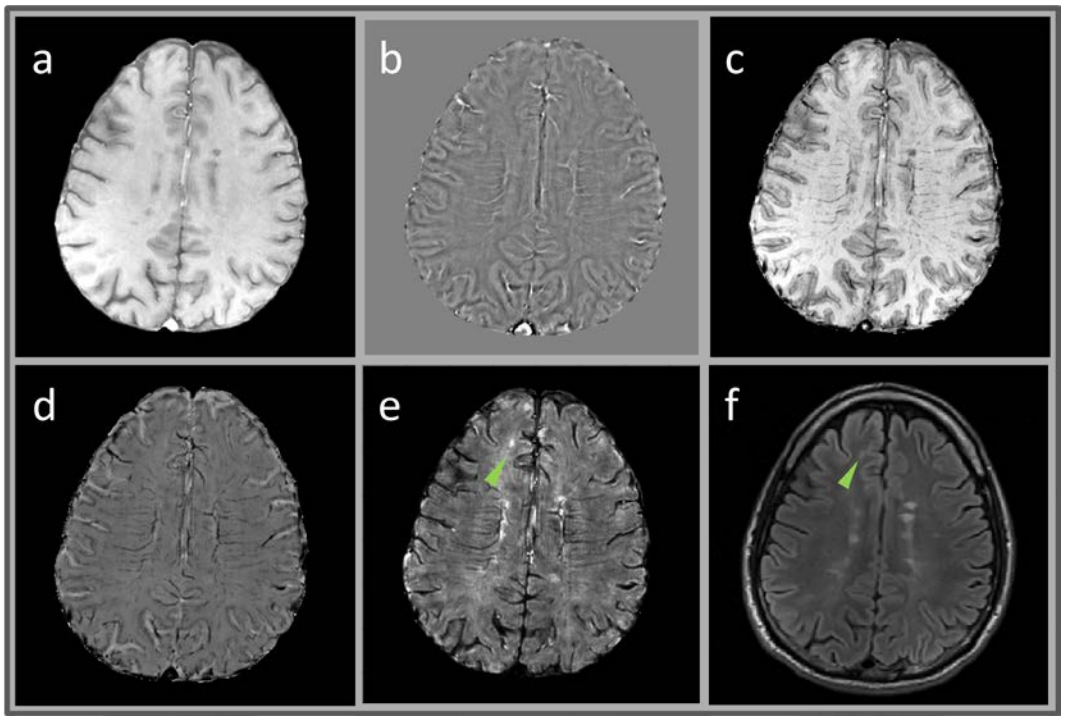

Figure 4.9 Examples of a series of GEPCI images applied to disease of Multiple Sclerosis. a) GEPCI-T1weighted image; b) frequency map; c) GEPCI-T1f image; d) GEPCI-SWI image; e) T2*-SWI, result from d multiplied by FST2* image; f) FLAIR image. Most MS lesions (hyperintence on e and f) are seen around veins; green arrow indicates example of lesion that is not affiliated with identifiable blood vessels.

MS lesions are identified as hypointense on GEPCI-T1w image (Figure 4.9a), and hyperintense on FST2* (Figure 4.8) due to increased T1 and T2* relaxation times. The T2* values in the lesion area could be further used for more quantitative assessment of MS lesions (40). GEPCI-SWI image (Figure 4.9d) shows veins without apparent indication of lesions. Lesions that are slightly hyperintense on frequency maps are darkened on T1f (Figure 4.9c) compared to T1weighted image

(Figure 4.9a). Veins also appeared on T1f image because of frequency map. Thus visualization of the distribution of lesions and their relation to veins (and possible iron deposition) is achieved by multiplication of FST2* and GEPCI-SWI images (Figure 4.8 with n=4 and Figure 4.9d), so that hyperintense lesions are contrasted by dark veins running through. This idea is similar to that recently proposed in (105) who combined FLAIR images acquired at 3.0 T and SWI acquired at 7.0 T. However, with GEPCI images, we easily achieve similar contrast from a single acquisition and complete, intrinsic co-registration. Comparing Figure 4.9e and Figure 4.9f, lesions that are hyperintense on standard FLAIR images are also clearly seen on the fusion of FST2* and SWI image where veins associated with MS lesions are readily observed. However, not all lesions in Figure 4.9 are associated with veins (e.g. green arrow on Figure 4.9e and 4.9f), and the underlying relationship between veins and pathology of MS remains to be investigated.

4.4.3.2 Other Possible Applications

The advantage of having a battery of images with multiple contrasts can have advantages for numerous clinical applications. For example, combining GEPCI-SWI and GEPCI-T1f images, can potentially be used to correct for venous contamination in dynamic susceptibility contrast MR perfusion maps such as obtained in stroke patients (116). In some patients, cavernous malformations can

be associated with epilepsy. With co-localized both SWI and T1f contrasts (venous and GM/WM delineation), it is possible to visualize the cavernous malformation and also evaluate its relationship to the adjacent cerebral cortex. This may provide new insights into the mechanism of epileptogensis in these patients and allow for better surgical planning (117,118). This combined contrast could also be useful in co-localizing subtle cortical malformations which may be found in the vicinity of complex venous abnormalities in some patients with epilepsy. The preservation of cortical GM/WM detail and representation of venous anatomy is also likely to be useful in surgical planning in patients with brain tumors who are set to undergo biopsies or curative resections (119,120). Based on these images, the surgeon will be better able to avoid prominent veins at the tumor margins as well as estimate the relationship of the tumor resection margins to eloquent areas of the cerebral cortex at the same time.

4.4.3.3 Potential Improvements

Although a number of novel contrast mechanisms have been highlighted in this manuscript, several limitations of the present study must also be mentioned. Most importantly, in this manuscript we have not discussed issues related to magnetic field inhomogeneities and their influence on quantitative results obtained with GEPCI technique, especially on quantitative evaluation of T2* relaxation time constant. Influences of field inhomogeneities are particularly significant around the

tissue/bone or tissue/air interfaces such as sinuses, ear canals, etc. However, away from these areas and for high resolution imaging as was used herein, this issue creates only minor problems in most parts of the brain. Detailed discussions of these issues can be found elsewhere (see for example (72,121,122)) and will also be addressed in our future publications. On the other hand, the non-local nature of frequency shift should also be noted when interpreting the derived contrasts based on application of the frequency masks. For example, the edge of the brain has some artifacts due to improper removal of the background field. Another example would be where there are sharp transitions in susceptibility of the brain tissue, e.g. the deep nuclei or ventricles. One might notice that the structures in frequency map are not always the same as that in magnitude images. In such cases tissue magnetic susceptibility will affect frequency map not only at the location of susceptibility variations but also in the surrounding areas. One of the ways to deal with this problem is already mentioned in the introduction quantitative susceptibility mapping (59,98,123-127).

Another potential area of improvement includes accounting for the multi-compartment tissue structure. Quantification of myelin-bound and free water fractions by a multiexponential analysis of the T2 decay has been discussed (128,129). Signal obtained based on a Carr-Purcell-Meiboom-Gill (CPMG) or Turbo Spin-Echo (TSE) sequence with multiple TEs was modeled by three pool model (130), or four pool model (131), or by non-negative least squares (132). Recently, it has been shown that T2* decay, which is measured by multi-echo gradient echo

sequence, could also be used for extraction of myelin water fraction (133,134). However these issues are beyond the scope of the current manuscript.

4.5 Summary

The GEPCI technique based on post processing of the multi-echo GRE data produces high quality frequency maps, high resolution R2* maps and T1-weighted images. These data sets can then be combined in novel ways to produce high resolution images which can offer excellent depiction of the intracranial venous system (SWI like and GEPCI-SWI images), images which promise to significantly improve the delineation of cerebral grey and white matter interfaces (GEPCI-T1f images) and GEPCI-FST2* images that look similar to FLAIR images. These novel imaging data sets can potentially find clinical applications in studying a variety of common neurological disorders. They can also find applications in basic neuro-anatomical and neuropathological research. Most importantly, these images with novel contrast properties can be obtained without any increase in acquisition time, and they are naturally co-registered obviating additional costs in terms of scanner time and personnel.

Chapter 5 Mapping T2* - Application of GEPCI to Monitoring Multiple Sclerosis

5.1 GEPCI images compared to Clinical Standard Spin Echo images

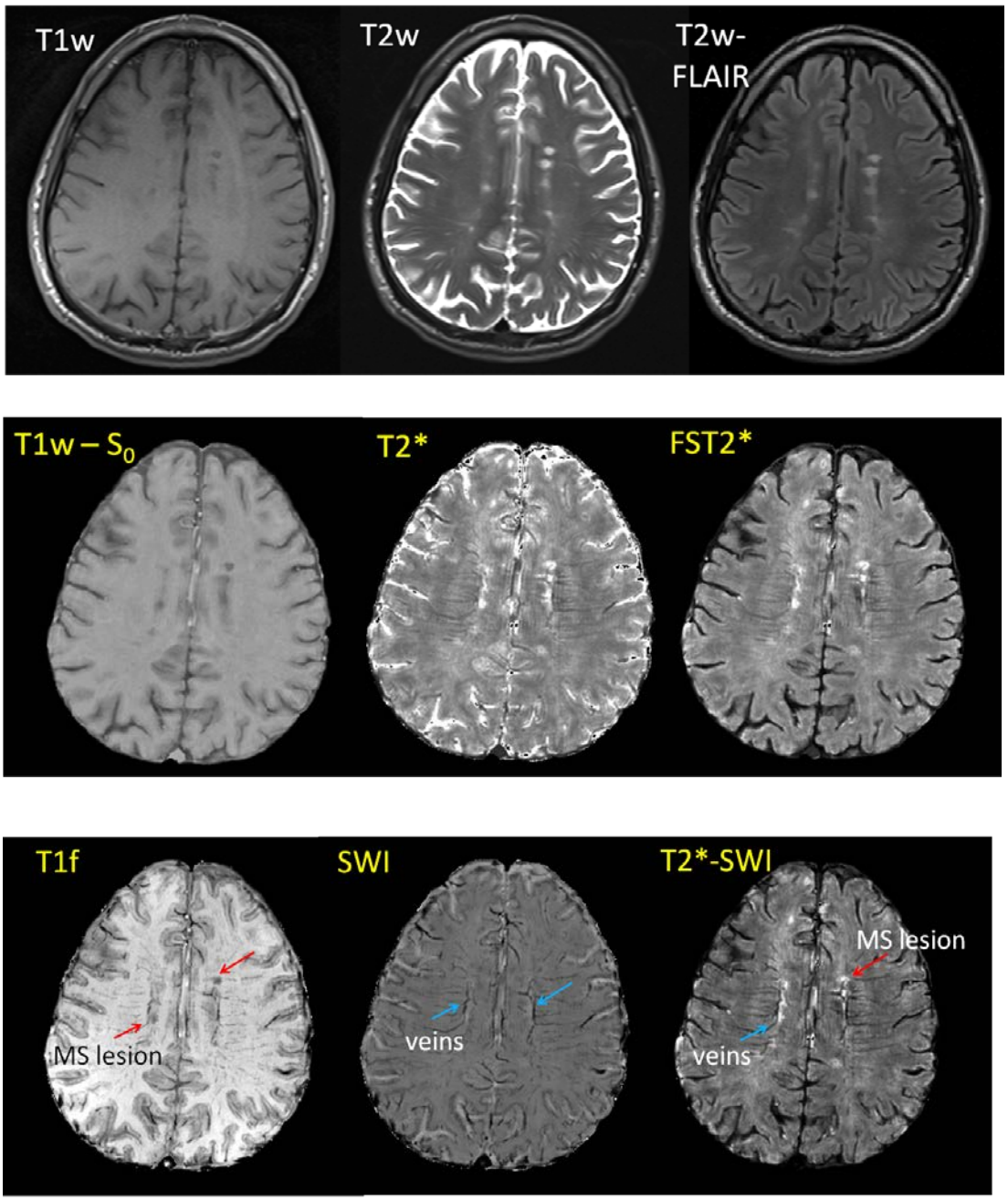

Figure 5.1 compares the images acquired by clinical standard sequences and GEPCI images of a patient with Relapsing-Remitting MS. Red arrows point to MS lesions; Blue arrows point to veins.

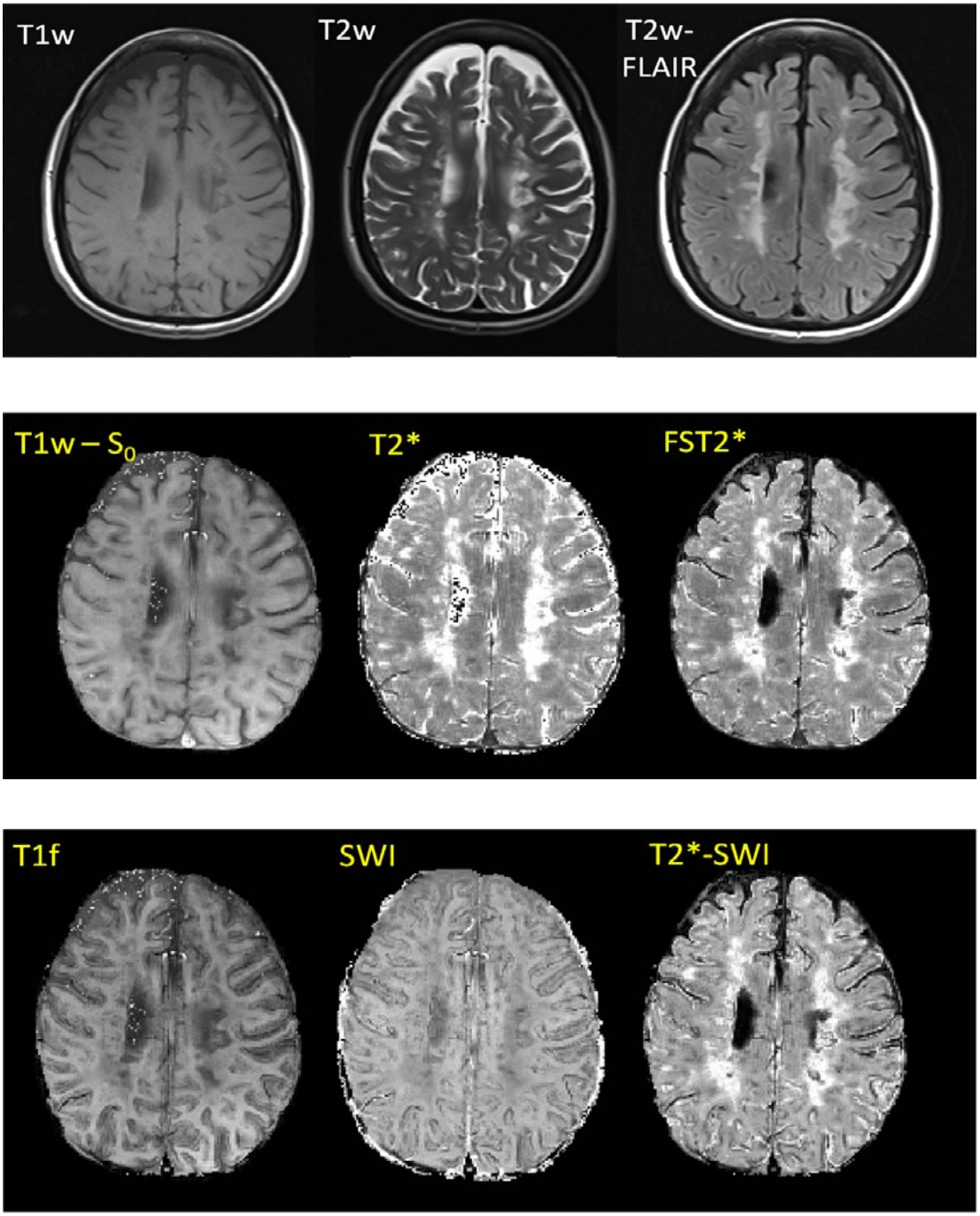

Figure 5.2 compares the images obtained by clinical standard sequences and GEPCI images of a patient with Secondary Progressive MS.

Clinical images: T1w (T1-weighted), T2w (T2-weighted), FLAIR (Fluid Attenuated Inversion Recovery). GEPCI images, as introduced in Chapter 4, are: T1w -S0 (GEPCI T1 weighted), T2* (GEPCI T2* map), FST2* (Fluid Suppressed T2* map), T1f (GEPCI T1 frequency image), SWI (GEPCI Susceptibility Weighted Image), T2*-SWI (GEPCI T2* map - SWI).

Tissue delineation is similar between the first panel (clinical images) and the second panel (GEPCI images) in Figure 5.1 and Figure 5.2. MS lesion contrast is well resolved with GEPCI (hypointense on T1w image and hyperintense on T2* map), thus allowing standard identification of MS lesions. All lesions that are seen on SE sequences (T1w, T2w, FLAIR) are also revealed by GEPCI.

Images shown above (Figure 5.1 and Figure 5.2) demonstrated several advantages of GEPCI over standard SE sequences for evaluation of MS. First, images obtained with GEPCI appear highly similar to standard scans; hence, they can be used in a reliable and conventional way for a clinical evaluation of the disease. Second, GEPCI-T1w images, GEPCI-T2* maps and FST2star maps are generated from a single dataset; that is, they are inherently coregistered. Third, the GEPCI technique

is based on gradient echo MRI and uses small flip angles as compared to spin-echo based techniques; hence it can be safely used in high-field MRI. Fourth, the acquisition time for simultaneous generation of these three images is considerably reduced compared with their equivalent SE sequences (6 min 40 sec) for GEPCI against a total of 15 min scan time for three scans in a standard clinical protocol. Fifth, GEPCI offers additional contrasts compared to SE sequences that might provide more insights to disease evaluation.

More importantly, the major advantage of GEPCI approach is its quantitative nature (T2* relaxometry) which can be used to quantitatively evaluate the severity of tissue damage in MS brain, based on the scoring method introduced in next section 5.2.

5.2 Quantification of Tissue Loss[4]

5.2.1 Tissue Damage Score (40)

To utilize the quantitative nature of GEPCI-T2* map, we introduce quantitative parameters to score the severity of the disease based on T2* (or R2*) changes in MS lesions.

[4] Most contents in this section have been published in Sati P, Cross AH, Luo J, Hildebolt CF, Yablonskiy DA. *In vivo* quantitative evaluation of brain tissue damage in multiple sclerosis using gradient echo plural contrast imaging technique. NeuroImage 2010; 51:1089-1097.

Each MS lesion voxel in GEPCI technique is characterized by an associated quantitative T2* relaxation time constant. We hypothesize that the R2* relaxation rate constant (R2*=1/T2*) will provide information on lesion severity. This hypothesis is a natural step because MS tissue damage involves loss of myelin lipids accompanied to a variable degree by loss of intracellular proteins, including axon proteins. In this process, R2* relaxation rate constant will progressively decrease from normal tissue values to values typical for interstitial fluid or CSF that is practically devoid of macromolecules. This supposition is in agreement with correlation established between tissue T1 and T2 values and tissue damage in MS reported in Schmierer et al. (2008) and Seewann et al. (2009). Recall, that R2*=R2+R2′, where R2=1/T2 and R2′ reflects contribution from mesoscopic field inhomogeneities generated mostly by the presence of blood vessel network in the brain tissue (122). Recent work has evaluated the tissue-specific R2′ relaxation rate in the healthy human brain (He and Yablonskiy, 2007). Using this data, we found R2′ value for white matter at 1.5 T to be equal to 0.35 s^{-1}, and at 3 T it is 0.7 s^{-1}, both are much smaller compared with the typical white matter R2 value that is approximately equal to 15–16 s^{-1} (Neema et al., 2009). The GEPCI technique, therefore, provides a quantitative measure of a tissue specific relaxation time T2* (equal to 1/R2*) that is very close to T2 measured using spin-echo sequences. Based on this consideration, we adopted the following procedure for estimation and scoring of tissue damage in MS.

First: design masks that contain only white matter, including both normal-appearing and lesioned areas. These masks are drawn manually on GEPCI-T1w images using home-built Matlab programs. All gray matter structures (cortical and deep) are excluded. Masks are applied on both GEPCI-T1w images and GEPCI-T2* maps. Then R2* histograms of the voxels inside masks of all slices are generated using a bin width of 0.3 s^{-1} ranging from 0 s^{-1} up to 30 s^{-1}. For control subjects these histograms look almost like ideal Gaussian distributions. For subjects with MS these histograms have a large peak with a quasi-Gaussian shape [corresponding to normal-appearing white matter (NAWM)] and a strongly elevated non-Gaussian tail on the left resulting from the presence of the MS lesions (see example in Figure 5.3). Second: define the level of tissue damage, or tissue damage score (TDS), for each voxel in MS lesions based on the tissue R2* value. The characteristics of the WM peak are determined using a standard Gaussian function that is fitted to the R2* distribution. To remove any influence on the fit from the tail existing in the R2* distribution of MS patients, we fit only the upper half of the R2* histogram. We define the “normal reference” R2* value as corresponding to the center of the NAWM peak (R2*c) obtained from the fitting procedure. As we already mentioned, in MS, tissue damage occurs through the loss of macromolecules, mainly myelin and proteins in axons, leading to reduction in tissue R2*. Hence, for each voxel in MS lesion with a given R2* value, the tissue damage score (TDS) is determined as:

$$TDS = \frac{R2_c^* - R2^*}{R2_c^*} \quad [5.1]$$

In addition to defining TDS for each voxel, we can also define the tissue damage load (TDL) for a given patient. This is done by summing TDS over all the voxels in MS lesions:

$$TDL = V \cdot \sum_N TDS \quad [5.2]$$

where N represents the total number of voxels in the MS lesions in cerebral white matter. We have also multiplied the sum by the voxel volume V (mm^3) to make this definition independent of the voxel resolution of the MRI pulse sequence. The tissue damage load, thus, assesses both the lesion load and the degree of severity of the MS lesions. Additionally, a mean tissue damage score (MTDS) can also be obtained by averaging TDS over all the lesions:

$$MTDS = TDL / LL \quad [5.3]$$

This mean score provides an estimate of the average severity of abnormal white matter tissue in the subject's brain.

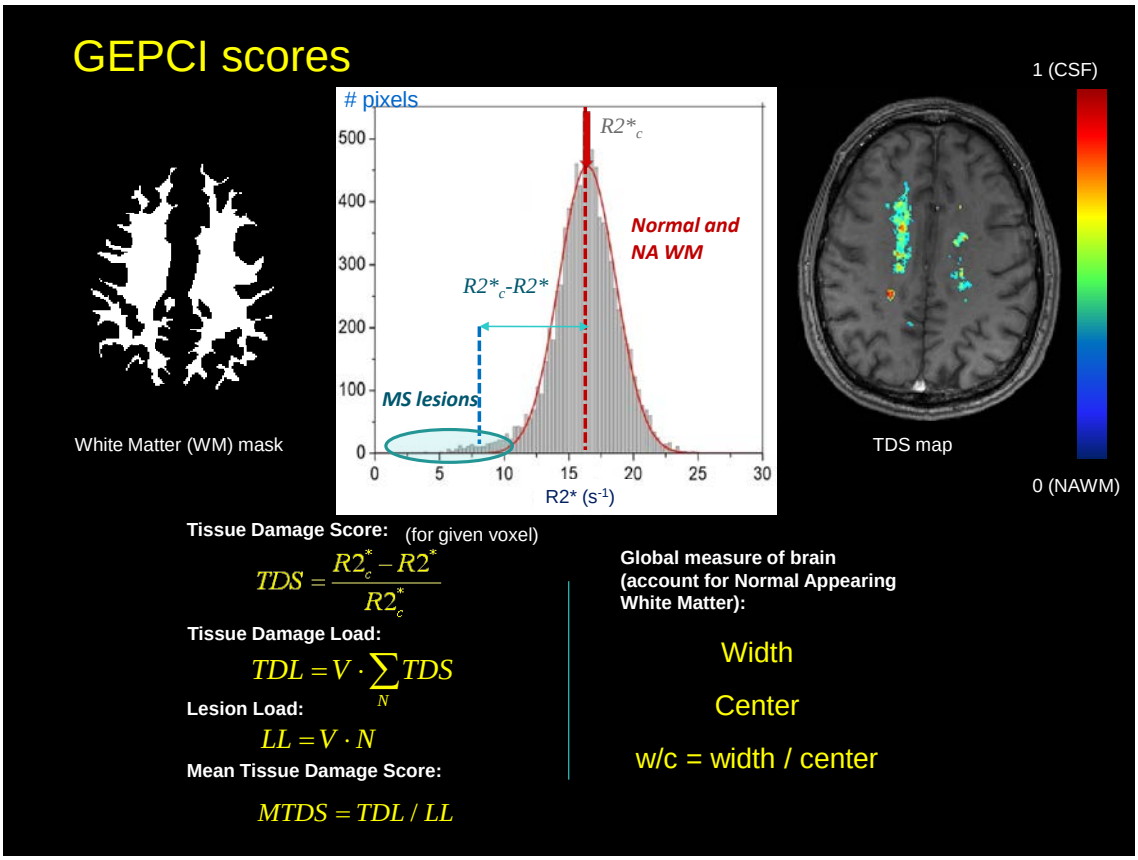

Figure 5.3 Introduction of GEPCI scores.

To apply Eqs. [5.1] and [5.2], we need to define a method for separating “normal” brain tissue from MS lesions. This procedure is always ambiguous because lesions almost never have sharp boundaries. Also, the distribution function of R2* values of normal WM has a Gaussian type shape. As for any Gaussian distribution, 95% of R2* values are located around peak center in the interval R2*=R2c*± 1.96σ, and 99% of values are in the interval R2*=R2c*±2.58σ, where σ is the distribution width. This means that even in the normal brain there are voxels that have “abnormal” GEPCI scores. Hence separation of tissue into “normal” and “abnormal” is always somewhat subjective. Visual examination by a neurologist (A.H.C.) of GEPCI and

standard clinical images from subjects with MS suggested that the threshold of 1.96σ separates most of the MS lesions from normal appearing tissue. We will use this threshold in this pilot study leaving more detailed examination for future work. In addition, all the voxels that have R2* below selected threshold and are isolated (single voxels) or have only one neighbor (hanging voxels) are eliminated from consideration to reduce influence of noise on our quantitative estimates. Moreover the characteristics of the main part of R2* distribution could also reveal info on MS disease (ref NAWM, peak shift). So we also take width, center, and w/c as part of GEPCI measures.

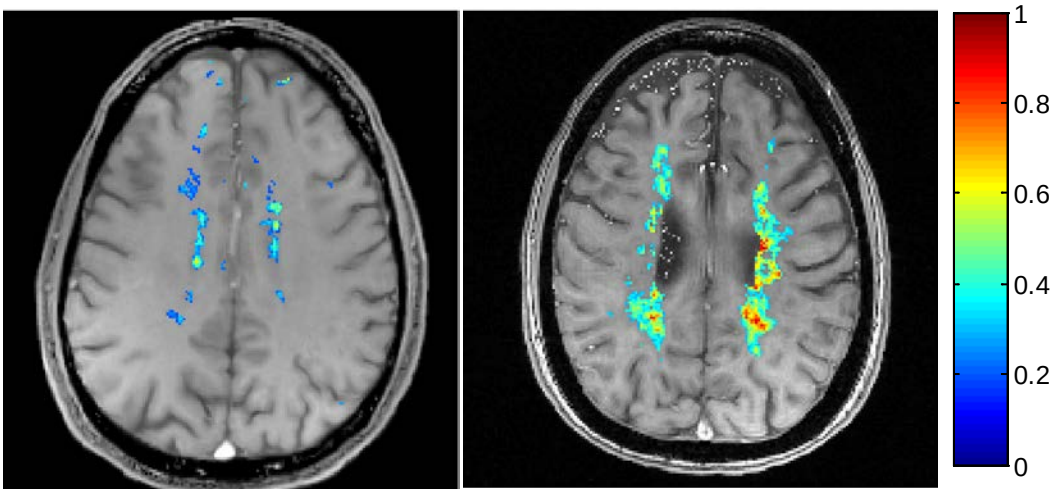

Figure 5.4 Illustration of GEPCI score maps obtained from subjects with RRMS and SPMS. They are made by overlapping colored TDS indices on T1 weighted images.

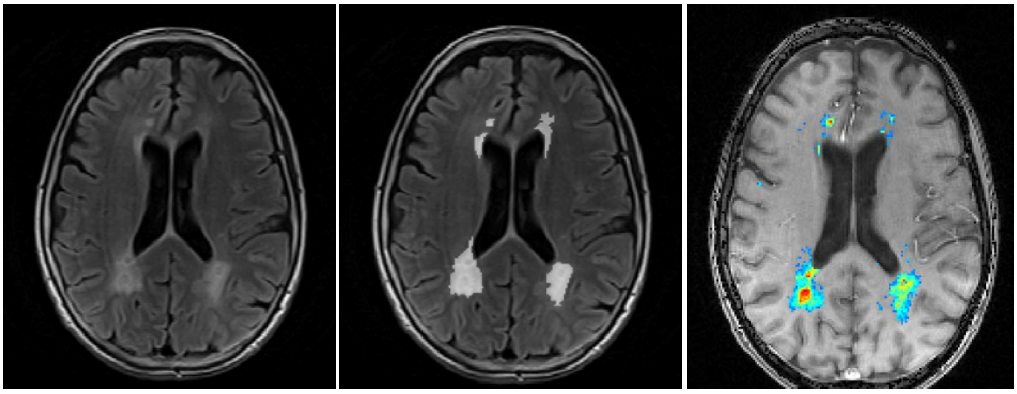

Figure 5.5 Illustration of lesion load determined by GEPCI compared to FLAIR image. Left: FLAIR image; Middle: FLAIR image with highlighted lesion area; Right: GEPCI score map.

5.2.2 Reproducibility of the R2 map*

Tissue-specific parameter, R2* (= 1/T2*) is not used as commonly as R2 or R1 in clinical studies, and is usually considered susceptible to field inhomogeneity. To ensure that TDS and other GEPCI scores are suitable for longitudinal studies, we tested the reproducibility of R2* measurement by GEPCI technique.

Experiments are performed on one healthy volunteer and one MS subject with the same protocol on 1.5 T scanner and 3.0 T scanner respectively. First run: standard GEPCI acquisition; second run: a consecutive scan immediately following first run; third run: subject was pulled out from scanner, tilted head while he was lying on the

table, sent back in the scanner, and then scanned with the same sequence after careful shimming of the field.

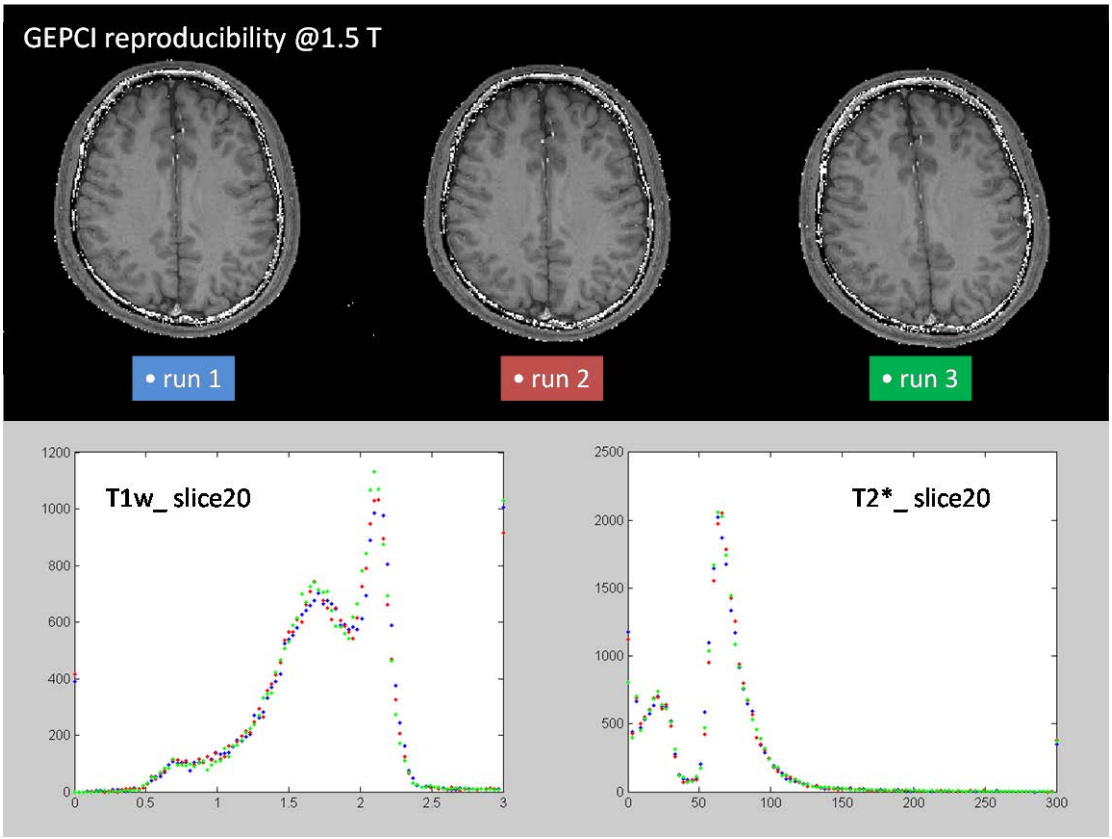

Figure 5.6 GEPCI reproducibility tested on healthy volunteer at 1.5 T scanner. Images on top shows T1w (S_0) images from run 1 to run 3. Histograms at bottom left show reproducibility of T1w image; histograms at bottom right show reproducibility of T2*. Blue, red and green points correspond to run1, run2, and run3 respectively.

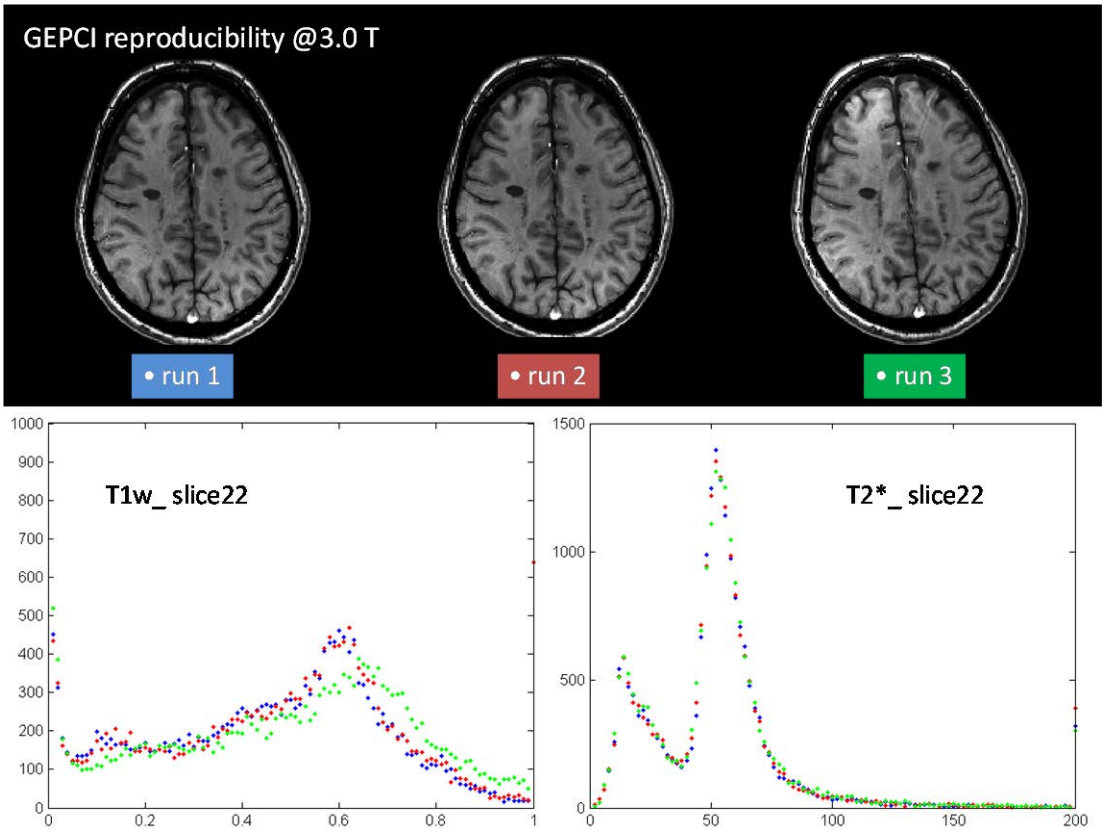

Figure 5.7 GEPCI reproducibility on MS subject at 3.0 T scanner. Images on top shows T1w (S_0) images from run 1 to run 3. Histograms at bottom left show reproducibility of T1w image; histograms at bottom right show reproducibility of T2*. Blue, red and green points correspond to run1, run2, and run3 respectively.

Histograms are chosen to characterize the reproducibility of T2* measurements. As shown in Figure 5.6 and Figure 5.7, T2* histograms show great reproducibility for all three scans both on healthy volunteer and patient. On the other hand, T1w intensity histograms show that after tilting head, T1 weighting shifted significantly due to different distribution of RF coil sensitivity.

5.3 Bridging the gap between radiological and clinical measurements of multiple sclerosis using Quantitative GEPCI Scores

5.3.1 Clinical tests

For each visit, patients are scanned with the standard MRI protocol introduced in Chapter 4, and also evaluated with clinical standard tests. EDSS (Expanded Disability Status Scale) evaluation is performed by experienced doctors. It is the "gold standard" for assessing impairment in MS (7). The MS Severity Score, a measure of aggressiveness of MS, was calculated based on the EDSS and duration of disease (135). MSFC (Multiple Sclerosis Functional Composite) is less subjective and more quantitative than EDSS, making it more amenable to statistical comparisons (136,137). The MSFC measures function, whereas the EDSS is neurologic examination. MSFC is comprised of timed 25 foot walk (test of ambulation), 9 hole peg test (test of upper extremity function) and 3 second paced auditory serial addition task (PASAT). PASAT is a standardized 10 minute test of information processing speed and attention/working memory, cognitive processes that are commonly impaired in MS. Since many of our early MS subjects score normal on the PASAT 3 sec version, we also include the 2 sec version. Symbol Digital Modality Test (SDMT) is also added in the protocol, it is demonstrated to be less susceptible to the practice effect than PASAT in measuring cognitive functions(138).

5.3.2 Baseline demographics

Characteristics	Values			
	overall	**RRMS**	**PPMS**	**SPMS**
Number of subjects	30	10	10	10
Age. y. median (range)	51.5 (27 to 70)	44 (27 to 52)	54.5 (40 to 70)	52.5 (41 to 64)
Gender. F:M	16:14	6:4	6:4	4:6
EDSS. median (range)	5.5 (1.5 to 8.0)	2.5 (1.5 to 6.5)	5.75 (3.5 to 8.0)	6.0 (4.0 to 6.5)
Disease Duration. y.	13 (3 to 34)	7 (3 to14)	9 (4 to 26)	25.5 (17 to 34)
MSSS. median (range)	5.25 (2.08 to 9.86)	4.27 (2.60 to 8.31)	7.11 (2.08 to 9.86)	5.25 (2.99 to 6.39)

Table 5.1 Baseline demographics

A group of 30 subjects - ten subjects each representing RRMS/SPMS/PPMS clinical subtypes (EDSS ranges 1.5-6.5/4.0-6.5/3.5-8.0) were recruited. The EDSS scores in each subgroup are chosen to be overlapping as much as possible. The RRMS group is younger than the other two groups. Since SPMS subjects by definition is at a fairly late stage of the disease, the disease duration of the SPMS subjects is much longer than the RRMS subjects.

5.3.3 Correlations in Clinical and Radiological measurements

Since our subject groups is small, and all parameters are not normally distributed, we used non-parametric Spearman ρ to examine cross correlations both within and between clinical measurements and traditional imaging measurements and GEPCI scores (we use the all 30 subjects as one group).

Correlations within clinical scores are shown in Table 5.2. EDSS is shown to highly correlate with MSSS, which is natural since EDSS is one of the determinants in

MSSS. On the other hand EDSS correlates poorly with all cognitive tests (PASAT 3'', 2'' and SDMT), suggesting that it reflect little cognitive dysfunctions. Although EDSS correlate highly with both MSFC 3'' and MSFC 2'', it is plausible to suggest that this correlation is driven by the 25' walk and 9-HPT components (especially the 25' walk which shows the strongest correlation with EDSS). MSSS and 25' walk show similar correlation patterns with other parameters as EDSS - poorly correlated with cognitive tests. MSSS shows weaker correlations with all other tests compared to EDSS, suggesting that the disease duration component in it does not play much role in functional tests. PASAT 2'' correlates strongly with PASAT 3'', and they both show similar correlations with other tests. As composite scores, MSFC 2'' and MSFC 3'' both find good correlation with all other parameters (except for MSSS). The 9-HPT test - as the upper extremity component of MSFC - correlated well with all other parameters, which indicates that this test is not limited to the upper extremity function.

	EDSS	MSSS	PASAT 3''	MSFC 3''	PASAT 2''	MSFC 2''	SDMT	25' Walk	9-HPT
EDSS		0.727 *****	-0.420 *	-0.679 *****	-0.364	-0.669 *****	-0.359	-0.866 *****	-0.623 ****
MSSS			-0.372 *	-0.541 ***	-0.179	-0.463 *	-0.263	-0.562 ***	-0.566 ***
PASAT 3''				0.822 *****	0.761 *****	0.705 *****	0.703 *****	0.339	0.583 ***
MSFC 3''					0.752 *****	0.940 *****	0.643 ****	0.711 *****	0.854 *****
PASAT 2''						0.834 *****	0.669 ****	0.478 *	0.522 ***
MSFC 2''							0.652 ****	0.7235 *****	0.824 *****
SDMT								0.384 *	0.545 ***
25' Walk									0.565 ***
9-HPT									

Table 5.2 Spearman ρ between Clinical Scores. p: Probability > $|\rho|$. * p<0.05, ** p<0.01, *** p<0.005, **** p<0.001, ***** p<0.0001.

	TDL	LL	MTDS	Width	Center	w/c
TDL						
LL	0.977 *****					
MTDS	0.624 ****	0.471 **				
Width	0.363 *	0.241	0.743 *****			
Center	-0.284	-0.250	-0.331	0.096		
w/c	0.408 *	0.276	0.821 *****	0.946 *****	-0.175	
LL- FLAIR	0.914 *****	0.867 *****	0.669 *****	0.476 **	-0.406 *	0.546 ***

Table 5.3 Spearman ρ between GEPCI scores. * p<0.05, ** p<0.01, *** p<0.005, **** p<0.001, ***** p<0.0001.

Correlations within MRI parameters are examined in Table 5.3. GEPCI scores are aiming to characterize two major features in the diseased brain - lesions and the brain as a whole. The TDL, LL and MTDS are defined as characteristics of lesion area. While LL is lesion load volume, TDL is the load of tissue damage weighted by damage severity. The strong correlation between TDL and LL could be due to the fact that by definition our TDL is also heavily weighted by lesion load, and the fact that patients with larger lesion load tend to have more severe damage (especially in SPMS subjects). The correlation between LL and MTDS also supports that. Global measures of the brain tissue are supposed to reflect properties of so-called 'normal appearing white matter (NAWM)', since although many parts of the brain do not show any abnormality (appear normal) in MRI scans, they have a lot of pathology under microscope (139). Width show very strong correlation with the MTDS. That could be partially due to our way of choosing the lesion 'cut-off' - we propose to do it at the $R2^*=R2_c^* - 1.96\sigma$, this inevitably means that when the width is broader, the lesions are cut at lower R2*, their mean tissue damage load will be higher. On the other

hand, center did not correlate with any of the other GEPCI parameters. As the mean value of the whole brain R2* distribution, the center might be affected by different factors other than the disease. For example, R2* would increase with iron accumulation, which is known to happen along the process of aging (140). Also, while we expect R2* decrease with neuronal tissue loss -> more water in the tissue, the brain suffers from atrophy at the same time, which reduces the total brain volume, thus counteracts the decrease of macromolecule concentration in tissue.

We have also calculated the lesion load based on the standard MRI technique – FLAIR and examined correlations with all GEPCI parameters. Strongest ones are with TDL and LL, which is expected. The correlation between FLAIR results and global GEPCI parameters is much weaker.

	EDSS	MSSS	PASAT 3''	MSFC 3''	PASAT 2''	MSFC 2''	SDMT	25' Walk	9-HPT
TDL	0.343	0.116	-0.314	-0.524 ***	-0.458 *	-0.644 ****	-0.444 *	-0.461 *	-0.454 *
LL	0.311	0.104	-0.292	-0.500 **	-0.447 *	-0.630 ****	-0.429 *	-0.458 *	-0.402 *
MTDS	0.176	0.033	-0.186	-0.298	-0.283	-0.344	-0.321	-0.196	-0.382 *
Width	0.127	-0.162	-0.083	-0.074	-0.130	-0.146	-0.141	-0.066	-0.166
Center	-0.017	-0.005	-0.038	0.088	0.004	0.057	0.073	0.088	0.120
w/c	0.142	-0.170	-0.069	-0.102	-0.061	-0.140	-0.136	-0.098	-0.193
LL- FLAIR	0.348	0.088	-0.254	-0.455 *	-0.307	-0.544 ***	-0.423 *	-0.405 *	-0.461 *

Table 5.4 Spearman ρ between GEPCI scores, FLAIR and Clinical measurements of disability. p: Probability > $|\rho|$

* p<0.05, ** p<0.01, *** p<0.005, **** p<0.001, ***** p<0.0001.

Table 5.4 shows correlations found between radiological and clinical scores. TDL and LL both correlate with MSFC 3'', MSFC 2'' and each of their components (except for PASAT 3'') and also SDMT, albeit not very strong with most of them. The fact that significant correlation does not exist between TDL and PASAT 3'' but does exist with the more sensitive PASAT 2'' indicates that GEPCI has high sensitivity in measuring brain abnormality. Subsequently, the stronger correlation between TDL and MSFC 2'' than 3'' is driven by the cognitive component. Note that the correlation between TDL and MSFCs is the strongest among all other scores, indicating that this correlation is not driven by any single component of MSFC. The lack of correlation between GEPCI and EDSS or MSSS (though both TDL and LL correlated with 25' walk moderately) show that GEPCI still in need of elements that assess other parts of CNS to perform more comprehensive evaluations for MS (same statement holds true for FLAIR-based lesion load count).

TDL did consistently better than LL with all their correlations, indicating that incorporating severity of lesion in the assessment does allow a stronger relationship between the radiological findings and functional impairments. No significant correlation is found between GEPCI global measures of the brain and disability tests. This might be attributed to the need of GEPCI data correction for magnetic field inhomogeneities which is a subject of current effort.

The FLAIR based lesion load assessment performs weaker than GEPCI scores (weaker in every correlation it has except for 9-HPT). We did not find correlation of FLAIR-LL with either PASAT 3'' or PASAT 2'', but there is some correlation between FLAIR-LL and SDMT.

5.3.4 Differentiating MS subtypes based on GEPCI or Clinical evaluations

As shown in the baseline demographics, this patient cohort is chosen to have three subtypes of MS patients, 10 each. In this section we try to determine how well GEPCI could discriminate the MS subtypes, and compare it with clinical scores' performance.

To accomplish that, we utilize the 'Decision Tree' method in the partition platform in JMP® (108). This program is convenient for exploring relationships without having a good prior model. In our case, the factor variables (X) are continuous, and the response variables (Y) are categorical (RRMS/PPMS/SPMS). The program recursively partitions data according to a relationship between X and Y values, creating a tree of splits. It finds a set of groupings of X values that best predict a Y value. It does this by exhaustively searching all possible groupings, and find the best among all candidates in X to do one split. Repeatedly splitting the data results in branches and leaves of the tree.

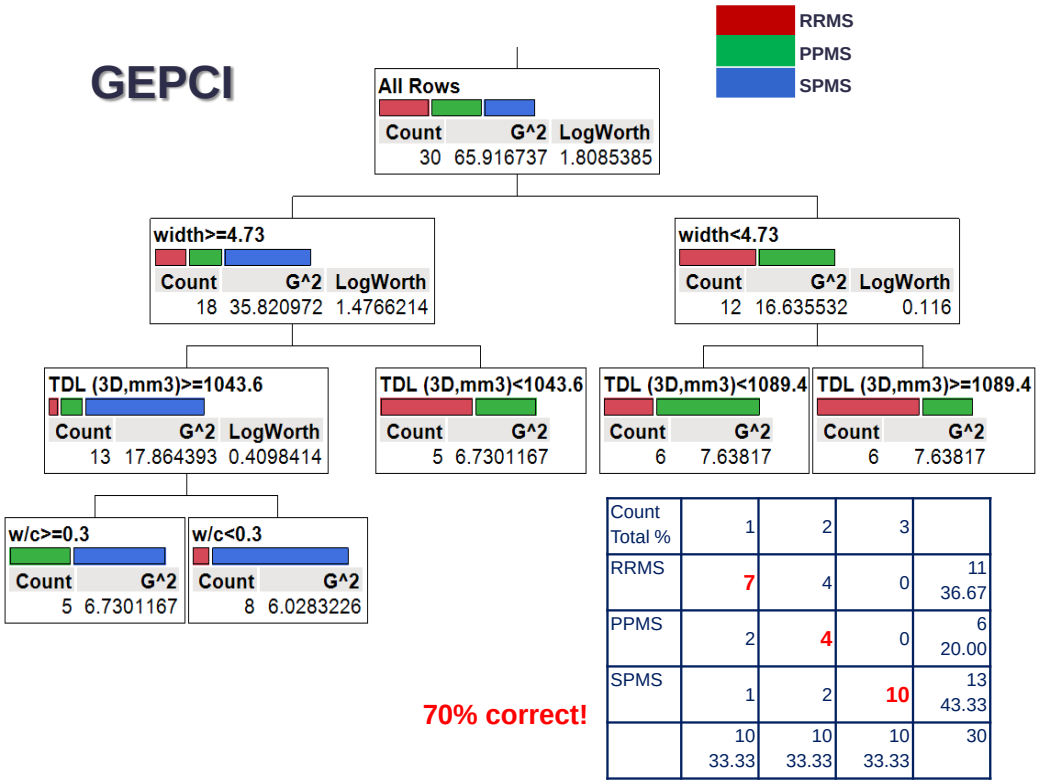

Figure 5.8 Decision tree and categorization of MS subtypes resulting from using GEPCI parameters alone.

First, we put all GEPCI parameters as potential factors to predict 30 subjects' MS subtypes. As shown in Figure 5.8, the decision tree started splitting by a global parameter in GEPCI 'width'. The left leaf corresponding to width >= 4.73, has 18 subjects, including all SPMS, 4 RRMS and 4 PPMS; the right leaf corresponding to width < 4.73, has 12 subjects, 6 RRMS and 6 PPMS. Then the tree grows with utilizing TDL as another factor. Groups of subjects are further split based on their tissue damage load. The w/c factor is used at last, but the final split does not affect the grouping results. In short, GEPCI is able to correctly identify all 10 SPMS subjects, 7 RRMS and only 4 PPMS, which adds up to total of 70% correctly grouped. The SPMS has broad width and

large TDL as expected; the PPMS group has small width and small TDL, which might be due to the reason that many PPMS subjects tend to have more lesions in their spinal cord; the RRMS group however, has either small width and large TDL or broad width and small TDL. The way RRMS group formed is very interesting. It might indicate that the inflammations in RRMS brains are highly dynamic processes, or that there are two kind of pathways for the disease to develop - finally they merge to SPMS (big width, big lesion). The high number of misclassification in RRMS and PPMS calls for extra information in GEPCI technique - spinal cord will definitely help! & measurement of brain atrophy may also improve the technique.

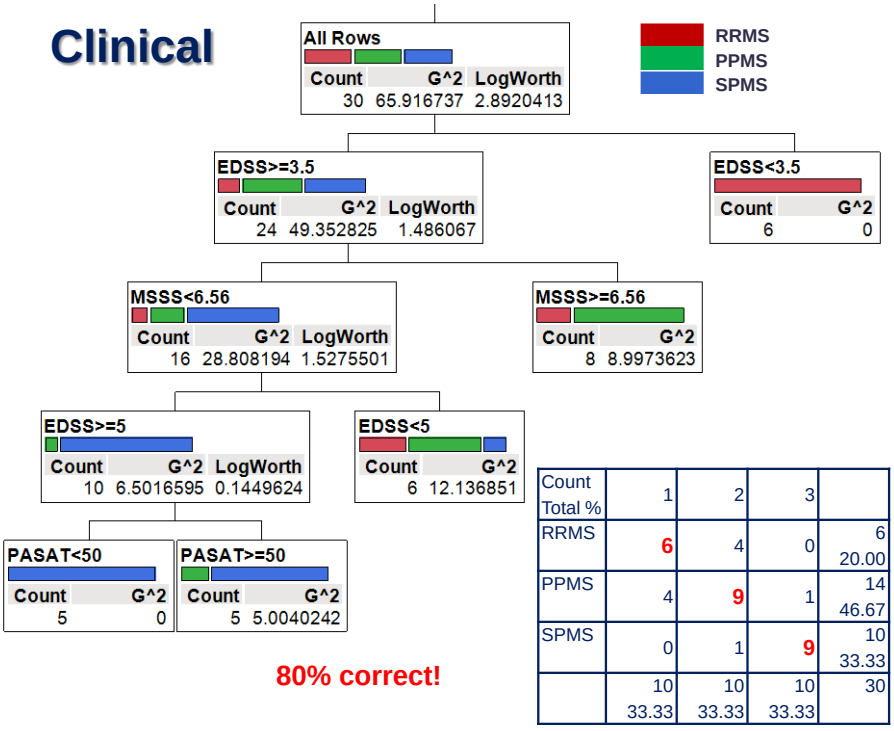

Count Total %	1	2	3	
RRMS	**6**	4	0	6 20.00
PPMS	4	**9**	1	14 46.67
SPMS	0	1	**9**	10 33.33
	10 33.33	10 33.33	10 33.33	30

Figure 5.9 Decision tree and categorization of MS subtypes resulting from using all clinical parameters.

In Figure 5.9 Decision tree and categorization of MS subtypes resulting from using all clinical parameters., 80% of all subjects are correctly identified. Among all clinical measurements, the program chose EDSS and MSSS for the entire grouping (the final split by PASAT did not affect results). Since the EDSS is the clinical 'gold standard' in measuring disabilities, and MSSS is result from EDSS and disease duration, they are expected to be strong in differentiating these MS subtypes. For example, 6 of RRMS and 9 of SPMS are identified by using EDSS alone (<3.5 and >5 respectively); also 6 PPMS got identified at the high end of MSSS since they progress from the disease onset without any recover episodes as RRMS.

Considering the fact that these clinical measurements are somewhat already affected doctor's judgments of MS subtypes, while GEPCI had no such advantages, it performs quite nicely in grouping MS subjects. Moreover, among 9 misclassified subjects by GEPCI, and 6 misclassified by EDSS and MSSS, they only have 1 (RRMS grouped as PPMS) in common, which suggests that the criteria offered by GEPCI and EDSS might have very different underlying mechanism. Larger sample size is needed for further validation of our observations.

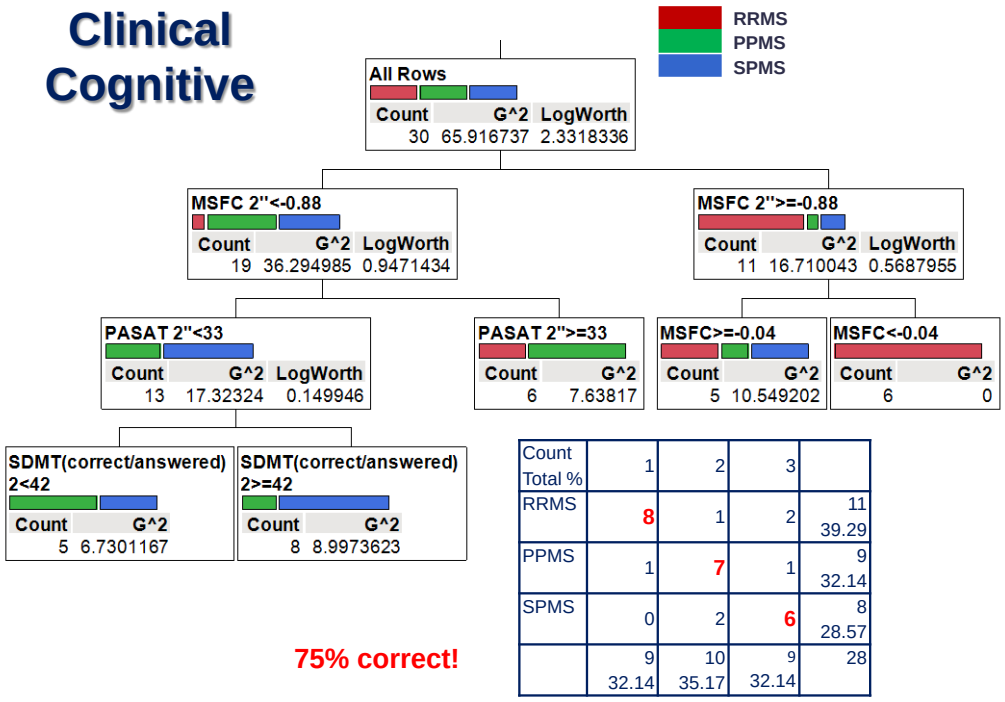

Figure 5.10 Decision tree and categorization of MS subtypes resulting from using clinical parameters excluding EDSS, MSSS and 25' walk.

Figure 5.10 shows results from using only cognitive tests to classify subjects. 21 out of 28 are correctly classified (2 missing values in PASAT 2"). The 7 misclassifications here also have only one overlapped with GEPCI (a PPMS grouped as RRMS by GEPCI, and grouped as SPMS by cognitive tests). And there are 3 misclassifications overlapped with EDSS/MSSS.

5.3.5 Summary

In summary, GEPCI offer multiple parameters in evaluating brain abnormality. TDL incorporates tissue damage severity in lesions; Lesion load provided by GEPCI scores correlate highly with clinical standard imaging FLAIR; GEPCI also provides measures beyond the lesions - distribution width and center assess changes in the NAWM. Among correlations between GEPCI and clinical tests, TDL and MSFC 2'' is the strongest (Spearman ρ = -0.644), and it's not driven by single component in MSFC. Both TDL and LL perform slightly better than FLAIR-LL. Although NAWM measures do not show correlations with clinical disability measurements, the 'width' does help with differentiating MS subtypes. GEPCI alone was able to correctly group 70% of all subjects, while EDSS/MSSS did 24/30, and cognitive scores did 21/28. This is not possible by using FLAIR-LL alone.

Although it remains a huge challenge to relate brain tissue damage in MR imaging to patients' clinical manifestations, compared to standard MRI scans, GEPCI is a big step forward in filling the gap between clinical and radiological measures.

5.4 Preliminary results of GEPCI in Spinal Cord Imaging[5]

As an important part of the CNS evaluation, spinal cord imaging is valuable in both diagnosis and ongoing evaluation of patients with multiple sclerosis (MS) (141). However, assessment of spinal cord damage using MRI lags behind the development of

[5] All contents have been published in Luo J, Cross AH, Yablonskiy DA. Quantitative evaluation of spinal cord tissue damage in MS patients using Gradient Echo Plural Contrast Imaging. Proc. Intl. Soc. Magn. Reson. Med. 2011; 2176.

brain methodology. Given GEPCI technique promise to provide substantial improvement in image quality and MRI acquisition time as compared to clinical sequences, and has already been used to quantitatively evaluate white matter tissue damage in brains of MS patients (40), it is tempting to use GEPCI technique to discriminate tissue damage in spinal cord of MS patients against normal subjects. This is an important step in development the GEPCI technique as a comprehensive tool for quantifying the extent of tissue damage of the whole CNS, and monitoring MS disease progression. Herein we provide preliminary results obtained in this direction.

Methods and Data Analysis: Data from the cervical spinal cord of healthy volunteers and relapsing-remitting MS patients were acquired using a Siemens® 3.0T Trio MRI scanner. A 3D version of GEPCI sequence was used with high isotropic resolution of 1x1x1 mm^3 and 11 gradient echoes (8min32s acquisition time). Further effective resolution enhancement was achieved with zero-filling in the k-space. A set of five standard clinical 2D turbo spin echo T1w and T2w images were acquired with a total imaging time of 16 min. Saturation band was applied on the anterior portions of the torso, to suppress motion artifacts. GEPCI technique simultaneously generates naturally co-registered quantitative T2* and R2*=1/T2* maps, along with T1-weighted (T1w) images. Data were analyzed using Matlab®. Isotropic resolution allows image reconstruction in arbitrary plane, thus providing great advantages over clinical methods. Mask for spinal cord area including both white matter and gray matter was obtained with segmentation based on the T1w-GEPCI images. R2* histogram of the whole cord is generated using a bin width of 0.3 s^{-1} ranging from 0 s^{-1} up to 30 s^{-1}.

Results and Discussion:

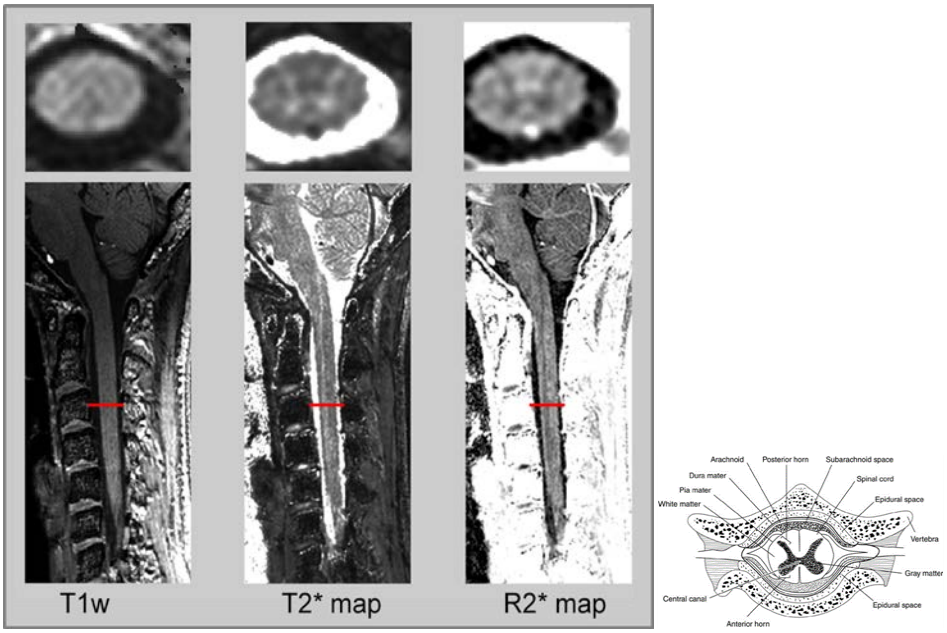

Figure 5.11 Examples of GEPCI-T1w (left column), T2* map (middle column) and R2* map (right column) of the spinal cord. Bottom row is the sagittal view; Upper row - magnified views of the transverse cut through the spinal cord corresponding to the red line on the sagittal view. All images are reconstructed from the same GEPCI 3D data set. The image on the right represents anatomy of spinal cord at a similar level;

In Figure 5.11, characteristic butterfly pattern of the grey matter is clearly seen on axial GEPCI R2* map. Remarkably, the grey matter is also seen on the sagittal views (bright T2* / dark R2* lines inside the spinal cord).

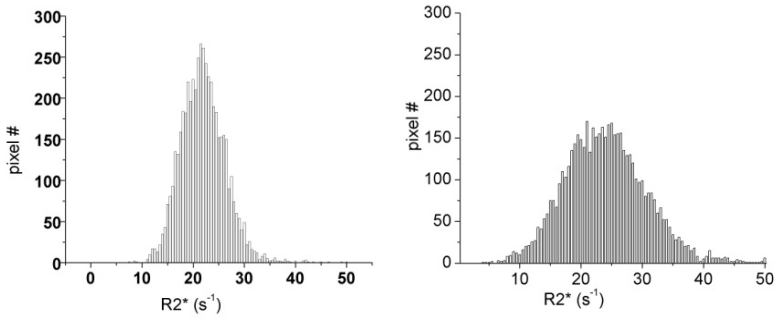

Figure 5.12 Examples of the R2* histograms of c-spinal cord of a healthy control (left) and MS subject (right).

In Figure 5.12, the width of the distribution (variation of the R2* values) of RRMS subject (12.9 s^{-1}) is substantially greater than the R2* variation of control subject (8.32s^{-1}) suggesting diffuse MS tissue damage.

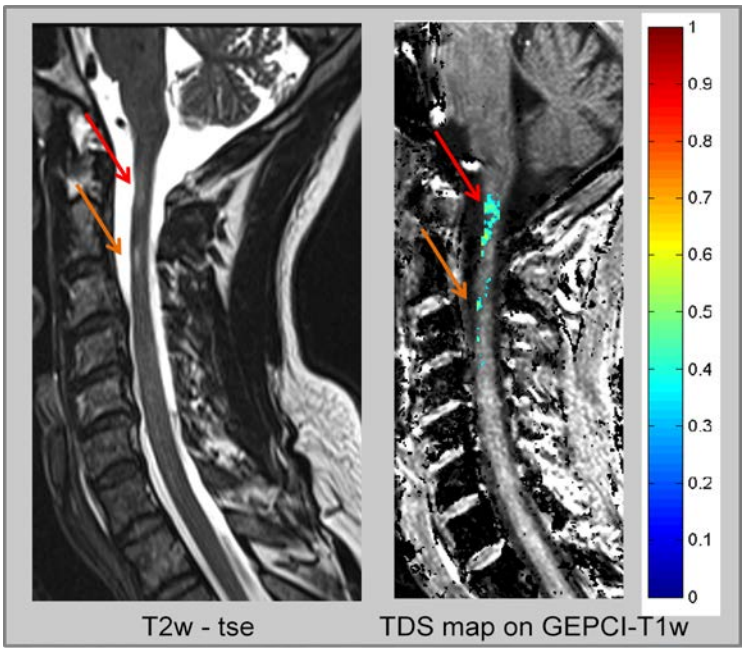

Figure 5.13 Images of an MS patient. Standard T2-weighted image is shown on the left; GEPCI score map is shown on the right.

We can clearly see 2 lesions on the clinical T2-weighted image (left) around C1 and C2

area. Lesions on GEPCI image (right) showed up at similar positions.

TDS (tissue damage score) of MS lesions was generated based on the R2* distribution shown in Figure 5.12, which indicates relative severity of the lesions. It was subsequently overlapped on the naturally co-registered GEPCI-T1w image. Definition of the lesion score here is analog to what was done for the MS brain lesions (see 5.2.1 Tissue Damage Score)

Spinal MS lesions are rarely depicted as hypointense on clinical T1w images, which indicates that the pathological changes in the tissue are not sufficient to produce contrast in T1w images (141). Similar situation is seen in our GEPCI-T1w image. However, quantitative R2* histograms shown in Figure 5.12 clearly differentiate normal from MS tissue. One of the problems with the clinical standard T2/T1 weighted images is that the intensity of the image is affected by the RF coil sensitivity and homogeneity of the RF field. Indeed we also observe image intensity variation (both up-to-bottom and left-to right) in our T1w images (Figure 5.11, left). However, as seen in Figure 5.11 (middle and right), the R2* and T2* GEPCI maps, being quantitative, are exempt from the sensitivity problem.

In summary: In this section, we demonstrated the capability of extending GEPCI technique to spinal cord imaging in general and quantitative evaluation of tissue damage in MS. High quality images were collected twice faster compared to standard clinical MS protocols. As a quantitative technique, GEPCI holds promise toward comprehensive characterization of MS abnormalities in the spinal cord. Also note that the cerebellum

and brain stem areas showed very good contrast with our resolution, which further strengthens the promise for GEPCI technique to characterize the whole CNS.

5.5 Preliminary Results of GEPCI with Detecting Cortical Lesions in *Ex Vivo* MS Brain[6]

Although most imaging research in Multiple Sclerosis has focused on the white matter, pathology can also be found in gray matter, including cerebral cortex. MS symptoms and signs including cognitive impairment, fatigue, and seizures have been linked to gray matter involvement (111). Conventional MRI techniques that are routinely used to detect MS lesions are T1 and T2 weighted spin-echo images and FLAIR, which detect white matter lesions well, but miss most cortical lesions, as reported in a postmortem tissue-MRI correlation study (142) at field strength of 1.5 T. Though higher fields will result in increased detectability of both cortical and WM lesions (143), these imaging techniques will suffer from high specific absorption rate (SAR), especially at 7.0 T. GEPCI on the other hand, is a technique based on multi-echo gradient echo sequence, which has very low SAR. In this pilot study, we evaluated GEPCI as a way to detect and quantify cortical lesions.

Material and Methods: Acquisition: Brain tissue of an *ex vivo* MS patient was scanned on a Varian 4.7 T MRI. Sample prepared as figure on the left. A 3 cm diameter bird cage coil was used to obtain a 3D version of the multi-echo gradient echo sequence with a

[6] All contents have been published in Luo J, Cross AH, Schmidt R, Sukstanskii AL, Yablonskiy DA. Detecting cortical lesions in MS tissue with Gradient Echo Plural Contrast Imaging. Proc. Intl. Soc. Magn. Reson. Med. 2012; 3123.

resolution of 0.11 x 0.11 x 0.5 mm^3, FOV of 40 x 40 x 8 mm^3 and 8 gradient echoes (TR = 200 ms; minTE = 4.58 ms; delta-TE = 7.6 ms; bandwidth = 40 kHz/FOV; FA = 60°, acquisition time = 13 min). 2D T2 weighted images were also acquired with spin echo sequence at different TE separately, (TR = 4000 ms; TE = 13 ms, 50 ms; acquisition time = 8 min x 2) and slices of same orientation.

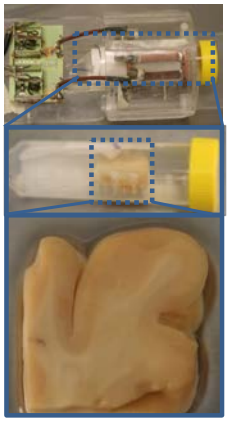

Figure 5.14 Demonstration of tissue sample and experimental set-up.

Image Analysis: GEPCI data were analyzed assuming mono-exponential signal decay and attenuation due to macroscopic field inhomogeneities, describing by *F*-function as discussed in (6): $S(TE_n) = S_0 \cdot e^{-R2^* \cdot TE_n} \cdot F(TE_n)$. The fitting to magnitude data produces two naturally co-registered basic GEPCI images: quantitative T2* = 1/R2* map and T1-weighted images (S_0). The frequency maps are obtained from phase data and used for calculation of *F*-function (6). As for T2 mapping, T2 weighted images at two echo times were fit by a mono-exponential decay: $S(TE_n) = S_0' \cdot e^{-R2 \cdot TE_n}$, which results in a T2=1/R2 map and a Spin Density image (S_0'). All data were Hann-filtered to improve SNR before fitting procedures.

Results & Discussions: As shown in Figure 5.15, T2* map, T1-weighted image and T2 map showed very well defined cortical lesion (red arrows). Sub-cortical structures are

also observed on GEPCI images and T2 map. The contrasts in cortical structures are not seen on the Spin Density images. It has been reported that focal cortical lesions are often extensive in MS (46). Unfortunately, cortical lesions are often completely missed with conventional MRI techniques, due to limited signal contrast between cortical grey matter and lesions. Double Inversion Recovery (DIR) has been reported to have significantly improved detection of cortical lesions (142), but it is often difficult to distinguish true lesions from artifacts using DIR, and problems are anticipated with high energy deposition at high field.

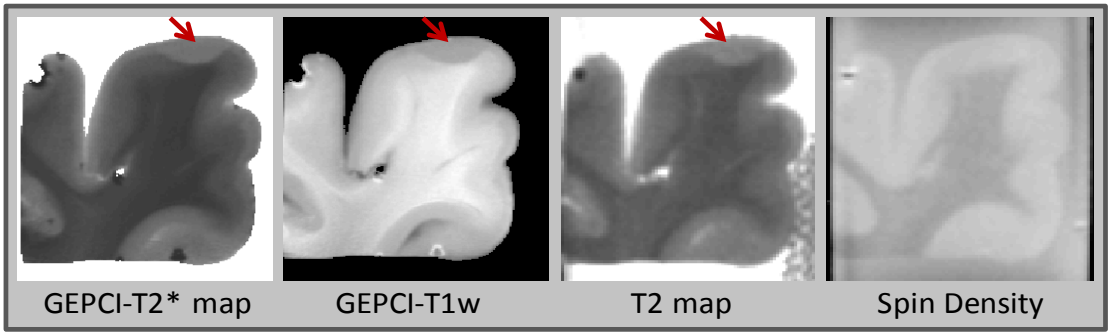

Figure 5.15 Results of GEPCI technique and T2 mapping.

In summary: In this pilot study, we have demonstrated that GEPCI technique is sensitive to cortical lesions and sub-cortical structures on *ex vivo* MS tissue. GEPCI holds much promise for the future, as the multi-echo gradient echo sequence upon which GEPCI is based has no problem with energy deposition at high field and it is very rapid; one would have to trade off resolution and/or SNR significantly to creates maps of T2 with similar amount of time.

Chapter 6 Mapping of Phase – Application of GEPCI to monitoring Multiple Sclerosis[7]

6.1 Inconsistency between magnitude image and phase image of MS brain.

6.1.1 Overview

MRI has played a revolutionary role toward enhancing knowledge in biology and medicine. Numerous MRI techniques have been developed over the years to aid physicians and scientists in understanding tissue structure and function in health and disease. One MRI technique that has been of increasing interest in recent years relies on phase images obtained by GE (gradient echo) MRI. It was demonstrated that phase images provide image contrast distinct from T1 weighted (T1W) and T2 weighted (T2W) images (e.g.(3,42-45,144)). However the sources of phase contrast have not been completely understood and are a subject of intense debate. Myelin was proposed as one of the main contributors to MR signal phase in white matter (145) and it was demonstrated that demyelination leads to a loss of phase contrast between white matter (WM) and gray matter (46) (54,146). This could have been explained by the difference in tissue cellular/molecular content (iron, lipids and proteins) between GM and WM. Yet it was also reported that phase contrast is practically absent between WM and CSF (3,144) despite substantial differences in their molecular content. Iron was shown to play an important role in formation of phase contrast in iron-rich areas such as caudate,

[7] All contents in this chapter have been accepted for publication in Yablonskiy DA, Luo J, Sukstanskii AL, Iyer A, Cross AH. Mapping MRI signal frequency to reveal central nervous system damage: biophysical mechanisms and application to multiple sclerosis. submitted to Proc. Natl. Acad. Sci. USA.

putamen, and globus pallidus (69,147-149). However, experimental data on the role of iron in WM is controversial – while a decrease of the phase contrast after iron extraction from the fixed brain tissue was reported in (145), this effect was not seen in (54). It was also concluded in (60) that the MR phase contrast between cortical gray and white matter can be mainly attributed to variations in myelin content, but not to iron concentration. Similar uncertainty exists in the study of multiple sclerosis (MS) using phase imaging, one of its emerging applications. In initial publications (148,150,151), a variety of manifestations of MS lesions in phase images were reported. It was noted that some lesions seen on phase images were also seen on T1W and T2W images, but some alterations were unique to phase images. Also some lesions detected on T1W and T2W images were not seen on phase images. One hypothesis proposed to explain phase contrast is based on an assumed mechanism that relates MR signal phase/frequency shift to iron content in the tissue. (148,150,151) However this mechanism does not take into account the hallmarks of MS lesions - the loss of axons and myelin (10).

Bridging the gap between these controversial findings is one of the main goals of this Chapter. To this end we provide theoretical background to the hypothesis that the local contribution to the MRI signal phase depends not on bulk tissue content but on tissue "magnetic architecture" - distribution of magnetic susceptibility inclusions (lipids, proteins, iron, etc) at the cellular and sub cellular levels (144). This allowed us not only to shed new light on the above-mentioned controversies but also to propose a theory of MRI phase contrast in MS. We demonstrate herein that according to this mechanism, phase contrast in MS lesions could appear simply because of injury to the myelin sheath, even without its removal from the affected area, thus preserving bulk tissue

magnetic susceptibility. Our theoretical concept indicates that phase contrast is sensitive to mild lesions, and thus may appear abruptly at lesion onset when damage is still minimal. Our preliminary data in several human subjects show abnormalities seen only on phase and not magnitude images, within the areas with borderline abnormal tissue damage, which can be explained by our theoretical prediction that the phase contrast in MS lesions could be altered with mild injury to the myelin sheath or axonal neurofilaments. Hence these phase abnormalities may represent mild or early MS lesions. Contrary to a common-sense expectation that the phase contrast in MS lesions should always increase in degree along with worsening of lesion severity (as happens for all known MR magnitude-based contrast mechanisms), we demonstrate that phase contrast can actually disappear in situations of medium to severe tissue destruction. Moreover, we predict that the sign of phase contrast in MS lesions indicates the predominant type of tissue injury – myelin damage (positive sign) vs. axonal neurofilament damage (negative sign). In the current paper, we provide theoretical and experimental evidence supporting these mechanisms of phase contrast in MS lesions. Our findings have potential to expand the information provided by CNS imaging both for understanding MS pathophysiology, and as an endpoint in clinical trials (152).

6.2 Phase Contrast in MS brain – Theoretical predictions

6.2.1 Phase Contrast in White Matter - Theory

Tissue magnetic architecture at the global (organ or body part) and at the cellular/sub-cellular levels depends on the structural (geometric) arrangement of the main tissue

components (proteins, lipids, iron, etc) that, as far as MRI is concerned, act as magnetic susceptibility inclusions. In an external magnetic field B_0 magnetic susceptibility inclusions become magnetized and induce their own magnetic fields that affect (shift) Larmor resonance frequencies of water molecules. White matter structure can be described as mainly comprised of quasi-cylindrical myelinated axons. The induced magnetic field in these axonal bundles (tracts) is generated by several sources: (a) longitudinally arranged myelin sheaths and intra-axonal neurofilaments that run mostly parallel to the axonal tract axis, (b) isotropically distributed free floating organelles, proteins, lipids, etc., and (c) the interface between the white matter tract and the surrounding tissue.

In a GE experiment, the contribution of each water molecule, diffusing in the inhomogeneous magnetic field, to the MR signal at GE time *TE* can be represented as $\exp(i\varphi(TE))$ where $\varphi(TE) = \gamma \int_0^{TE} b(r(t))dt$ is the phase accumulated by the diffusing molecule along its trajectory $r(t)$; $b(r(t))$ is a projection of the local magnetic field, created by all the sources of magnetic field inhomogeneities at point $r(t)$, on the external magnetic field B_0. According to well known results followed from Maxwell equations, the distribution of magnetic fields in the cylinder-like structures depends mostly on the position in the transverse plane. Since in white matter water molecules are confined either to intracellular or extracellular spaces with the transverse sizes about or less than 1 μm, it requires less than 1 ms to sample the whole distribution of magnetic field within a given compartment (water diffusion coefficient is about 1 μm^2/ms). Hence for gradient echo time *TE* greater than 1 ms used in experiments, all diffusing nuclei in the same compartment sample the whole distribution of magnetic fields within a given

compartment and, therefore, accumulate similar phases (motional averaging regime). Effectively, a diffusing water molecule "feels" an average magnetic field $\langle b_m \rangle$ in the compartment where it resides, hence

$$\varphi_m(TE) = 2\pi \Delta f_m TE; \quad 2\pi \Delta f_m = \gamma \langle b_m \rangle \qquad [6.1]$$

where Δf_m is an average frequency shift in m-th compartment. Based on this consideration, only an average magnetic field in each compartment should be calculated. In what follows, we will use Eq. [6.1] and computer Monte-Carlo simulations to quantify influence of WM microstructure on MR signal phase. For this purpose we will initially use a simple model of axonal structure presented in Fig. 1.

6.2.2 Monte-Carlo Simulations of Phase Contrast in Intact and Destructed Tissue

Figure 6.1A represents a schematic structure of an intact myelinated axon (intracellular water, myelin sheath and extracellular water). Computer Monte-Carlo simulations of the MR signal frequency shift were performed in the intact myelinated axon and in an axon undergoing demyelination typical of MS (Figure 6.1B and C). The latter was modeled by fragmenting the cylindrical structure of the myelin sheath to different degrees. The fragments were modeled as spheres with positive magnetic susceptibility with respect to water (because lipids and iron each provide a positive magnetic susceptibility, whereas proteins have a primarily negative contribution (144)). The phase accumulated by diffusing water molecules was calculated based on the well known expressions following

from Maxwell equations for magnetic field created by cylinders and spheres (see for example (72)).

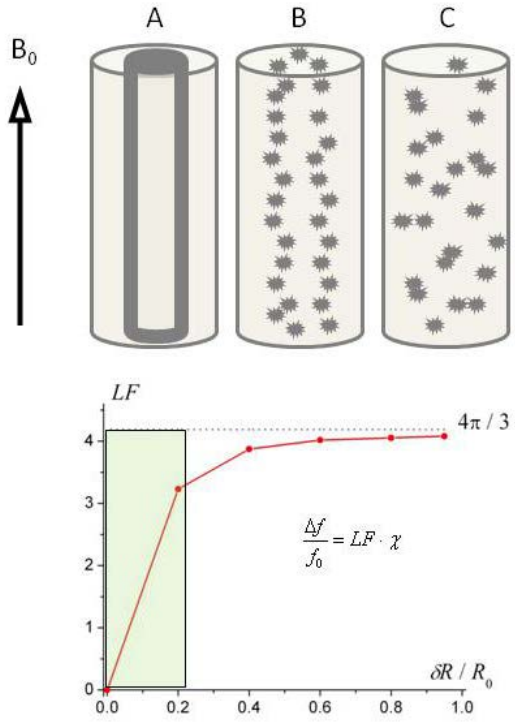

Figure 6.1 Effect of increasing myelin sheath damage on phase/frequency of MR signal derived from computer Monte-Carlo simulations. A) schematic of an intact axon (internal cylinder) covered by a myelin sheath (bold outline of cylinder) in an extra-cellular space (between bold and outer cylinder) with radius R_0. B) "Mildly" damaged myelin sheath – fragments of original structure are slightly scattered. C) "Severely" damaged myelin sheath - fragments of initial structure are scattered randomly. Lower panel -- dependence of the Lorentzian Factor (*LF*) in the MR signal frequency shift on the "level of distraction" (*δR* – average fragments' displacement). Shaded zone (0-0.2) indicates minor injury to tissue, wherein even a small increase in the "disorder" parameter *δR* (horizontal axis) will rapidly and dramatically change the Lorentzian Factor, and hence will also change signal phase/frequency.

The calculations revealed that for all the structures in Fig. 1, the water MR frequency shift could be described by the following equation:

$$\Delta f / f_0 = LF \cdot \chi \qquad [6.2]$$

where χ is a total (bulk) volume magnetic susceptibility of inclusions (myelin sheath and/or its fragments). The proportionality coefficient *LF* (referred hereafter as "Lorenzian Factor") varies with different levels of damage to the myelin sheath. Note that the Lorentzian Factor is equal to $4\pi/3$ only for randomly scattered fragments; this case is usually referred to as a Lorentzian Sphere approach (e.g., (62)). For all other cases, *LF* is less than $4\pi/3$, approaching zero for the intact axon. Therefore, as previously suggested (144), the Lorentzian sphere approach is not valid for describing the magnetic susceptibility frequency shift in normal WM which is highly directional.

An additional factor that contributes to the frequency shift is the object's (axonal) general external shape:

$$\Delta f / f_0 \big|_{shape} = SF \cdot \chi \qquad [6.3]$$

For the structure in Fig. 1, where B_0 is parallel to the axonal axis, the shape factor *SF*, Eq. [6.3], is zero and the frequency shift is completely determined by the Lorenzian Factor *LF*, Eq.[6.2].

The results of Monte-Carlo simulations for an oblique direction of an axon with respect to magnetic field B_0 are shown in Fig. 2. An important conclusion from this figure is a prediction of zero frequency shift for the intact axon, regardless of axonal orientation.

This important result is due to cancellation of contributions from *Lorentzian Factor* characteristic for longitudinal structures, $LF\big|_{longitudinal} = 2\pi \cdot \sin^2 \alpha$ (144), and the shape factor for circular cylinder, $SF\big|_{cylinder} = -2\pi \cdot \sin^2 \alpha$. At the same time, for a scattered case (C), the Lorentzian factor is equal to $4\pi / 3$ and does not depend on axonal orientation, whereas the shape factor does.

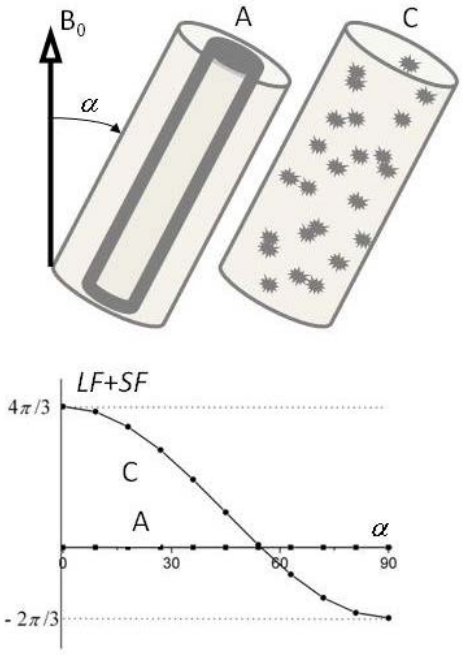

Figure 6.2 Dependence of MR resonance frequency shift, derived from computer Monte-Carlo simulations, on the angle α (in degrees) between axonal direction and the external magnetic field B_0 for an intact axon (A) and randomly-scattered myelin fragments (C).

Figure 6.1 and Figure 6.2 present results for a simplified case when only intact or damaged myelin sheath contributes to a susceptibility-induced MR signal phase shift.

The true situation is more complicated due to the presence of components in addition to myelin and will be discussed below. However, the contribution from proteinaceous neurofilaments is qualitatively similar (though with the opposite sign) because they are also organized in longitudinal structures.

6.2.3 Theoretical Predictions of Frequency Shift between Intact Axon and Surrounding Tissue – Effect of WM "Darkness"

To understand phase contrast in injured MS tissue, we first need to understand phase contrast in a normal brain. In general, the intact myelinated axon can be described as comprised of longitudinal structures with magnetic susceptibility χ_L (myelin and neurofilaments) aligned along the axonal axis, and isotropic components (free floating organelles, proteins, lipids, etc) with magnetic susceptibility χ_i. Hence, the total "Lorentzian contribution" to the MR signal frequency shift is a combination of the two: $\Delta f / f_0\big|_{Lorentzian} = 2\pi \cdot \chi_L \cdot \sin^2\alpha + \frac{4}{3}\pi \cdot \chi_i$. For a circular cylindrical myelinated axonal bundle (tract) surrounded by an isotropic media (like CSF or gray matter) with magnetic susceptibility χ_e, the contribution from the interface (tract shape factor SF) between the tract and the media is equal to $-2\pi \cdot \sin^2\alpha \cdot (\chi_{WM} - \chi_e)$, where $\chi_{WM} = (\chi_L + \chi_i)$ is the total susceptibility of WM. Thus, the total frequency difference between a circular cylindrical axonal tract and the external media can be written as

$$\Delta f / f_{0\,axon} = \left(-2\pi \cdot \sin^2\alpha + \frac{4}{3}\pi\right) \cdot (\chi_i - \chi_e) \qquad [6.4]$$

Note that for non-circular cylindrical tracts this dependence is more complicated (144).

The fact that the longitudinal structures (myelin sheaths, neurofilaments, etc.) do not contribute to the total frequency shift of the cylindrical axon when magnetic field B_0 is parallel to the axonal axis is a direct consequence of Maxwell equations: the induced magnetization of long cylindrical structures parallel to B_0 does not create any magnetic field outside the structures themselves. This is not true when B_0 forms an angle with the axonal axis. However, the average magnetic field contributing to the frequency shift around intact myelin sheath (or neurofilament) is zero for an arbitrary orientation of B_0 with respect to the axonal axis. Monte-Carlo simulations (see Figure 6.2) confirm this result, which is also in agreement with published predictions (144).

One of the important consequences of Eq.[6.4] is that the terms proportional to χ_L cancel each other for circular cylindrical axonal bundles, i.e. *the longitudinal structures do not contribute to frequency contrast between such a bundle and any adjacent isotropic media*. Therefore, in the regions of the brain, such as the cortex, where gyri and sulci abut one another, the intact cylindrical axons in gyri should have very small frequency shifts relative to CSF in the sulci. This effect, first predicted by He and Yablonskiy (144), is counter-intuitive because there is a substantial difference between the total magnetic susceptibility of WM ($\chi_{WM} = \chi_L + \chi_i$) and that of CSF ($\chi_e$). One could, therefore, expect a substantial phase contrast between WM and CSF. However, according to Eq. [6.4], the frequency shift is determined not by the difference $(\chi_{WM} - \chi_e)$ but the difference $\chi_i - \chi_e$, where χ_i comprises a small fraction of the total magnetic susceptibility of WM χ_{WM}, leading to very little contrast between WM and CSF (144).

In the same manner, Eq. [6.4] also explains negative WM/GM contrast which is also counterintuitive because WM has higher magnetic susceptibility than GM (144). However, according to Eq. [6.4] the phase/frequency contrast between WM and GM is proportional to $\chi_i - \chi_{GM}$, which is essentially magnetic susceptibility of GM (with the negative sign) since χ_i comprises only a small fraction of the total magnetic susceptibility of WM. These results are in agreement with previous observations (3,144) where the dominant "bright" regions in phase images belong to GM, while WM and CSF are usually dark. Exceptions are areas of high concentrations of iron, e.g. caudate nuclei (148). Such a dark background provides a convenient display for MS lesions that have mostly (but not always) positive phase (see examples in Figure 6.3) due to the effect of myelin "disordering" in MS.

6.2.4 Theoretical Predictions – Frequency Shifts in MS Tissue

An essential feature of the plot in Figure 6.1 generated by computer simulations is the steep growth of the *LF* predicted to occur with only minor damage to the myelin sheath (shaded zone). Thus, even small abnormalities in MS-affected CNS may cause substantial (positive in sign) changes in MR signal phase. A theoretical consideration for axonal damage (destruction of neurofilaments) leads to a similar scenario with one important difference – phase/frequency as a function of neurofilament destruction experiences negative changes. This is because neurofilaments are formed from proteins that have a negative magnetic susceptibility with respect to water, whereas myelin is >70% lipid and also contains relatively more iron, each having positive susceptibility with respect to water (144). Since frequency shift in Eq. [6.2] is a product of two factors – *LF* and tissue magnetic susceptibility (χ_L in this case), one can expect that with tissue

destruction, phase will experience major changes for mildly damaged longitudinal structures due to the steep increase in *LF.* On the other hand, decrease in tissue magnetic susceptibility due to tissue removal from the damaged area may lead to reduction of phase/frequency changes for severely damaged tissue. To characterize tissue damage in MS we use a previously introduced (40) quantitative parameter – tissue damage score (*TDS*). *TDS* around zero corresponds to normal tissue and *TDS* =1 corresponds to severely injured tissue ('black holes"). Both *TDS* and MRI signal frequency/phase are obtained herein using gradient echo plural contrast imaging (GEPCI) technique (39) which is described in the 'experimental results' section in 6.3.

Importantly, the sign of phase/frequency changes depends on the type of injured tissue (axonal filaments vs. myelin). With myelin damage and intact neurofilaments, the change is positive, whereas in the case of damage to proteinaceous neurofilaments within intact myelin the change is negative. This scenario is depicted in Figure 6.3. However, the latter case would typically occur in the setting of myelin destruction with a possible additional components of lipids and iron which would offset the negative phase change. This is consistent with our and others (151) observation of negative phase changes in MS lesions being very rare.

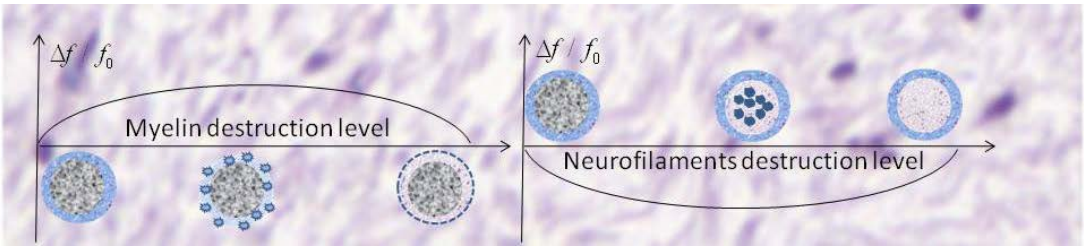

Figure 6.3 Schematic structure of the MR signal phase/frequency change with MS lesion severity for two types of tissue destruction: left panel – pure myelin injury, right panel –

pure injury to neurofilaments. Minimal myelin injury which may not be apparent on standard T2W and T1W images will appear positive by phase, corresponding to the initial ascending portion of the left figure (and also lower panel Figure 6.1). For moderately severe lesions with predominant myelin injury (center of the left figure, medium TDS score), phase will also be positive. However, axon destruction is often also present, and the relative degree of myelin and neurofilament destruction will affect the sign of the phase change. Severe lesions such as persistent black holes, with a high TDS score and significant destruction of both myelin and axons might disappear on phase images.

Based on the above consideration, the following scenario describes MRI phase/frequency behavior according to the type and severity of MS tissue damage.

(i) Normal WM, having mostly longitudinal structure, has little local effect on MR signal phase.

(82) At the initial stages of MS lesion development with demyelination, small alterations in this longitudinal structure would become visible on phase images. This might happen even before detection using other techniques. Hence, MR signal phase might serve as a very sensitive biomarker for minimal abnormalities or early MS lesion development. Importantly, damage to myelin would cause an increase in signal phase (positive contrast), while damage to axons would cause a decrease of signal phase (negative contrast). When axons degenerate, the surrounding myelin is also subsequently lost due to Wallerian degeneration. Thus, one would expect negative phase contrast to be relatively uncommon. If both myelin and axons are damaged, the phase contrast could

disappearbecause myelin and protein-based neurofilaments have opposite magnetic susceptibilities resulting in opposing frequency shifts.

(iii) For severely injured tissue, when cellular components (macromolecules) are removed from the site, magnetic susceptibility becomes small leading to decreased phase contrast. Hence for many cases with medium and severe damage, one can expect very small phase contrast. This can explain previous reports of phase changes being detected only for a subset of MS lesions (see for example (148,150)).

6.3 Phase Mapping in MS - Experimental Results

6.3.1 Materials and Methods

Image Acquisition: Brain images were collected using a Siemens 3T Trio MRI scanner (Erlangen, Germany) and a 12-Channel phased-array head coil.

GEPCI data were obtained using a 3D version of the multi gradient echo sequence with a resolution of 1x1x3 mm^3, FOV of 256 mm x 192 mm and 11 gradient echoes (TR=50 ms; First TE=4ms, δTE=4 ms; FA=30°). To generate GEPCI images raw data were reconstructed using Eq.[4.5]. The frequency maps were high-pass filtered to remove effects of macroscopic field inhomogeneities using a 7x7 (out of 256x256) in-plane averaging matrix. Image reconstruction and post-processing were performed using a standard PC computer and Matlab software (MathWorks Inc.). The automatic shimming procedure available on the Siemens scanner allowed substantial minimization of macroscopic field inhomogeneity effects in most parts of the brain. Hence, a simple fitting of the mono-exponential to the GEPCI signal was sufficient to generate GEPCI

T2* and T1W images. GEPCI-FST2Star images that are R2* maps with suppressed signal from CSF and GEPCI T1f images (a combination of GEPCI T1W and frequency maps) with enhanced GM/WM contrast (39) were also created.

Standard clinical images were also obtained: Forty-four contiguous 3-mm axial imaging sections were obtained with a 24-cm field-of-view (FOV), a matrix size of 256 x 192, and using two types of Turbo SE (TSE) sequences: 1) T2-weighted images with TR = 6800 ms and TE = 95 ms, Bandwidth=151 Hz/Px, Turbo factor=7; 2) FLAIR images with TI = 2310 ms, TR = 10000 ms and TE = 83 ms, Bandwidth=219 Hz/Pixel, Turbo factor=13; 3) T1-weighted images using a standard SE sequence with TR = 600 ms and TE = 12 ms, Bandwidth=130 Hz/Pixel; Total time for these three standard sequences was 16 minutes.

Human Subjects: The human studies were approved by the Washington University IRB. One normal healthy subject, four subjects with relapsing remitting MS (RRMS) disease (gender/age/EDSS = M/42/1.5, M/52/3.5, M/39/2.5, F/42/2.0) and one with secondary progressive (SPMS) disease (gender/age/EDSS = F/49/6.5) (5,153) entered the study. Sixty lesions were studied by GEPCI magnitude and phase, and standard imaging.

6.3.2 Experimental Results

Example in Figure 6.4 shows one MS lesion that has a range of tissue damage scores (TDS) from normal on periphery to severe damage at the lesion center. On FLAIR image it manifests itself as a bright ring with a dark core. The appearance on GEPCI frequency map is similar to the appearance on FLAIR though the abnormality is bigger in size and is surrounded by two dark strips. The sign (positive frequency – myelin damage) and

pattern of phase changes as compared to GEPCI TDS score are in agreement with our prediction that phase/frequency becomes abnormal for mildly damaged tissue (blue TDS), grows with the level of tissue injury and disappears for highly destroyed tissue (lesion core – red TDS). Dark areas on the GEPCI frequency map might correspond to predominantly axonal damage while bright areas – to predominantly myelin damage.

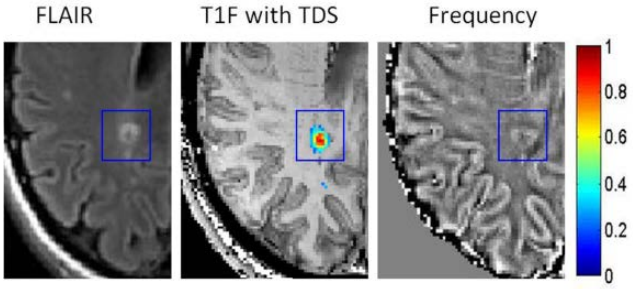

Figure 6.4 Example of a MS lesion (marked by a red rectangle) that has a range of TDS represented by colors on vertical bar. TDS is overlaid on T1f image. Data obtained from a subject with RRMS (female, age 42, EDSS 2.0).

Examples of changes in phase image in MS lesions with no or very small TDS scores are shown in Figure 6.5, orange and blue rectangles. These might represent changes in tissue microstructure that are not observed with conventional imaging techniques. The positive phase contrast indicates myelin damage.

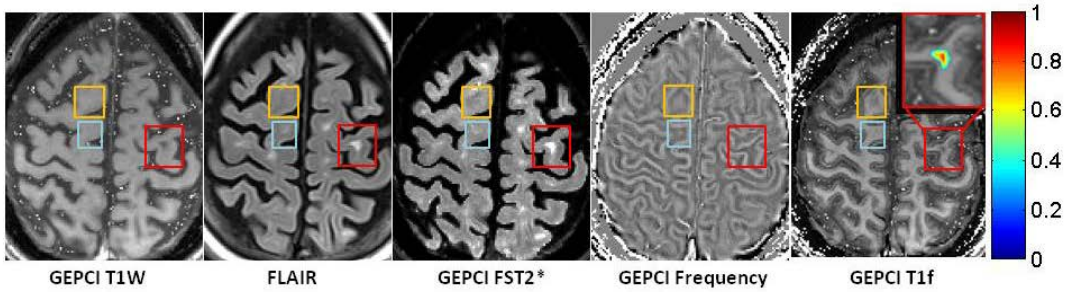

Figure 6.5 Example of data obtained from a subject with SPMS (female, age 49, EDSS 6.5). Note the prominent contrast between GM and WM on GEPCI T1f image as compared to other images. Rectangles outline abnormalities observed on FLAIR or Frequency (phase) maps. Orange rectangles denote an alteration seen in phase images (bright contrast) but not on T1W, FLAIR or GEPCI FST2*. This may represent a very mild lesion with damaged myelin, and is also seen on GEPCI T1f image as negative dark contrast. Blue rectangle outlines a small MS lesion that is barely seen on FLAIR and GEPCI FST2*, and is also visible on the phase image. Red rectangle outlines a severe MS lesion (very high TDS score) that is seen on T1W, FLAIR and GEPCI FST2* but does not have a footprint on the phase image. A magnified view of this lesion is shown in the inset (upper right of GEPCI T1f image) with overlaid GEPCI TDS score in color according to the color bar.

According to Figure 6.1 and Figure 6.3, the phase contrast in severe lesions (black holes, high TDS score) can disappear even though these lesions would have substantially different magnetic susceptibility from the surrounding normal WM. Example of such a lesion is shown in Figure 6.5, red rectangle. The absence of phase contrast together with high TDS in this case suggests that myelin and axonal debris are mostly removed from the lesion area.

Lesions of intermediate severity (intermediate GEPCI TDS score) appear on – GEPCI T1W (hypointense), FLAIR and GEPCI FST2* (hyperintense) and Phase/frequency maps. Several examples are shown in Figure 6.6, red rectangles. The combination of TDS and phase appearance suggests that myelin is damaged but with myelin debris still present in the lesion area. At the same time the lesion denoted by an orange oval has

similar TDS but very little phase contrast, suggesting damage to both myelin and axon that offset one another.

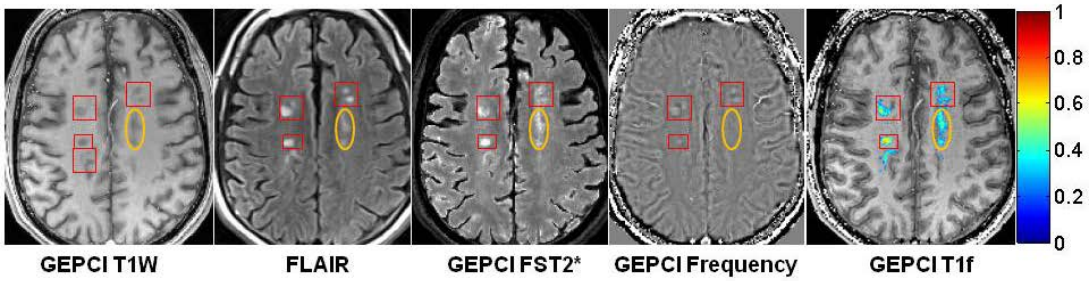

Figure 6.6 Example of data obtained from a subject with RRMS (male, age 52, EDSS 3.5) showing multiple lesions (red rectangles) with intermediate TDS scores (overlaid on GEPCI T1f image). Here, lesions seen on FLAIR are also seen on GEPCI T1W, GEPCI FST2* (GEPCI analog of FLAIR) and GEPCI Frequency map. Area within orange oval also corresponds to intermediate TDS with low phase contrast.

The theory of MS lesion manifestations on phase/frequency images proposed herein should be complemented by considerations of lesion shape, not only the internal lesion structure. Development of lesions of varying severity might lead to multiple appearances on phase images, because phase is a combination of multiple factors that include not only the change in tissue content and structure but also the shape and the structure of the surrounding tissue. One potential approach to overcoming this problem is Quantitative Susceptibility Mapping (QSM) (123,125-127,146), where non-local effects of magnetic fields on phase image are removed by solving Maxwell equations for field distribution on a global level. The current state of this approach however assumes that MR signal phase relates to tissue magnetic susceptibility by means of a Lorentzian sphere approximation which is not the case for WM in general, and MS lesions in particular, as shown in the present study. Thus, QSM technique, as a tool for analyzing

WM structure and MS lesions, awaits incorporation of a non-spherical Lorentzian relationship between MR signal phase and local magnetic field.

In this chapter we focus our attention on the most pronounced injuries to tissue in MS - myelin and axonal damage. Other components of the MS lesion, e.g. inflammatory cell infiltration, gliosis, and edema/increased extracellular space can also be incorporated in our model. These will be a subject of our future research. Other hypotheses of phase contrast that were also discussed previously include frequency shifts induced by water-macromolecule exchange in the tissue (42,55,56) and possible tissue magnetic susceptibility dependence upon orientation with respect to the magnetic field B_0 (58,154), though their roles are not yet clear.

6.4 Summary

In this study we propose a theory of phase contrast in MS and provide experimental and Monte-Carlo simulated results supporting our theoretical predictions. Our theory is based on the newly introduced concept - Generalized Lorentzian Approach – that allows relating MRI signal phase not to tissue bulk magnetic susceptibility but to tissue "magnetic architecture," the distribution of magnetic susceptibility inclusions (lipids, proteins, iron, etc) at the cellular and sub cellular levels (144). Our theory predicts that the phase contrast in MS lesions could appear due to MS pathology affecting white matter integrity, such as mild injury to the myelin sheath or neurofilaments, even with preserved tissue magnetic susceptibility. Also, contrary to an expectation that the phase contrast in MS lesions should always increase in magnitude with lesion worsening (as

happens for all known MR magnitude imaging contrast mechanisms), our theory and experimental results indicate that phase contrast can actually disappear with extreme tissue destruction. We also demonstrate that the change in the phase contrast might be specific to a type of tissue injury – myelin (positive change) vs. neurofilaments (negative change). The GEPCI approach, providing simultaneous information on tissue signal phase, T2* and T1, shows unique potential to decipher the mechanisms underlying phase contrast. Our approach not only aids in understanding changes seen by phase imaging, but opens a door to better understanding biological underpinnings of MS brain pathology and has a potential to assist in optimizing design of clinical trials.

Chapter 7 Conclusions and Future Directions

In this study, we extensively investigated the mechanisms behind gradient echo MRI signal formation, and explored the use of gradient echo MRI in Multiple Sclerosis. The origin and use of phase contrast have become hot topics of investigation in the field of MRI in recent years since it manifests superior gray matter/ white matter contrast and sub-cortical contrast. By measurement of phase contrast in isolated optic nerve, we have provided the first direct prove of the theoretical framework – Generalized Lorentzian Approach – developed in our group. The experiment shows that phase contrast in brain white matter (optic nerve) is not directly proportional to the tissue bulk magnetic susceptibility but is rather determined by the geometrical arrangement of brain tissue components (lipids, proteins, iron, etc.) at the cellular and sub-cellular levels. We have also provided first quantitative measurements of the contribution to phase contrast from the water-macromolecule exchange effect. Based on our measurement in protein solutions, we demonstrated that the magnitude of the exchange effect is 1/2 of susceptibility effect and to the opposite sign. Further we apply the Generalized Lorentzian Approach to better understand phase contrasts in MS lesions.

In most of our studies we used Gradient Echo Plural Contrast Imaging (GEPCI) technique developed in our laboratory. It is based on multi-gradient-echo sequence, and allows generating of several base and secondary contrasts. Basic contrasts include T2* relaxation time constant maps, T1-weighted signal intensity images and signal phase/frequency maps. Secondary contrast images include SWI, T1f, FST2* and T2*-SWI. All these base and secondary GEPCI images with multiple novel contrasts provide

additional information that helps with visualization and identification of brain abnormalities including MS.

By using GEPCI quantitative T2* maps we have developed a scoring method for monitoring Multiple Sclerosis. With a cohort of 30 MS subjects (10 in each MS subtypes), we demonstrated a strong agreement between GEPCI quantitative scores and traditional lesion load assessment. We also established a correlation between GEPCI scores and clinical tests for MS patients. We found that this correlation is stronger than that found between traditional lesion load and clinical tests. We have also demonstrated the ability of GEPCI scores to distinguish between MS subtypes.

Of course, there are much more in these topics that one can carry on investigating.

1) MS disease. As a CNS disease, the pathology of MS is not restricted in the brain, but also cerebellum, brain stem, and spinal cord; GEPCI measurement should be performed on more parts of the CNS in order to reflect more closely to the patients' clinical status. As demonstrated in our preliminary results (Chapter 5), we have already started in the direction of spinal cord imaging using GEPCI. Moreover, the cortical damage is also a very important aspect in evaluating CNS damage, and remains to be investigated.
2) The GEPCI study needs to be taken to a bigger population in order to allow stronger statistical power to confirm our preliminary results. Age matched control subjects are also needed so that we could rule out variations in T2* due to age.
3) Brain atrophy can be added in GEPCI scores as another dimension of abnormality measurement. It is especially suitable for monitoring longitudinal changes of MS

subjects under treatment (useful in evaluation of clinical trials).

4) Along the road of using phase contrast in explaining MS lesions in brain white matter (Chapter 6), it will be important to have histological validation of our theory. Correlations between pathological hallmarks and MR signal from *ex vivo* tissue have been found on T1 and T2 before, and a similar experiment should offer a fairly direct experimental evidence for origin of phase contrast. However, our data (Chapter 2, and abstract) show that both magnitude and phase contrast could be very different from *in vivo* to formalin fixed tissue – which limits the adequacy of histological validation. Using animal model *in vivo* could be a promising solution to this problem. Marmoset is a good candidate; given it has big WM volume.

5) From technical aspects: to improve GEPCI, one ongoing effort in our group is the field inhomogeneity correction. Since the quantitative measurement of T2* is actually susceptible to macroscopic magnetic field inhomogeneity, we always perform careful shimming on the field before experiments. However, there are some intrinsic sources of field distortion associated with the brain geometry such as sinuses and ear canals. A theoretical way to remove field inhomogeneity is under development in our group.

   Finally, we treated the gradient echo signal as single compartment throughout the study, that is we assume the tissue water is uniform in each voxel. In fact, the tissue water distribution is usually more complicated, and has multiple slow exchanging or non-exchanging components. Each of them has their own relaxation characteristics, and their own frequency. The role of multi-compartment model in phase contrast between gray and white matter; and new insights on relationship between MRI signal and specific disease pathologies of MS remain to be future directions of our study.

References

1. Levitt M. Spin Dynamics: Basics of Nuclear Magnetic Resonance. West Sussex, England: John Wiley & Sons, Ltd; 2001.
2. Bernstein MA, King KF, Zhou XJ. Handbook of MRI pulse sequences: Academic Press; 2004.
3. Duyn JH, van Gelderen P, Li TQ, de Zwart JA, Koretsky AP, Fukunaga M. High-field MRI of brain cortical substructure based on signal phase. Proceedings of the National Academy of Sciences of the United States of America 2007;104(28):11796-11801.
4. Compston A, Coles A. Multiple sclerosis. Lancet 2008;372(9648):1502-1517.
5. Lublin FD, Reingold SC. Defining the clinical course of multiple sclerosis: Results of an international survey. Neurology 1996;46(4):907-911.
6. Miller DH, Leary SM. Primary-progressive multiple sclerosis. Lancet Neurology 2007;6(10):903-912.
7. Kurtzke JF. Rating Neurologic Impairment in Multiple-Sclerosis - an Expanded Disability Status Scale (Edss). Neurology 1983;33(11):1444-1452.
8. Minagar A, Jy W, Jimenez JJ, Alexander JS. Multiple sclerosis as a vascular disease. Neurological Research 2006;28(3):230-235.
9. Bjartmar C, Wujek JR, Trapp BD. Axonal loss in the pathology of MS: consequences for understanding the progressive phase of the disease. Journal of the Neurological Sciences 2003;206(2):165-171.
10. Trapp BD, Peterson J, Ransohoff RM, Rudick R, Mork S, Bo L. Axonal transection in the lesions of multiple sclerosis. New England Journal of Medicine 1998;338(5):278-285.
11. Mainero C, De Stefano N, Iannucci G, Sormani MP, Guidi L, Federico A, Bartolozzi ML, Comi G, Filippi M. Correlates of MS disability assessed in vivo using aggregates of MR quantities. Neurology 2001;56(10):1331-1334.
12. Goodin D. The use of MRI in the diagnosis of multiple sclerosis. Lancet Neurol 2006;5(10):808-809.
13. Goodin DS. Magnetic resonance imaging as a surrogate outcome measure of disability in multiple sclerosis: have we been overly harsh in our assessment? Ann Neurol 2006;59(4):597-605.
14. Goodkin DE, Rooney WD, Sloan R, Bacchetti P, Gee L, Vermathen M, Waubant E, Abundo M, Majumdar S, Nelson S, Weiner MW. A serial study of new MS lesions and the white matter from which they arise. Neurology 1998;51(6):1689-1697.
15. Li DKB, Held U, Petkau J, Daumer M, Barkhof F, Fazekas F, Frank JA, Kappos L, Miller DH, Simon JH, Wolinsky JS, Filippi M. MRI T2 lesion burden in multiple sclerosis - A plateauing relationship with clinical disability. Neurology 2006;66(9):1384-1389.
16. Sormani MP, Rovaris M, Comi G, Filippi M. A reassessment of the plateauing relationship between T2 lesion load and disability in MS. Neurology 2009;73(19):1538-1542.
17. Sormani MP, Bruzzi P, Beckmann K, Wagner K, Miller DH, Kappos L, Filippi M. MRI metrics as surrogate endpoints for EDSS progression in SPMS patients treated with IFN beta-lb. Neurology 2003;60(9):1462-1466.
18. van Walderveen MAA, Lycklama a Nijeholt GJ, Ader HJ, Jongen PJH, Polman CH, Castelijns JA, Barkhof F. Hypointense lesions on T1-weighted spin-echo

magnetic resonance imaging - Relation to clinical characteristics in subgroups of patients with multiple sclerosis. Archives of Neurology 2001;58(1):76-81.
19. Balaban RS, Ceckler TL. Magnetization transfer contrast in magnetic resonance imaging. Magnetic Resonance Quarterly 1992;8(2):116-137.
20. Wolff SD, Balaban RS. Magnetization Transfer Contrast (Mtc) and Tissue Water Proton Relaxation Invivo. Magnetic Resonance in Medicine 1989;10(1):135-144.
21. Filippi M, Inglese M, Rovaris M, Sormani MP, Horsfield MA, Iannucci G, Colombo B, Comi G. Magnetization transfer imaging to monitor the evolution of MS - A 1-year follow-up study. Neurology 2000;55(7):940-946.
22. Pike GB, De Stefano N, Narayanan S, Worsley KJ, Pelletier D, Francis GS, Antel JP, Arnold DL. Multiple sclerosis: Magnetization transfer MR imaging of white matter before lesion appearance on T2-weighted images. Radiology 2000;215(3):824-830.
23. Gass A, Barker GJ, Kidd D, Thorpe JW, Macmanus D, Brennan A, Tofts PS, Thompson AJ, Mcdonald WI, Miller DH. Correlation of Magnetization-Transfer Ratio with Clinical Disability in Multiple-Sclerosis. Annals of Neurology 1994;36(1):62-67.
24. van der Knaap MS, Valk J. Chapter 1: Myelin and white matter. Magnetic resonance of myelination and myelin disorders. 3rd edition: New York : Springer; 2005. page 7 p.
25. Miller DH, Austin SJ, Connelly A, Youl BD, Gadian DG, Mcdonald WI. Proton Magnetic-Resonance Spectroscopy of an Acute and Chronic Lesion in Multiple-Sclerosis. Lancet 1991;337(8732):58-59.
26. Suhy J, Rooney WD, Goodkin DE, Capizzano AA, Soher BJ, Maudsley AA, Waubant E, Andersson PB, Weiner MW. H-1 MRSI comparison of white matter and lesions in primary progressive and relapsing-remitting MS. Multiple Sclerosis Journal 2000;6(3):148-155.
27. Tourbah A, Stievenart JL, Gout O, Fontaine B, Liblau R, Lubetzki C, Cabanis EA, Lyon-Caen O. Localized proton magnetic resonance spectroscopy in relapsing remitting versus secondary progressive multiple sclerosis. Neurology 1999;53(5):1091-1097.
28. DeStefano N, Matthews PM, Narayanan S, Francis GS, Antel JP, Arnold DL. Axonal dysfunction and disability in a relapse of multiple sclerosis: Longitudinal study of a patient. Neurology 1997;49(4):1138-1141.
29. Gonen O, Catalaa I, Babb JS, Ge Y, Mannon LJ, Kolson DL, Grossman RI. Total brain N-acetylaspartate - A new measure of disease load in MS. Neurology 2000;54(1):15-19.
30. Le Bihan D, Breton E, Lallemand D, Grenier P, Cabanis E, Lavaljeantet M. MR Imaging of Intravoxel Incoherent Motions - Application to Diffusion and Perfusion in Neurologic Disorders. Radiology 1986;161(2):401-407.
31. Song SK, Sun SW, Ramsbottom MJ, Chang C, Russell J, Cross AH. Dysmyelination revealed through MRI as increased radial (but unchanged axial) diffusion of water. Neuroimage 2002;17(3):1429-1436.
32. Sun SW, Liang HF, Cross AH, Song SK. Evolving Wallerian degeneration after transient retinal ischemia in mice characterized by diffusion tensor imaging. Neuroimage 2008;40(1):1-10.
33. Sun SW, Liang HF, Schmidt RE, Cross AH, Song SK. Selective vulnerability of cerebral white matter in a murine model of multiple sclerosis detected using diffusion tensor imaging. Neurobiol Dis 2007;28(1):30-38.

34. Song SK, Sun SW, Ju WK, Lin SJ, Cross AH, Neufeld AH. Diffusion tensor imaging detects and differentiates axon and myelin degeneration in mouse optic nerve after retinal ischemia. Neuroimage 2003;20(3):1714-1722.
35. Budde MD, Kim JH, Liang HF, Russell JH, Cross AH, Song SK. Axonal injury detected by in vivo diffusion tensor imaging correlates with neurological disability in a mouse model of multiple sclerosis. Nmr in Biomedicine 2008;21(6):589-597.
36. van Waesberghe JHTM, Kamphorst W, De Groot CJA, van Walderveen MAA, Castelijns JA, Ravid R, Nijeholt GJLA, van der Valk P, Polman CH, Thompson AJ, Barkhof F. Axonal loss in multiple sclerosis lesions: Magnetic resonance imaging insights into substrates of disability. Annals of Neurology 1999;46(5):747-754.
37. Papanikolaou N, Papadaki E, Karampekios S, Spilioti M, Maris T, Prassopoulos P, Gourtsoyiannis N. T2 relaxation time analysis in patients with multiple sclerosis: correlation with magnetization transfer ratio. European Radiology 2004;14(1):115-122.
38. Seewann A, Vrenken H, van der Valk P, Blezer ELA, Knol DL, Castelijns JA, Polman CH, Pouwels PJW, Barkhof F, Geurts JJG. Diffusely Abnormal White Matter in Chronic Multiple Sclerosis Imaging and Histopathologic Analysis. Archives of Neurology 2009;66(5):601-609.
39. Luo J, Jagadeesan BD, Cross AH, Yablonskiy DA. Gradient Echo Plural Contrast Imaging - Signal model and derived contrasts: T2*, T1, Phase, SWI, T1f, FST2*and T2*-SWI. Neuroimage 2012;60(2):1073-1082.
40. Sati P, Cross AH, Luo J, Hildebolt CF, Yablonskiy DA. In vivo quantitative evaluation of brain tissue damage in multiple sclerosis using gradient echo plural contrast imaging technique. Neuroimage 2010;51(3):1089-1097.
41. Yablonskiy DA. Gradient echo plural contrast imaging (GEPCI) - New fast magnetic resonance imaging technique for simultaneous acquisition of T2, T1 (or spin density) and T2*-weighted images. Radiology 2000;217:204-204.
42. Zhong K, Leupold J, von Elverfeldt D, Speck O. The molecular basis for gray and white matter contrast in phase imaging. Neuroimage 2008;40(4):1561-1566.
43. Marques JP, Maddage R, Mlynarik V, Gruetter R. On the origin of the MR image phase contrast: An in vivo MR microscopy study of the rat brain at 14.1 T. Neuroimage 2009;46(2):345-352.
44. Abduljalil AM, Schmalbrock P, Novak V, Chakeres DW. Enhanced gray and white matter contrast of phase susceptibility-weighted images in ultra-high-field magnetic resonance imaging. J Magn Reson Imaging 2003;18(3):284-290.
45. Rauscher A, Sedlacik J, Barth M, Mentzel HJ, Reichenbach JR. Magnetic susceptibility-weighted MR phase imaging of the human brain. AJNR Am J Neuroradiol 2005;26(4):736-742.
46. Kutzelnigg A, Lucchinetti CF, Stadelmann C, Bruck W, Rauschka H, Bergmann M, Schmidbauer M, Parisi JE, Lassmann H. Cortical demyelination and diffuse white matter injury in multiple sclerosis. Brain 2005;128:2705-2712.
47. Hammond KE, Metcalf M, Carvajal L, Okuda DT, Srinivasan R, Vigneron D, Nelson SJ, Pelletier D. Quantitative In Vivo Magnetic Resonance Imaging of Multiple Sclerosis at 7 Tesla with Sensitivity to Iron. Annals of Neurology 2008;64(6):707-713.
48. Fukunaga M, Li TQ, van Gelderen P, de Zwart JA, Shmueli K, Yao B, Lee J, Maric D, Aronova MA, Zhang GF, Leapman RD, Schenck JF, Merkle H, Duyn JH. Layer-specific variation of iron content in cerebral cortex as a source of MRI contrast. Proceedings of the National Academy of Sciences of the United States of America 2010;107(8):3834-3839.

49. Yao B, Li TQ, van Gelderen P, Shmueli K, de Zwart JA, Duyn JH. Susceptibility contrast in high field MRI of human brain as a function of tissue iron content. Neuroimage 2009;44(4):1259-1266.
50. Lee J, Hirano Y, Fukunaga M, Silva AC, Duyn JH. On the contribution of deoxy-hemoglobin to MRI gray-white matter phase contrast at high field. Neuroimage 2010;49(1):193-198.
51. Petridou N, Wharton SJ, Lotfipour A, Gowland P, Bowtell R. Investigating the effect of blood susceptibility on phase contrast in the human brain. Neuroimage 2010;50(2):491-498.
52. He X, Zhu M, Yablonskiy DA. Validation of Oxygen Extraction Fraction Measurement by qBOLD Technique. Magn Reson Med 2008;Accepted.
53. Spees WM, Yablonskiy DA, Oswood MC, Ackerman JJ. Water proton MR properties of human blood at 1.5 Tesla: magnetic susceptibility, T(1), T(2), T*(2), and non-Lorentzian signal behavior. Magn Reson Med 2001;45(4):533-542.
54. Lodygensky GA, Marques JP, Maddage R, Perroud E, Sizonenko SV, Huppi PS, Gruetter R. In vivo assessment of myelination by phase imaging at high magnetic field. Neuroimage 2012;59(3):1979-1987.
55. Luo J, He X, d'Avignon DA, Ackerman JJH, Yablonskiy DA. Protein-induced water H-1 MR frequency shifts: Contributions from magnetic susceptibility and exchange effects. Journal of Magnetic Resonance 2010;202(1):102-108.
56. Shmueli K, Dodd SJ, Li TQ, Duyn JH. The Contribution of Chemical Exchange to MRI Frequency Shifts in Brain Tissue. Magnetic Resonance in Medicine 2011;65(1):35-43.
57. Lee J, van Gelderen P, Kuo LW, Merkle H, Silva AC, Duyn JH. T(2)*-based fiber orientation mapping. Neuroimage 2011;57(1):225-234.
58. Liu CL. Susceptibility Tensor Imaging. Magnetic Resonance in Medicine 2010;63(6):1471-1477.
59. Liu CL, Li W, Johnson GA, Wu B. High-field (9.4 T) MRI of brain dysmyelination by quantitative mapping of magnetic susceptibility. Neuroimage 2011;56(3):930-938.
60. Langkammer C, Krebs N, Goessler W, Scheurer E, Yen K, Fazekas F, Ropele S. Susceptibility induced gray-white matter MRI contrast in the human brain. Neuroimage 2012;59(2):1413-1419.
61. He X, Yablonskiy DA. Biophysical mechanisms of phase contrast in gradient echo MRI. Proceedings of the National Academy of Sciences of the United States of America 2009;106(32):13558-13563.
62. Chu SC, Xu Y, Balschi JA, Springer CS. Bulk magnetic susceptibility shifts in NMR studies of compartmentalized samples: use of paramagnetic reagents. Magnetic Resonance in Medicine 1990;13(2):239-262.
63. Dahnke H, Schaeffter T. Limits of detection of SPIO at 3.0 T using T-2* relaxometry. Magnetic Resonance in Medicine 2005;53(5):1202-1206.
64. He X, Yablonskiy DA. Quantitative BOLD: Mapping of human cerebral deoxygenated blood volume and oxygen extraction fraction: Default state. Magnetic Resonance in Medicine 2007;57(1):115-126.
65. Sati P, van Gelderen P, Silva AC, Merkle H, Reich DS, Duyn JH. Evidence of the myelin origin of the short T2* component in white matter: a combined magnetization transfer and T2* relaxometry experiment in the marmoset brain at 7T. Proceedings of the 20th International Society for Magnetic Resonance in Medicine 2012:019.
66. Wharton SJ, Bowtell R. Non-linear Phase Evolution: The Dominant Source of the Average Frequency Difference between Grey Matter and White Matter in

Gradient Echo MRI? Proceedings of the 20th International Society for Magnetic Resonance in Medicine 2012:380.
67. Hammond KE, Metcalf M, Okuda DT, Nelson SJ, Vigneron DB, Pelletier D. In vivo high resolution MR imaging at 7T of multiple sclerosis with sensitivity to iron. Neurology 2008;70(11):A8-a8.
68. Ding B, Chen KM, Ling HW, Sun F, Li X, Wan T, Chai WM, Zhang H, Zhan Y, Guan YJ. Correlation of Iron in the Hippocampus with MMSE in Patients with Alzheimer's Disease. Journal of Magnetic Resonance Imaging 2009;29(4):793-798.
69. Haacke EM, Cheng NY, House MJ, Liu Q, Neelavalli J, Ogg RJ, Khan A, Ayaz M, Kirsch W, Obenaus A. Imaging iron stores in the brain using magnetic resonance imaging. Magn Reson Imaging 2005;23(1):1-25.
70. Schenck JF, Zimmerman EA. High-field magnetic resonance imaging of brain iron: birth of a biomarker? Nmr in Biomedicine 2004;17(7):433-445.
71. Schenck JF. Magnetic resonance imaging of brain iron. Journal of the Neurological Sciences 2003;207(1-2):99-102.
72. Yablonskiy DA, Haacke EM. Theory of NMR Signal Behavior in Magnetically Inhomogeneous Tissues - the Static Dephasing Regime. Magnetic Resonance in Medicine 1994;32(6):749-763.
73. He X, Zhu M, Yablonskiy DA. Validation of oxygen extraction fraction measurement by qBOLD technique. Magnetic Resonance in Medicine 2008;60(4):882-888.
74. He X, Yablonskiy DA. On the Nature of Phase Contrast in Gradient Echo MRI:A Generalized Lorentzian Approach. Proc Intl Soc Mag Reson Med 2009;17.
75. Bryant RG. The dynamics of water-protein interactions. Annu Rev Biophys Biomol Struct 1996;25:29-53.
76. Mäkelä HI, Gröhn OHJ, Kettunen MI, Kauppinen RA. Proton Exchange as a Relaxation Mechanism for T1 in the Rotating Frame in Native and Immobilized Protein Solutions. Biochemical and Biophysical Research Communications 2001;289(4):813-818.
77. Liepinsh E, Otting G. Proton exchange rates from amino acid side chains - Implications for image contrast. Magnetic Resonance in Medicine 1996;35(1):30-42.
78. Olechnowicz R, Masierak W, Bodurka J, Gutsze A. ^{1}H NMR relaxation measurements in highly concentrated water protein solutions. Magnetic Resonance in Chemistry 1999;37(13):S147-S149.
79. Hills BP, Takacs SF, Belton PS. The effects of proteins on the proton N.M.R. transverse relaxation times of water -- I. Native bovine serum albumin. Molecular Physics: An International Journal at the Interface Between Chemistry and Physics 1989;67(4):903 - 918.
80. Ravel R. Chapter 19. Cerebrospinal Fluid Examination and Neurologic Disorders. Clinical laboratory medicine: clinical application of laboratory data. 6th edition. Elsevier Health Sciences 1994:page 295.
81. Shimizu A, Ikeguchi M, Sugai S. Appropriateness of DSS and TSP as internal references for ^{1}H NMR studies of molten globule proteins in aqueous media Journal of Biomolecular NMR 1994;4(6):859-862.
82. Quirk JD, Sukstanskii AL, Bretthorst GL, Yablonskiy DA. Optimal decay rate constant estimates from phased array data utilizing joint Bayesian analysis. Journal of Magnetic Resonance 2009;198(1):49-56.

83. Gallier J, Rivet P, de Certaines J. 1H- and 2H-NMR study of bovine serum albumin solutions. Biochimica et Biophysica Acta (BBA) - Protein Structure and Molecular Enzymology 1987;915(1):1-18.
84. Bretthorst GL. Bayesian Spectrum Analysis and Parameter Estimation. Berlin: Springer-Verlag; 1988.
85. Hindman JC. Proton Resonance Shift of Water in the Gas and Liquid States. The Journal of Chemical Physics 1966;44(12):4582-4592.
86. Weast RC, Astle MC. CRC handbook of chemistry and physics. Cleveland, Ohio: CRC Press; 1981-1982.
87. Woodward CK, Ellis LM, Rosenberg A. Solvent accessibility in folded proteins. Studies of hydrogen exchange in trypsin. J Biol Chem 1975;250(2):432-439.
88. Srere PA. Macromolecular interactions: tracing the roots. Trends Biochem Sci 2000;25(3):150-153.
89. Kiyota K. Soluble protein fraction of the brain tissue in relation to maturation of the brain. Folia Psychiatr Neurol Jpn 1959;13:15-22.
90. Schmitt FO. Fibrous proteins--neuronal organelles. Proceedings of the National Academy of Sciences of the United States of America 1968;60(4):1092-1101.
91. Mizuno K, Imafuji S, Fujiwara T, Ohta T, Tamiya Y. Hydration of the CH groups in 1,4-dioxane probed by NMR and IR: Contribution of blue-shifting CH center dot center dot center dot OH2 hydrogen bonds. J Phys Chem B 2003;107(16):3972-3978.
92. Chick H, Martin CJ. The Density and Solution Volume of some Proteins. Biochem J 1913;7(1):92-96.
93. Cerdonio M, Morante S, Torresani D, Vitale S, DeYoung A, Noble RW. Reexamination of the evidence for paramagnetism in oxy- and carbonmonoxyhemoglobins. Proc Natl Acad Sci U S A 1985;82(1):102-103.
94. Spector AA, John K, Fletcher JE. Binding of long-chain fatty acids to bovine serum albumin. J Lipid Res 1969;10(1):56-67.
95. Cistola DP, Small DM, Hamilton JA. Carbon 13 NMR studies of saturated fatty acids bound to bovine serum albumin. I. The filling of individual fatty acid binding sites. J Biol Chem 1987;262(23):10971-10979.
96. Witoszynskyj S, Rauscher A, Reichenbach JR, Barth M. Phase unwrapping of MR images using Phi UN - A fast and robust region growing algorithm. Medical Image Analysis 2009;13(2):257-268.
97. Hammond KE, Lupo JM, Xu D, Metcalf M, Kelley DAC, Pelletier D, Chang SM, Mukherjee P, Vigneron DB, Nelson SJ. Development of a robust method for generating 7.0 T multichannel phase images of the brain with application to normal volunteers and patients with neurological diseases. Neuroimage 2008;39(4):1682-1692.
98. Schweser F, Deistung A, Lehr BW, Reichenbach JR. Quantitative imaging of intrinsic magnetic tissue properties using MRI signal phase: An approach to in vivo brain iron metabolism? Neuroimage 2011;54(4):2789-2807.
99. Liu T, Khalidov I, de Rochefort L, Spincemaille P, Liu J, Tsiouris AJ, Wang Y. A novel background field removal method for MRI using projection onto dipole fields (PDF). Nmr in Biomedicine 2011;24(9):1129-1136.
100. Reichenbach JR, Venkatesan R, Schillinger DJ, Kido DK, Haacke EM. Small vessels in the human brain: MR venography with deoxyhemoglobin as an intrinsic contrast agent. Radiology 1997;204(1):272-277.
101. Hajnal JV, Bryant DJ, Kasuboski L, Pattany PM, Decoene B, Lewis PD, Pennock JM, Oatridge A, Young IR, Bydder GM. Use of Fluid Attenuated Inversion

Recovery (Flair) Pulse Sequences in Mri of the Brain. Journal of Computer Assisted Tomography 1992;16(6):841-844.
102. Smith SM, Jenkinson M, Woolrich MW, Beckmann CF, Behrens TEJ, Johansen-Berg H, Bannister PR, De Luca M, Drobnjak I, Flitney DE, Niazy RK, Saunders J, Vickers J, Zhang YY, De Stefano N, Brady JM, Matthews PM. Advances in functional and structural MR image analysis and implementation as FSL. Neuroimage 2004;23:S208-S219.
103. Woolrich MW, Jbabdi S, Patenaude B, Chappell M, Makni S, Behrens T, Beckmann C, Jenkinson M, Smith SM. Bayesian analysis of neuroimaging data in FSL. Neuroimage 2009;45(1):S173-S186.
104. Zhang YY, Brady M, Smith S. Segmentation of brain MR images through a hidden Markov random field model and the expectation-maximization algorithm. Ieee Transactions on Medical Imaging 2001;20(1):45-57.
105. Grabner G, Dal-Bianco A, Schernthaner M, Vass K, Lassmann H, Trattnig S. Analysis of Multiple Sclerosis Lesions Using a Fusion of 3.0 T FLAIR and 7.0 T SWI Phase: FLAIR SWI. Journal of Magnetic Resonance Imaging 2011;33(3):543-549.
106. Denk C, Rauscher A. Susceptibility Weighted Imaging With Multiple Echoes. Journal of Magnetic Resonance Imaging 2010;31(1):185-191.
107. Haacke EM, Mittal S, Wu Z, Neelavalli J, Cheng YCN. Susceptibility-Weighted Imaging: Technical Aspects and Clinical Applications, Part 1. American Journal of Neuroradiology 2009;30(1):19-30.
108. JMP®10. Modeling and Multivariate Methods. Cary, North Carolina: SAS Institute Inc.; 2012.
109. Binder DK, Rau G, Starr PA. Hemorrhagic complications of microelectrode-guided deep brain stimulation. Stereotactic and Functional Neurosurgery 2003;80(1-4):28-31.
110. Kanekar S, Gent M. Malformations of cortical development. Semin Ultrasound CT MR 2011;32(3):211-227.
111. Pirko I, Lucchinetti CF, Sriram S, Bakshi R. Gray matter involvement in multiple sclerosis. Neurology 2007;68(9):634-642.
112. He X, Yablonskiy DA. Quantitative BOLD: mapping of human cerebral deoxygenated blood volume and oxygen extraction fraction: default state. Magn Reson Med 2007;57(1):115-126.
113. Keegan BM, Noseworthy JH. Multiple sclerosis. Annual Review of Medicine 2002;53:285-302.
114. McFarland HF. Examination of the role of magnetic resonance imaging in multiple sclerosis: A problem-orientated approach. Annals of Indian Academy of Neurology 2009;12(4):254-263.
115. Haacke EM, Makki M, Ge YL, Maheshwari M, Sehgal V, Hu JN, Selvan M, Wu Z, Latif Z, Xuan Y, Khan O, Garbern J, Grossman RI. Characterizing Iron Deposition in Multiple Sclerosis Lesions Using Susceptibility Weighted Imaging. Journal of Magnetic Resonance Imaging 2009;29(3):537-544.
116. Reishofer G, Fazekas F, Keeling S, Enzinger C, Payer F, Simbrunner J, Stollberger R. Minimizing macrovessel signal in cerebral perfusion imaging using independent component analysis. Magnetic Resonance in Medicine 2007;57(2):278-288.
117. Maciunas JA, Syed TU, Cohen ML, Werz MA, Maciunas RJ, Koubeissi MZ. Triple pathology in epilepsy: Coexistence of cavernous angiomas and cortical dysplasias with other lesions. Epilepsy Research 2010;91(1):106-110.

118. Menzler K, Thiel P, Hermsen A, Chen X, Benes L, Miller D, Sure U, Knake S, Rosenow F. The role of underlying structural cause for epilepsy classification: Clinical features and prognosis in mesial temporal lobe epilepsy caused by hippocampal sclerosis versus cavernoma. Epilepsia 2011;52(4):707-711.
119. Barkovich AJ. Abnormal Vascular Drainage in Anomalies of Neuronal Migration. American Journal of Neuroradiology 1988;9(5):939-942.
120. Desai K, Bhayani R, Nadkarni T, Limaye U, Goel A. Developmental deep venous system anomaly associated with congenital malformation of the brain. Pediatric Neurosurgery 2002;36(1):37-39.
121. Fernandez-Seara MA, Wehrli FW. Postprocessing technique to correct for background gradients in image-based R-2(*) measurements. Magnetic Resonance in Medicine 2000;44(3):358-366.
122. Yablonskiy DA. Quantitation of intrinsic magnetic susceptibility-related effects in a tissue matrix. Phantom study. Magnetic Resonance in Medicine 1998;39(3):417-428.
123. de Rochefort L, Brown R, Prince MR, Wang Y. Quantitative MR susceptibility mapping using piece-wise constant regularized inversion of the magnetic field. Magnetic Resonance in Medicine 2008;60(4):1003-1009.
124. Liu TA, Spincemaille P, de Rochefort L, Wong R, Prince M, Wang Y. Unambiguous identification of superparamagnetic iron oxide particles through quantitative susceptibility mapping of the nonlinear response to magnetic fields. Magnetic Resonance Imaging 2010;28(9):1383-1389.
125. Shmueli K, de Zwart JA, van Gelderen P, Li TQ, Dodd SJ, Duyn JH. Magnetic Susceptibility Mapping of Brain Tissue In Vivo Using MRI Phase Data. Magnetic Resonance in Medicine 2009;62(6):1510-1522.
126. Schweser F, Deistung A, Lehr BW, Reichenbach JR. Differentiation between diamagnetic and paramagnetic cerebral lesions based on magnetic susceptibility mapping. Medical Physics 2010;37(10):5165-5178.
127. de Rochefort L, Liu T, Kressler B, Liu J, Spincemaille P, Lebon V, Wu J, Wang Y. Quantitative susceptibility map reconstruction from MR phase data using bayesian regularization: validation and application to brain imaging. Magn Reson Med 2010;63(1):194-206.
128. Mackay A, Whittall K, Adler J, Li D, Paty D, Graeb D. In-Vivo Visualization of Myelin Water in Brain by Magnetic-Resonance. Magnetic Resonance in Medicine 1994;31(6):673-677.
129. Beaulieu C, Fenrich FR, Allen PS. Multicomponent water proton transverse relaxation and T-2-discriminated water diffusion in myelinated and nonmyelinated nerve. Magnetic Resonance Imaging 1998;16(10):1201-1210.
130. Lancaster JL, Andrews T, Hardies LJ, Dodd S, Fox PT. Three-pool model of white matter. Journal of Magnetic Resonance Imaging 2003;17(1):1-10.
131. Levesque IR, Pike GB. Characterizing Healthy and Diseased White Matter Using Quantitative Magnetization Transfer and Multicomponent T-2 Relaxometry: A Unified View via a Four-Pool Model. Magnetic Resonance in Medicine 2009;62(6):1487-1496.
132. Whittall KP, Mackay AL. Quantitative Interpretation of Nmr Relaxation Data. Journal of Magnetic Resonance 1989;84(1):134-152.
133. Du YP, Chu R, Hwang D, Brown MS, Kleinschmidt-DeMasters BK, Singel D, Simon JH. Fast multislice mapping of the myelin water fraction using multicompartment analysis of T-2* decay at 3T: A preliminary postmortem study. Magnetic Resonance in Medicine 2007;58(5):865-870.

134. Hwang D, Kim DH, Du YPP. In vivo multi-slice mapping of myelin water content using T-2* decay. Neuroimage 2010;52(1):198-204.
135. Roxburgh RHSR, Seaman SR, Masterman T, Hensiek AE, Sawcer SJ, Vukusic S, Achiti I, Confavreux C, Coustans M, le Page E, Edan G, McDonnell GV, Hawkins S, Trojano M, Liguori M, Cocco E, Marrosu MG, Tesser F, Leone MA, Weber A, Zipp F, Miterski B, Epplen JT, Oturai A, Sorensen PS, Celius EG, Lara NT, Montalban X, Villoslada P, Silva AM, Marta M, Leite I, Dubois B, Rubio J, Butzkueven H, Kilpatrick T, Mycko MP, Selmaj KW, Rio ME, Sa M, Salemi G, Savettieri G, Hillert J, Compston DAS. Multiple sclerosis severity score - Using disability and disease duration to rate disease severity. Neurology 2005;64(7):1144-1151.
136. Cutter GR, Baier ML, Rudick RA, Cookfair DL, Fischer JS, Petkau J, Syndulko K, Weinshenker BG, Antel JP, Confavreux C, Ellison GW, Lublin F, Miller AE, Rao SM, Reingold S, Thompson A, Willoughby E. Development of a multiple sclerosis functional composite as a clinical trial outcome measure. Brain 1999;122:871-882.
137. Fischer JS, Rudick RA, Cutter GR, Reingold SC. The Multiple Sclerosis Functional Composite measure (MSFC): an integrated approach to MS clinical outcome assessment. Multiple Sclerosis 1999;5(4):244-250.
138. Cohen JA, Reingold SC, Polman CH, Wolinsky JS. Disability outcome measures in multiple sclerosis clinical trials: current status and future prospects. Lancet Neurology 2012;11(5):467-476.
139. Fisher E, Chang A, Fox RJ, Tkach JA, Svarovsky T, Nakamura K, Rudick RA, Trapp BD. Imaging correlates of axonal swelling in chronic multiple sclerosis brains. Annals of Neurology 2007;62(3):219-228.
140. Hallgren B, Sourander P. The Effect of Age on the Non-Haemin Iron in the Human Brain. Journal of Neurochemistry 1958;3:41-51.
141. Lycklama G, Thompson A, Filippi M, Miller D, Polman C, Fazekas F, Barkhof F. Spinal-cord MRI in multiple sclerosis. Lancet Neurology 2003;2(9):555-562.
142. Geurts JJG, Pouwels PJW, Uitdehaag BMJ, Polman CH, Barkhof F, Castelijns JA. Intracortical lesions in multiple sclerosis: Improved detection with 3D double inversion-recovery MR imaging. Radiology 2005;236(1):254-260.
143. Mainero C, Benner T, Radding A, van der Kouwe A, Jensen R, Rosen BR, Kinkel RP. In vivo imaging of cortical pathology in multiple sclerosis using ultra-high field MRI. Neurology 2009;73(12):941-948.
144. He X, Yablonskiy DA. Biophysical mechanisms of phase contrast in gradient echo MRI. Proc Natl Acad Sci U S A 2009;106(32):13558-13563.
145. Fukunaga M, Li TQ, van Gelderen P, de Zwart JA, Shmueli K, Yao B, Lee J, Maric D, Aronova MA, Zhang G, Leapman RD, Schenck JF, Merkle H, Duyn JH. Layer-specific variation of iron content in cerebral cortex as a source of MRI contrast. Proc Natl Acad Sci U S A 2010;107(8):3834-3839.
146. Liu C, Li W, Johnson GA, Wu B. High-field (9.4 T) MRI of brain dysmyelination by quantitative mapping of magnetic susceptibility. Neuroimage 2011;56(3):930-938.
147. Pfefferbaum A, Adalsteinsson E, Rohlfing T, Sullivan EV. MRI estimates of brain iron concentration in normal aging: Comparison of field-dependent (FDRI) and phase (SWI) methods. Neuroimage 2009;47(2):493-500.
148. Hammond KE, Metcalf M, Carvajal L, Okuda DT, Srinivasan R, Vigneron D, Nelson SJ, Pelletier D. Quantitative in vivo magnetic resonance imaging of multiple sclerosis at 7 Tesla with sensitivity to iron. Ann Neurol 2008;64(6):707-713.

149. Bilgic B, Pfefferbaum A, Rohlfing T, Sullivan EV, Adalsteinsson E. MRI estimates of brain iron concentration in normal aging using quantitative susceptibility mapping. Neuroimage 2012;59(3):2625-2635.
150. Haacke EM, Makki M, Ge Y, Maheshwari M, Sehgal V, Hu J, Selvan M, Wu Z, Latif Z, Xuan Y, Khan O, Garbern J, Grossman RI. Characterizing iron deposition in multiple sclerosis lesions using susceptibility weighted imaging. J Magn Reson Imaging 2009;29(3):537-544.
151. Yao B, Bagnato F, Matsuura E, Merkle H, van Gelderen P, Cantor FK, Duyn JH. Chronic multiple sclerosis lesions: characterization with high-field-strength MR imaging. Radiology 2012;262(1):206-215.
152. Barkhof F, Simon JH, Fazekas F, Rovaris M, Kappos L, de Stefano N, Polman CH, Petkau J, Radue EW, Sormani MP, Li DK, O'Connor P, Montalban X, Miller DH, Filippi M. MRI monitoring of immunomodulation in relapse-onset multiple sclerosis trials. Nat Rev Neurol 2011;8(1):13-21.
153. McDonald WI, Compston A, Edan G, Goodkin D, Hartung HP, Lublin FD, McFarland HF, Paty DW, Polman CH, Reingold SC, Sandberg-Wollheim M, Sibley W, Thompson A, van den Noort S, Weinshenker BY, Wolinsky JS. Recommended diagnostic criteria for multiple sclerosis: guidelines from the International Panel on the diagnosis of multiple sclerosis. Annals of Neurology 2001;50(1):121-127.
154. Lee J, Shmueli K, Fukunaga M, van Gelderen P, Merkle H, Silva AC, Duyn JH. Sensitivity of MRI resonance frequency to the orientation of brain tissue microstructure. Proceedings of the National Academy of Sciences of the United States of America 2010;107(11):5130-5135.